

SAR Imagery for Detecting Sea Surface Slicks: Performance Assessment of Polarization-Dependent Parameters

Sébastien Angelliaume¹, Pascale C. Dubois-Fernandez, *Senior Member, IEEE*, Cathleen E. Jones, Benjamin Holt, Brent Minchew, Emna Amri, and Véronique Miegebielle

Abstract—Remote sensing technology is an essential link in the global monitoring of the ocean surface, and radars are efficient sensors for detecting marine pollution. When used operationally by authorities, a tradeoff must usually be made between the covered area and the quantity of information collected by the radar. To identify the most appropriate imaging mode, a methodology based on receiver operating characteristic curve analysis has been applied to an original data set collected by two airborne systems operating at L-band, both characterized by a very low instrument noise floor. The data set was acquired during controlled releases of mineral and vegetable oil at sea. Various polarization-dependent quantities are investigated, and their ability to detect slick-covered areas is assessed. A relative ordering of the main polarimetric parameters is reported in this paper. When the sensor has a sufficiently low noise floor, HV is recommended because it provides the strongest slick-sea contrast. Otherwise, VV is found to be the most relevant parameter for detecting slicks on the ocean surface. Among all the investigated quad-polarimetric settings, no significant added value compared to single-polarized data was found. More specifically, it is demonstrated, by increasing the instrument noise level, that the studied polarimetric quantities which combine the four polarimetric channels have performances of detection mainly driven by the instrument noise floor, namely, the noise equivalent sigma zero. This result, obtained by progressively adding noise to the raw synthetic aperture radar (SAR) data, indicates that the polarimetric discrimination between clean sea and polluted area results mainly from the differentiated behavior between single-bounce scattering and noise. It is thus demonstrated, using SAR data collected with a low instrument noise floor, that there is no deviation from Bragg scattering for radar scattering from ocean surface covered by mineral and vegetable oil.

Index Terms—Bragg, detection, instrument noise, marine pollution, noise, noise equivalent sigma zero (NESZ), noise floor, ocean, oil, polarimetric discrimination, polarization, probability of detection (Pd), probability of false alarm (Pfa), radar, ranking,

Manuscript received October 11, 2017; revised December 20, 2017 and January 26, 2018; accepted January 28, 2018. This work was supported in part by the French National Research Agency (ANR) through the POLLUPROOF Research Program under Grant ANR-13-ECOT-007 and in part by the New Advanced Observation Method Integration Project, a common research program between Total (the French Petroleum Company) and ONERA (the French Aerospace Lab). (*Corresponding author: Sébastien Angelliaume.*)

S. Angelliaume, P. C. Dubois-Fernandez, and E. Amri are with ONERA, DEMR, 13661 Salon de Provence, France (e-mail: sebastien.angelliaume@onera.fr).

C. E. Jones and B. Holt are with the Jet Propulsion Laboratory, California Institute of Technology, Pasadena, CA 91109 USA.

B. Minchew is with British Antarctic Survey, Cambridge CB3 0ET, U.K.

V. Miegebielle is with the Remote Sensing Department, Total, 64018 Pau, France.

Color versions of one or more of the figures in this paper are available online at <http://ieeexplore.ieee.org>.

Digital Object Identifier 10.1109/TGRS.2018.2803216

receiver operating characteristic (ROC) curves, synthetic aperture radar (SAR), sea, slick, spill.

I. INTRODUCTION

SPACEBORNE and airborne remote sensing sensors are commonly used in the offshore domain for monitoring natural and anthropogenic oil slicks [1]–[3]. These sensors allow the authorities and the petroleum companies to monitor sea shipping lanes to identify possible fuel releases, respond to incidents occurring at surface or subsurface oil and gas facilities, and identify the occurrence of natural hydrocarbons (seeps) on the sea surface [4]–[6], testifying to the presence of mature source rock on the ocean bottom.

Because of the constraints linked mainly to weather conditions and the risk of significant cloud cover, the use and programming of synthetic aperture radar (SAR) data is usually favored over optical imagery for oil slick detection over the ocean surface [6]–[8]. SAR is a powerful tool for detecting hydrocarbons or chemicals on the sea surface because of the sensitivity of the electromagnetic (EM) scattering to surface roughness. In calm seas, most of the transmitted energy is reflected away from the radar and the backscattered signal toward the instrument is very low. Wind-driven roughness increases the total backscattered energy from the surface. Oil films on the sea surface damp the capillary and short gravity waves [9], [10], which are the main source of sea surface roughness. As a consequence, slicks appear as dark areas in the SAR image (low backscattered signal), which makes the presence of an oil slick on the sea surface detectable in radar imagery.

Several major issues are identified in the success of hydrocarbon detection in the offshore domain, the first of which remains today, namely, the revisit time. Indeed, in an emergency situation, obtaining quick information from spaceborne sensors is decisive. The latency is constrained by the repeat orbit interval of SAR satellite systems, the trajectory of the orbits, the location of the area of interest (e.g., there are more possibilities of acquisition daily at high latitudes than that toward the equator), the data recording and downlink system, and the SAR viewing geometry agility [11]. Thus, very large swath modes are often selected by maritime surveillance services to the detriment of the spatial resolution or to the amount of information potentially collected over the area of interest, for example, with polarimetric modes. Monitoring

services exploit mainly radar remote sensing data acquired in a single-polarization mode, maximizing the covered surface of the ocean. Due to a higher backscattered signal level from the sea surface for vertically (V) polarized waves than that for horizontal (H) polarization [12], the VV channel is often preferred to HH for ocean studies. Because most of the spaceborne SAR systems available today have a moderate noise floor (between -20 and -35 dBm²/m² [13]), the cross-polarization (HV or VH) channels have not been used for operational ocean slick detection.

The second major issue affecting the success of offshore hydrocarbon detection concerns the speed of data analysis coupled with the reliability of hydrocarbon detection. Operationally, the analysis of SAR images is mostly based on the visual identification of dark areas corresponding to oil slicks [14]. Many oceanic and atmospheric phenomena can occur over the sea surface and manifest themselves on radar images in the same way as areas covered by hydrocarbons. These are called look-alikes, and they can originate from several sources [15]: 1) natural biogenic surface films produced by fish or plankton; 2) young and thin sea ice; 3) low-wind areas; and 4) upwelling of cold water. For decades, Alpers *et al.* [15], Migliaccio *et al.* [16], and Hansen *et al.* [17] have attempted to develop methodologies to differentiate ocean areas covered by hydrocarbon from look-alikes. Today, the discrimination between biogenic films and mineral oil slicks remains an active area of research [15]. The method of conventional operational SAR analysis is mainly based on the experience and expertise of the image interpreter. In order to facilitate visual inspection, there have been many studies of the SAR signature of hydrocarbons observed in different acquisition configurations in order to identify the optimal detection method. Regarding the choice of sensor, the reliability of detection depends mainly on the frequency band and the sensor noise floor. For example, it has been demonstrated in [18] that SAR images acquired at high frequency (e.g., X- or C-band) are preferable to those acquired at lower frequency (e.g., L-band) for mineral oil slick detection. In parallel with system considerations, it is essential to know what information is most relevant for detection, especially information that can be obtained from the polarization of the EM waves. Because many studies published in the literature have suggested that multipolarization (dual-polarization or quad-polarization) or polarimetric (POLoSAR, i.e., using both amplitude and phase information) parameters improve the detection capability of slicks compared to single-polarization data [19]–[26], exploring various polarization-dependent SAR parameters accessible in the range of possible SAR acquisition configurations is a valuable aid to operational teams in ranking the acquisition modes that can be used.

The aim of this paper is to present a prioritization of SAR parameters to enhance and facilitate slick detection in the offshore domain. The originality of the proposed method lies in the definition and quantitative evaluation of parameters calculated using data obtained in quad-polarimetric mode by two airborne SARs operating at L-band (1.275 and 1.325 GHz) with very high signal-to-noise ratio (SNR) over controlled releases of mineral and vegetable oil at sea. These two sensors are Système Expérimental de Télédétection Hyperfréquence

Imageur (SETHI) operated by ONERA [27], the French Aerospace Lab, and Uninhabited Aerial Vehicle Synthetic Aperture Radar (UAVSAR) operated by National Aeronautics and Space Administration (NASA)/Jet Propulsion Laboratory (JPL) [28].

This paper is organized as follows. Section II presents the basis of the radar scattering from the ocean surface. Section III summarizes the state-of-the-art POLoSAR parameters proposed in the literature for slick detection. Section IV describes the airborne SAR data used in this paper. Section V presents the methodology used to evaluate the studied parameters and gives the results, and main discussions are presented in Section VI.

II. RADAR SCATTERING FROM THE OCEAN SURFACE

Over a rough sea surface where Bragg scattering is dominant (incidence angles in the so-called “plateau region” [29], ranging from around 30° to 60°), the co-polarized channels (HH and VV) have higher backscattered power than that of the cross-polarized (HV and VH) channels. Higher backscattered power means higher SNR, which makes these channels more attractive for slick detection on the sea surface where typical backscattered power can be low [17]. The co-polarized radar backscattered power is proportional to the normalized radar cross section (NRCS), which is defined in the Bragg scattering theory [12] as

$$\sigma_{pp}^0 = 4\pi k_{EM}^4 \cos^4 \theta_i \Gamma_{pp} W(k_B) \quad (1)$$

$$k_B = 2k_{EM} \sin \theta_i \quad (2)$$

where subscript p denotes either H (horizontal) or V (vertical) polarization; $k_{EM} = 2\pi/\lambda_{EM}$ is the EM wavenumber corresponding to the radar wavelength λ_{EM} ; Γ_{pp} is the reflectivity; $W(k_B)$ is the spectral density of ocean surface roughness evaluated at the Bragg wavenumber k_B ; and θ_i is the radar local incidence angle. The spectral density of the sea surface describes the components of the ocean wave spectrum that contribute to the scattering of the radar pulses [30], while the reflectivity describes the total power scattered from the surface.

This formulation of the NRCS (1) does not fully explain the EM signal backscattered by a rough sea surface because it takes into account only the polarized components of the backscattering from the ocean surface. Deviations between model estimation (Bragg theory) and real observation [31], [32] are often explained through nonresonant mechanisms, called non-Bragg or nonpolarized effects [33]. Those mechanisms are generally associated with breaking waves or whitecaps, and they contribute to the total backscattered energy from the sea surface. However, the contribution of non-Bragg scattering to the total NRCS is frequency dependent, and it has been reported in [34] that at low EM frequency (e.g., L-band), the relative contribution of this non-polarized component with respect to the total power scattered from the ocean surface is negligible. For this reason, we do not consider nonpolarized effects in the rest of this paper.

The local incidence angle of the EM wave θ_i is defined [12] as

$$\theta_i = \cos^{-1}[\cos(\theta + \psi) \cos \xi] \quad (3)$$

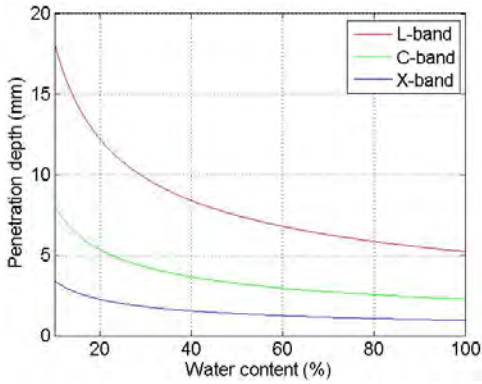


Fig. 1. Penetration depth as a function of water content (volumetric percentage) based on a linear mixing model for the dielectric constant at L-band (red), C-band (green), and X-band (blue); dielectric constants are specified in Table I.

where θ is the EM angle of incidence relative to the local, untilted surface vertical direction and ψ and ζ are defined in the following paragraph.

The sea surface is modeled as a set of slightly rough tilted facets that contributes to the backscattering of the incident radiation. Each facet has superimposed small-scale surface roughness that creates a Bragg scatterer when the roughness scale is commensurate with the radar wavelength. Small-scale roughness is randomly distributed on the scattering surface and responds to the strength of local wind, which generates capillary and short gravity waves whose wavelengths are of the order centimeters to decimeters with periods less than 1 s [35]. The tilt of the facet is caused by larger scale gravity waves on the ocean surface that change the local orientation, or tilt, of the short waves [36]. The orientation of the facet of the sea surface is defined by two angles: ψ , which is the angle between local up and the projection of the facet normal onto the radar scattering plane (in-plane tilt), and ζ , which is the angle between local up and the projection of the facet normal onto the vertically oriented plane perpendicular to the scattering plane (out-of-plane tilt) (see [37, Fig. 1]).

The co-polarized reflectivity Γ_{pp} is a function of the local geometry and the electrical properties of the scattering surface (e.g., seawater and films) such that

$$\Gamma_{pp} = \left| \left(\frac{\sin(\theta + \psi) \cos \zeta}{\sin \theta_i} \right)^2 \alpha_{pp} + \left(\frac{\sin \zeta}{\sin \theta_i} \right)^2 \alpha_{qq} \right|^2 \quad (4)$$

where subscript $q(p \neq q)$ denotes either H or V polarization. The co-polarized Bragg scattering coefficients, introduced in (4), are defined [12] as

$$\alpha_{HH} = \frac{\cos \theta_i - \sqrt{\varepsilon_r - \sin^2 \theta_i}}{\cos \theta_i + \sqrt{\varepsilon_r - \sin^2 \theta_i}} \quad (5)$$

$$\alpha_{VV} = \frac{(\varepsilon_r - 1)(\sin^2 \theta_i - \varepsilon_r(1 + \sin^2 \theta_i))}{(\varepsilon_r \cos \theta_i + \sqrt{\varepsilon_r - \sin^2 \theta_i})^2} \quad (6)$$

They depend only on the local incidence angle of the EM wave θ_i and the complex-valued relative dielectric constant of the imaged surface ε_r .

TABLE I
DIELECTRIC CONSTANT OF SEAWATER FROM [38] AND
MINERAL OIL FROM [39] AND [40]

Material	L-BAND [1.3 GHz]	C-BAND [5.0 GHz]	X-BAND [10 GHz]
Seawater (15°C 35 PSU)	73.0+65.1i	66.8+35.7i	52.9+39.0i
Mineral oil	2.3+0.01i	2.3+0.01i	2.3+0.01i

The relative dielectric constant ε_r defined as the ratio between the material dielectric constant and the electric constant in a vacuum is a complex number. Its value is material dependent and varies with the radar frequency. The imaginary part characterizes how far an EM wave can penetrate into a conducting medium. The penetration depth δ_p is defined as the depth where the power of the propagating EM wave is attenuated by a factor of $1/e$ such that

$$\delta_p = \frac{1}{2k_{EM} \text{Im}(\sqrt{\varepsilon_r})} \quad (7)$$

where $\text{Im}(\cdot)$ selects the imaginary part of a complex number. Typical values of dielectric constant of seawater [38] and mineral oil [39], [40] are given in Table I. Note that the value of the dielectric constant for mineral oil is nearly constant in the range 1–10 GHz, with a loss factor (imaginary component) close to 0, suggesting a nonnegligible penetration of the EM wave through this medium.

Assuming a linear mixing model, the effective dielectric constant of a water-in-oil emulsion (ε_{em}) is given by

$$\varepsilon_{em} = v\varepsilon_w + (1 - v)\varepsilon_{oil} \quad (8)$$

where v , ranging from 0 to 1, is the water content by volume of the oil–water mixture, and ε_w and ε_{oil} are the relative dielectric constants of seawater and oil, respectively. It follows from (8) that the effective dielectric constant of a mixture of oil and seawater is lower than that of seawater alone [41]. From values given in Table I and from (7) and (8), it is seen that the penetration depth decreases with increasing frequency and water content, with typical penetration depth of the order of millimeters for water content greater than 50% (Fig. 1).

When hydrocarbons are spilled into a marine environment, the oil can be mixed with seawater within the upper few centimeters of the water column or can behave like a viscoelastic film floating on the surface. In the first case, mixing of oil with seawater will lead to a reduction of the relative dielectric constant of the contaminated sea surface compared to the surrounding slick-free area. This will contribute to a decrease in the total radar backscattered power, along with suppression of the Bragg-wavelength gravity–capillary waves that are present due to the difference in surface tension and density. In the second case (thin film), radar-backscattered power is mainly diminished through mechanical damping of Bragg-wavelength gravity–capillary waves. The capability of radar imagery to distinguish between varying substances that manifest as a thin film on the sea surface or that mix with seawater near the surface has already been demonstrated in the case of

mineral oil [42] and chemicals [43]. If the thickness of the film on the top of the sea surface is thin compared to the penetration depth δ_p , the EM wave is not altered and will penetrate the film to scatter from the seawater below the film, so the effective dielectric constant will remain that of seawater, and not be changed by different, generally lower, dielectric constants of that product which forms the film. When the film becomes thicker (relative to the penetration depth), the dielectric properties of the film/seawater mixture will be reduced compared to seawater itself, with the mixture acting as a separate layer on the ocean surface with intermediate dielectric values that will also impact the power of the backscattered signal.

Mineral oil films can form multilayers, whose thickness can vary considerably within oil patches, from less than 1 μm to more than 1 mm [44]–[46]. When released at sea, mineral oil mixes quickly with seawater under the action of wind and waves and will result in water-in-oil mixture (emulsion) with water content generally between 50% and 75% [47].

Results shown in Fig. 1 suggest that the backscattered signal from ocean surface covered by a mineral oil film will only be impacted by the dielectric properties of the medium in the case of very thick slick, with greater effect on high-frequency imaging radar. Otherwise, damping of the sea surface roughness will be the primary mechanisms for decreasing radar-backscattered power. Because the dielectric constants of biogenic films and mineral oil are similar [48], [49] and because biogenic films can be observed on the ocean surface only in the form of monolayers [15], [18], i.e., they are only one molecular layer thick (typical thickness of 2.4–2.7 nm), the same phenomena will be observed as in the case of mineral oil film, namely, reduced backscattered power caused by mechanical damping of the Bragg-wavelength surface waves with little dependence on the effective dielectric constant.

III. STATE-OF-THE-ART POLSAR PARAMETERS

Radar remote sensing techniques are of great interest for monitoring slick-covered ocean surface for two primary reasons. First, EM waves are sensitive to the modification of the sea surface induced by oil. Second, SAR sensors can be used any time of day or year and in almost any weather conditions [50]. The physical interaction between an EM wave and a slick-covered area has been established by analyzing airborne and spaceborne data acquired over ocean surfaces covered by mineral oil and biogenic film [18], [51], [52]. Many studies [19]–[26] have analyzed the added value of polarimetric SAR data for slick monitoring. A review of SAR parameters used for this purpose is given in [14], where most of the methods published in the literature for oil slick detection are presented. Since this publication in 2012, many researchers have attempted to assess the utility of POLSAR parameters for slick detection. These works exploit either accidental events [53] or controlled releases of pollutant at sea, the latter of which includes experiments managed by the Norwegian Clean Seas Association for Operating Companies (NOFO) in the North Sea [17], [25], [26], [54]–[57] or the POLLUPROOF experiment whose objective is to establish a procedure for collecting evidence of

illegal maritime pollution by chemicals using remote sensing sensors [43]. In the following, we focus on polarization-dependent parameters that have been found to be efficient for slick detection in the offshore domain [13], [14] and we organize them by input data type. These are separated into categories that use backscattered amplitudes only (incoherent systems) and those that use both amplitude and phase of the backscattered signals (coherent systems, i.e., POLSAR modes of operation), and into systems that acquire dual-polarization data (HH/HV, VV/VH, or HH/VV acquisitions) and those that acquire quad-polarization data (HH/VV/HV/VH). Here we consider only linearly polarized systems, which are currently the most common in remote sensing.

A. Dual-Polarized Synthetic Aperture Radar

1) *Incoherent Dual-Co-Polarized Radar Imaging System:* For slick-detection methods using a dual-co-polarized (HH and VV) radar remote sensing system, the two relevant parameters that use amplitude data only [33] are the Polarization Ratio (PR) and the Polarization Difference (PD), respectively, defined within the Bragg model (in linear units) as

$$\text{PR} = \frac{\sigma_{\text{HH}}^0}{\sigma_{\text{VV}}^0} \approx \frac{\alpha_{\text{HH}}}{\alpha_{\text{VV}}} \quad 0 \leq \text{PR} \leq 1 \quad (9)$$

$$\text{PD} = \sigma_{\text{VV}}^0 - \sigma_{\text{HH}}^0 \quad \text{PD} \geq 0. \quad (10)$$

As backscattered power over the sea surface in the Bragg regime is stronger in VV polarization than that in HH [12], it follows that PR varies between 0 and 1 and PD takes positive values. As reflectivities at VV and HH are always different when the SNR is greater than 0 dB, there is no realistic scenario in which backscattered power is nonzero and PD is equal to 0. It follows from (9) that PR, commonly referred to as the Bragg ratio when written in this simplified form, is independent of sea surface roughness (W) and depends only on the local incidence angle and the relative dielectric constant [41], [42]. Because the relative dielectric constant is lower for slick-covered areas than for uncontaminated seawater [41], the Polarization Ratio (PR) can detect sea surface slicks through the decrease in the relative dielectric constant. It is also considered an effective parameter to distinguish between slick-covered sea surface and oceanographic phenomena [17].

When the ocean surface is covered by a thin film (like biogenic or thin mineral oil film), the surface layer is transparent to the EM waves, and thus the radar will sense the dielectric constant of the seawater under the film, which will have no effect on the Polarization Ratio [58]. However, for thick oil film (relative to the radar wavelength) or emulsions, the dielectric constant of the imaged product will affect the radar backscattering and its effect will manifest itself on the Polarization Ratio. Thus, Polarization Ratio could be used to discriminate between thin film and emulsion/thick film. However, at least one major issue occurs when using the Polarization Ratio for slick characterization at sea. The contrast, which is defined as the ratio of the values obtained over contaminated and uncontaminated areas, is low. This limitation is evident in Fig. 2 where, for example, there is little difference

in PR between pure seawater (line labeled 100%) and a 50–50 or a 25–75 mixture of seawater and oil.

The PD parameter is of interest for slick detection at sea [17], [33], [43] because it is proportional to the spectral density of the ocean surface roughness [59], which is altered even by thin films [9], [10]. As discussed in [33], the non-polarized part of the backscattered signal (see Section II) is removed using PD. Therefore, the Polarization Difference mostly contains contributions due to the presence of short wind-driven waves around the Bragg wavenumber (2), making PD an attractive parameter for slick detection at sea [33], [43].

2) Coherent Dual-Co-Polarized Radar Imaging System:

The Polarization Difference (PD) and the Polarization Ratio (PR), introduced above, use only the backscattered power of the complex dual-polarized signals. With a remote sensing system collecting coherent acquisitions, the phase between the two co-polarized channels is measured. In this case, the following parameters are generally recommended in the literature for slick detection over the ocean surface: the modulus of the co-polarized complex coherence (ρ_{HHVV}) [22], [25] and the Bragg likelihood ratio (BLR) [25], [26]

$$\rho = \frac{\langle S_{HH} S_{VV}^* \rangle}{\sqrt{\langle |S_{HH}|^2 \rangle \cdot \langle |S_{VV}|^2 \rangle}} = \rho_{HHVV} e^{j\Delta\phi} \quad 0 \leq \rho_{HHVV} \leq 1 \quad (11)$$

$$\text{BLR} = \max\{0, \text{Re}(\rho)\} \quad 0 \leq \text{BLR} \leq 1. \quad (12)$$

In (11) and (12), superscript * denotes the complex conjugate, $\langle \cdot \rangle$ denotes spatial averaging, $\text{Re}(\cdot)$ denotes the real part of a complex number, and S_{pp} represents the complex scattering coefficient. In the case of an EM signal backscattered by rough surface, the co-polarized channels (HH and VV) are correlated and in phase [12], [60]. It follows that the complex correlation of the co-polarized channels is a real number (imaginary part close to 0) and the modulus (ρ_{HHVV}) takes values close to 1. Thus, these two parameters have the same behavior, namely, the value is high (close to 1) when the Bragg scattering mechanism is dominant and the value is low (close to 0) otherwise. However, when the backscattered signal is corrupted by noise, the phase between the co-polar channels becomes uniformly distributed between 0 and π and the modulus of the co-polarized coherence reaches 0. The polarimetric coherence between the co-polarized channels can be written as the product of three terms

$$\rho_{HHVV} = \rho_{\text{Scattering}} \rho_{\text{Temp}} \rho_{\text{SNR}} \quad (13)$$

where $\rho_{\text{Scattering}}$ denotes the correlation between HH and VV due to scattering mechanism (close to 1 over ocean surface) and ρ_{Temp} and ρ_{SNR} denote temporal decorrelation and decorrelation due to noise, respectively. The decorrelation time of a moving sea surface is of the order of 1×10^{-2} s at X-band [61] and 1×10^{-1} s at L-band [62]. For sensors operating at low pulse repetition interval (PRI), the decorrelation due to time lag between transmitted pulses (alternatively polarized H and V) can be neglected. For the two sensors investigated in Sections IV-A and IV-B, the PRIs are equal to 1×10^{-7} s for SETHI and 2.3×10^{-6} s for UAVSAR, which

are both orders of magnitude smaller than the surface decorrelation time and assure no temporal decorrelation between HH and VV (ρ_{Temp} close to 1). Thus, the only remaining decorrelation term is that induced by the noise defined as

$$\rho_{\text{SNR}} = \frac{1}{1 + \text{SNR}^{-1}}. \quad (14)$$

Equation (14) exhibits the strong dependence of the modulus of the co-polarized complex coherence (ρ_{HHVV}), as well as the BLR, on the SNR. Following (14), an SNR equal to 10 or 5 dB induces a decorrelation between the two co-polarized channels of 10% and 25%, respectively.

In addition to their strong dependence on the SNR, being normalized by the amplitude of the co-polarized backscattering coefficient, both ρ_{HHVV} and BLR are more strongly affected by the noise (low SNR) than the intensities alone. To overcome this limitation while exploiting the potential of these parameters, we propose in this paper to use the Hermitian product (HP) between the two co-polarized channels, defined as

$$\text{HP} = \langle S_{HH} S_{VV}^* \rangle. \quad (15)$$

3) Coherent Dual-Polarized Radar Imaging System: A way to represent polarimetric information collected by a coherent dual-polarized (HH and HV or VV and VH) remote sensing system is the Stokes formalism [63]–[65]. The Stokes parameters are a set of four values (S_0 , S_1 , S_2 , and S_3) describing the polarization state of an EM wave

$$S_0 = \langle |E_H|^2 + |E_V|^2 \rangle \quad (16)$$

$$S_1 = \langle |E_H|^2 - |E_V|^2 \rangle \quad (17)$$

$$S_2 = 2\text{Re}(\langle E_H E_V^* \rangle) \quad (18)$$

$$S_3 = 2\text{Im}(\langle E_H E_V^* \rangle) \quad (19)$$

where $\text{Re}(\cdot)$ and $\text{Im}(\cdot)$ select the real and the imaginary values, respectively, of a complex number. E is the measured complex scattering coefficient in the subscripted polarization and is independent of the polarization state of the transmitted wave. Using this formalism, Touzi *et al.* [19], Shirvany *et al.* [23], and Nunziata *et al.* [24] have proposed to use the degree of polarization (DoP) for ship or marine pollution detection

$$\text{DoP} = \frac{\sqrt{S_1^2 + S_2^2 + S_3^2}}{S_0} \quad 0 \leq \text{DoP} \leq 1. \quad (20)$$

Over ocean surface, the EM wave is well polarized [60] and the DoP is close to 1 [23]. When the received signal is dominated by the noise, as in the case for slicked surfaces imaged by most of spaceborne SARs available today, the measured signals appear depolarized and the DoP reaches values close to 0.

These last four parameters (ρ_{HHVV} , BLR, HP, and DoP), derived from co-polarized coherent acquisitions, are recommended in the literature for oil slick detection and the proposed justification comes from their ability to distinguish Bragg scattering (over clean sea surface) to another scattering mechanism that may occur over slick-covered area [19], [22]–[25]. However, the impact of the noise on these parameters is often omitted even though, as we have just seen, it can have a predominant effect. An analysis of the impact of the noise is presented in Section V-D.

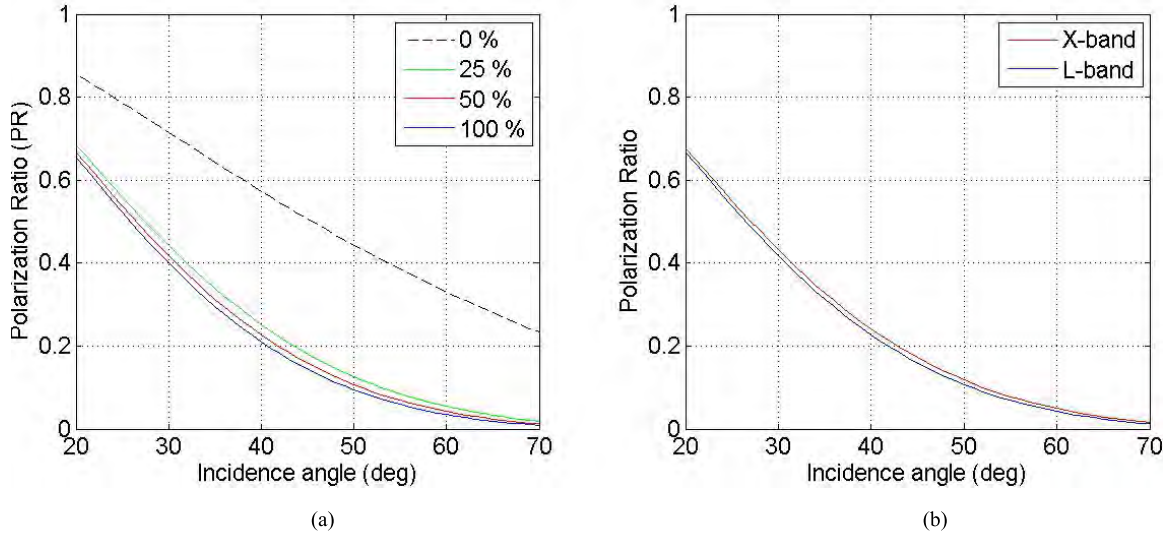


Fig. 2. PR (Bragg theory) as a function of incidence angle (a) at L-band for a water content of 0% (black dashed line), 25% (green line), 50% (red line), and 100% (blue line) and (b) at X-band (red line) and L-band (blue line) for a water content of 50%. A linear mixing is assumed between mineral oil and seawater. Values of dielectric constants are from Table I.

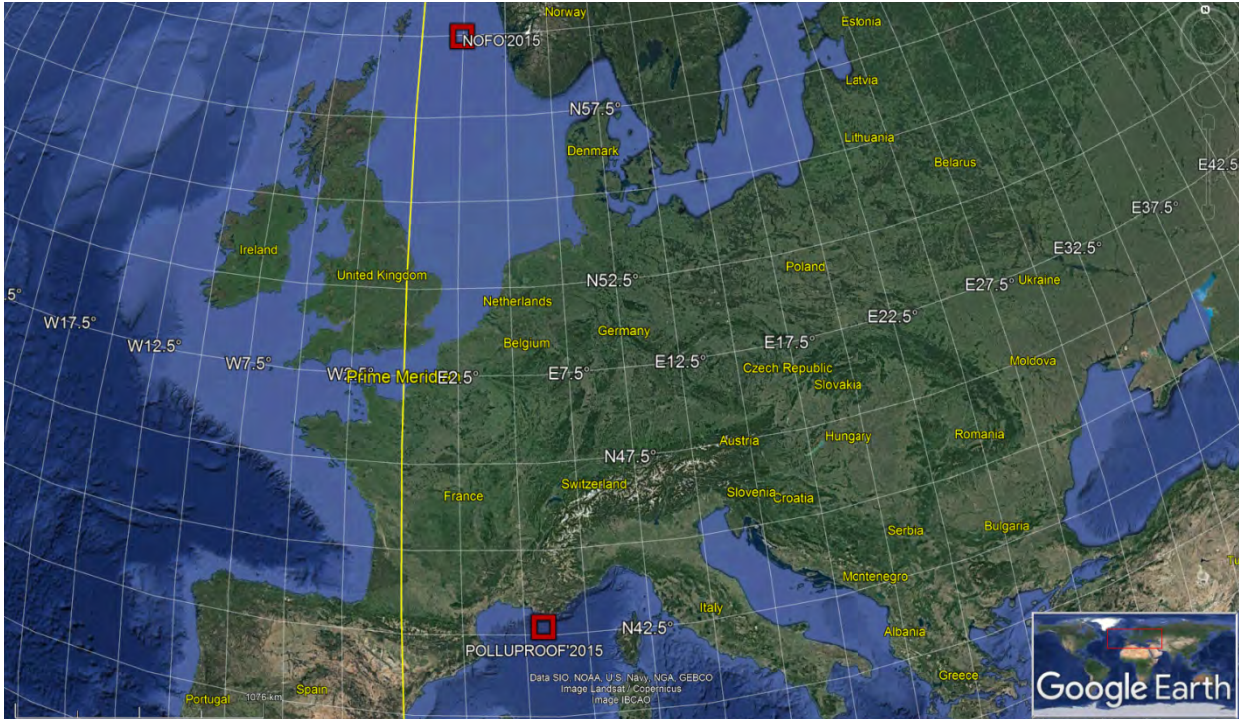


Fig. 3. Map of the POLLUPROOF*2015 and NOFO*2015 experimental sites.

B. Coherent Quad-Polarized Synthetic Aperture Radar

Many methods using quad-polarized remote sensing data are proposed in the literature to detect ocean surface covered by a slick. For a review, the reader is referred to [13] and [14]. Here we consider a few parameters dependent on all polarizations, namely, the Conformity Coefficient (μ) [66], originally proposed in [67] for remote sensing application over land surfaces, the first eigenvalue (λ_1) [41], and the Entropy (H) [25], [66] based on the eigenvalue decomposition of the covariance matrix C [68], [69]

$$\mu \approx \frac{2(\text{Re}(S_{HH}S_{VV}^*) - |S_{HV}|^2)}{|S_{HH}|^2 + 2|S_{HV}|^2 + |S_{VV}|^2} \quad -1 \leq \mu \leq 1 \quad (21)$$

$$C = \begin{bmatrix} \langle |S_{HH}|^2 \rangle & \sqrt{2} \langle S_{HH}S_{HV}^* \rangle & \langle S_{HH}S_{VV}^* \rangle \\ \sqrt{2} \langle S_{HV}S_{HH}^* \rangle & 2 \langle |S_{HV}|^2 \rangle & \sqrt{2} \langle S_{HV}S_{VV}^* \rangle \\ \langle S_{VV}S_{HH}^* \rangle & \sqrt{2} \langle S_{VV}S_{HV}^* \rangle & \langle |S_{VV}|^2 \rangle \end{bmatrix}. \quad (22)$$

Over the ocean, because the cross-polarized signal is very low, the Conformity Coefficient can be interpreted in the same way as the co-polarized coherence (11) or the BLR (12). A simple algorithm with a threshold equal to 0 is proposed in [66] for oil slick detection. The Entropy has similar interpretation to that of the Degree of Polarization (DoP), but with values near 0 corresponding to one dominant scattering mechanism and values close to 1 when multiscattering occurs or when the signal is corrupted by noise [68], [69].

TABLE II
ENVIRONMENTAL CONDITIONS AND PROPERTIES OF RELEASED SUBSTANCES

Date of release	Time of release (UTC)	Amount of release	Released substance	Time of imaging (UTC)	Wind speed (m/s)	Wind direction (from-deg)	Wave height (m) at time of imaging
22 May, 2015	15:00-15:30	1 m ³	Rapeseed oil	16:07	7	315	2
22 May, 2015	15:25-15:40	1 m ³	FAME	16:07	7	315	2
09 June, 2015	06:30-08:00	45 m ³	Mineral oil	09:56 10:01	5	255	1

TABLE III
PROPERTIES OF SAR SCENES INVESTIGATED IN THIS PAPER. INCIDENCE ANGLE AND NESZ VALUES ARE THE MINIMUM AND MAXIMUM ACROSS THE IMAGING SWATH

Sensor	Frequency band	Polarization mode	Experiment	Date	Time (UTC)	Incidence angle (deg)	NESZ (dBm ² /m ²)
SETHI	L	Quad-Pol	POLLUPROOF	22 May, 2015	16:07	34 / 52	-51 / -53
SETHI	L	Quad-Pol	NOFO	09 June, 2015	10:01	34 / 52	-51 / -53
UAVSAR	L	Quad-Pol	NOFO	09 June, 2015	09:56	19 / 68	-35 / -51

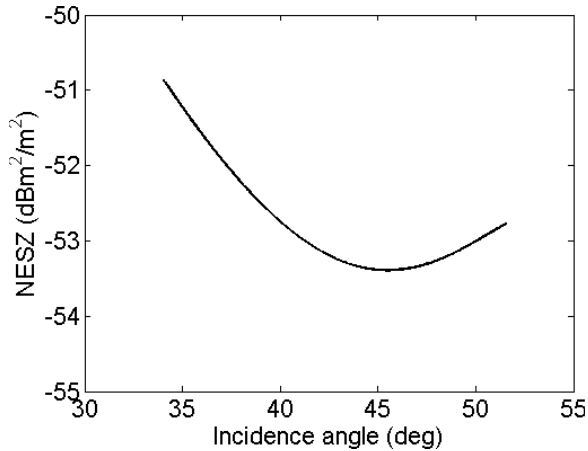


Fig. 4. SETHI—POLLUPROOF’2015 and NOFO’2015 experiments—instrument noise floor (NESZ) plotted by increasing incidence angle.

The main issue when working with quad-polarized SAR data is the low power of the backscattered signal in the cross-polarization channels (HV and VH). For most of spaceborne SAR sensors available today, the backscattered signal measured in cross-polarization over slick-covered area is close to or below the instrument noise floor [17]. This low SNR values strongly impact the values of the polarimetric parameters measured over oil slicks.

IV. EXPERIMENTAL DATA

Two experimental campaigns of measurements are used in this paper: NOFO’2015 and POLLUPROOF’2015 (see Fig. 3). POLLUPROOF’2015 was conducted in May 2015 over the

Mediterranean Sea (off the French coast, near 42°45’ N, 5°45’ E) and focused on the release and subsequent observation of several hazardous and noxious substances (HNS) that are meant to represent the majority of chemicals commonly transported by sea. The primary goal of this experiment is to establish a procedure for collecting evidence of illegal marine pollution by HNS using airborne sensors [43]. SAR images of controlled releases of fatty acid methyl esters (FAME) and rapeseed oil, conducted during the POLLUPROOF’2015 experiment, are investigated in this paper (Table II). Vegetable oils (like plant oil or rapeseed oil) have already been imaged by SAR sensors as they are often used to simulate a natural monomolecular biogenic slick [15], [18], [25]. NOFO’2015 was conducted from June 8, 2015 to June 14, 2015, during NOFO’s oil-on-water exercise. This experiment aims at testing recovering systems of pollution at sea by hydrocarbons. During the exercise, airborne and spaceborne acquisitions were collected over the offshore spill areas (North Sea, near 59°59’ N, 2°27’ E—see Fig. 3 and [56, Fig. 2]). In the following, we use SAR images collected by the French and American airborne sensors on June 9, 2015. For the investigated experiment, the released product is an emulsion of mineral oil in water, with a water content of 60% (Table II). It consists of a mixture of seawater, Oseberg crude oil, and a small addition of intermediate fuel oil (IFO) 380 (IFO or marine diesel oil, with a viscosity of 380 mm²·s⁻¹). For the trial, 45 m³ of mineral oil emulsion was discharged at sea. Large swath remote sensing data collected by UAVSAR (see Section IV-B) imaged the full extent of the hydrocarbon-covered area, namely, 5.4 km². Assuming all the 45 m³ of mineral oil emulsion released at sea was on

TABLE IV
SIGNAL-TO-NOISE RATIO—SETHI, NOFO'2015 EXPERIMENT, JUNE 09, 2015, 10:01 UTC

Region	Incidence angle (deg)	HH	HV	VV
		MEAN [MIN MAX] dB	MEAN [MIN MAX] dB	MEAN [MIN MAX] dB
Clean sea	44.5°	26.5 [25.8 27.4] dB	16.4 [15.6 17.2] dB	34.1 [33.3 34.9] dB
Oil slick	44.5°	21.5 [19.7 23.0] dB	10.2 [8.6 12.3] dB	28.0 [26.3 29.3] dB

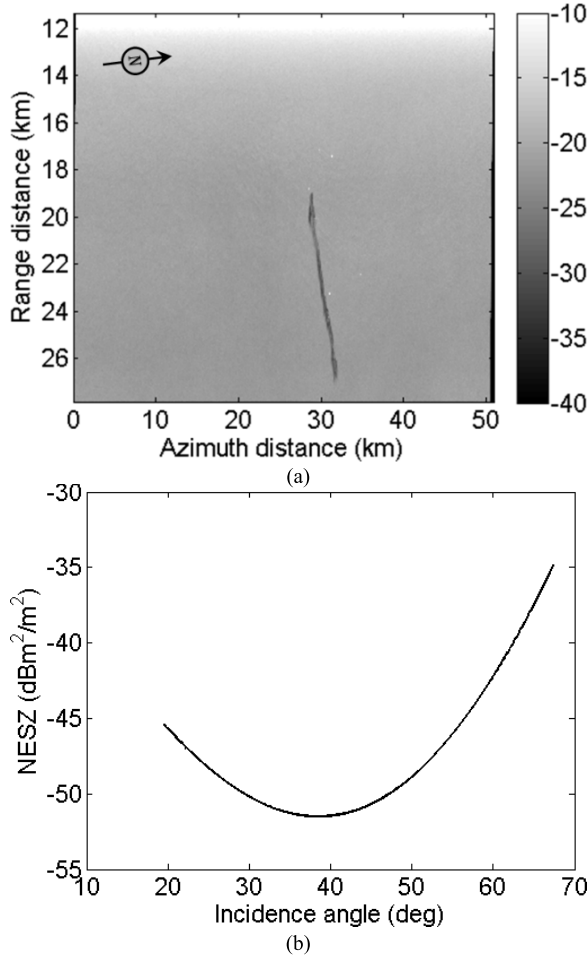


Fig. 5. UAVSAR—NOFO'2015 experiment, June 09, 2015, 09:56 UTC. (a) VV image and (b) instrument noise floor (NESZ) plotted by increasing incidence angle for the corresponding acquisition. The oil slick is located across the range of incidence angles from $\sim 56^\circ$ to 67° in the image.

the surface, the upper limit of the average slick thickness is greater than $1 \mu\text{m}$. The actual thickness is likely to be lower, shown through modeling of slicks released in the same area on June 10 during another spill experiment and under higher wind conditions that indicate only $\sim 50\%$ of the released oil was on the surface a few hours after the release [70].

Wind and waves information was obtained from Météo-France, the French national meteorological service (POLLUPROOF'2015 campaign), and from the Norwegian Meteorological Institute (NOFO'2015 campaign) and is given in Table II.

The methodologies and the results presented in the following are based on SAR data collected by SETHI [27], the remote sensing imaging system developed by ONERA,

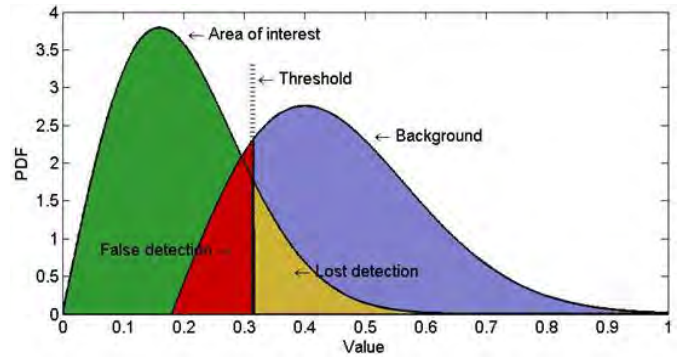


Fig. 6. Overview of histogram thresholding for ROC curve computation based upon separation of two classes.

as well as experimental data acquired by UAVSAR [28], the airborne sensor of JPL/NASA. Sections IV-A and IV-B briefly present the two SAR systems used here. Table III summarizes all SAR scenes investigated in this paper.

A. SETHI: Airborne Quad-Polarized SAR Sensor

SETHI is the ONERA airborne remote sensing laboratory designed to explore the science applications of remote sensing [27]. It is a pod-based system operating onboard a Falcon 20 Dassault aircraft flying at an altitude of 9000 ft. For both POLLUPROOF'2015 and NOFO'2015 campaigns, POLSAR data were acquired by SETHI at L-band, with a range resolution of 1 m (bandwidth from 1.25 to 1.4 GHz). Images are processed with an azimuth (along track) resolution equal to the range resolution. Imaged area is 9.5 km in azimuth and 1.5 km in range, with incidence angles from 34° to 52° . The instrument noise floor has been estimated using the method proposed in [71], and the results are shown in Fig. 4. The estimated noise equivalent sigma zero (NESZ) is very low, ranging from around -51 to $-53 \text{ dBm}^2/\text{m}^2$, allowing a sufficiently high SNR over slick-covered areas for valid analysis of surface characteristics. Examples of high-resolution polarization-dependent images acquired by SETHI at L-band are shown in Section V.

B. UAVSAR: Airborne Quad-Polarized SAR Sensor

During the NOFO'2015 experiment, UAVSAR (developed by NASA [28]) acquired POLSAR data at L-band over controlled releases of mineral oil at sea, flying at an altitude of 35100 ft. The data used in this analysis were acquired on June 9, 2015, within 5 min of SETHI and over the same area. They are processed with a resolution of 5 m in range and 7.2 m in azimuth (multilook format). The incidence angle ranges from 19.5° to 67.5° across the swath. The instrument

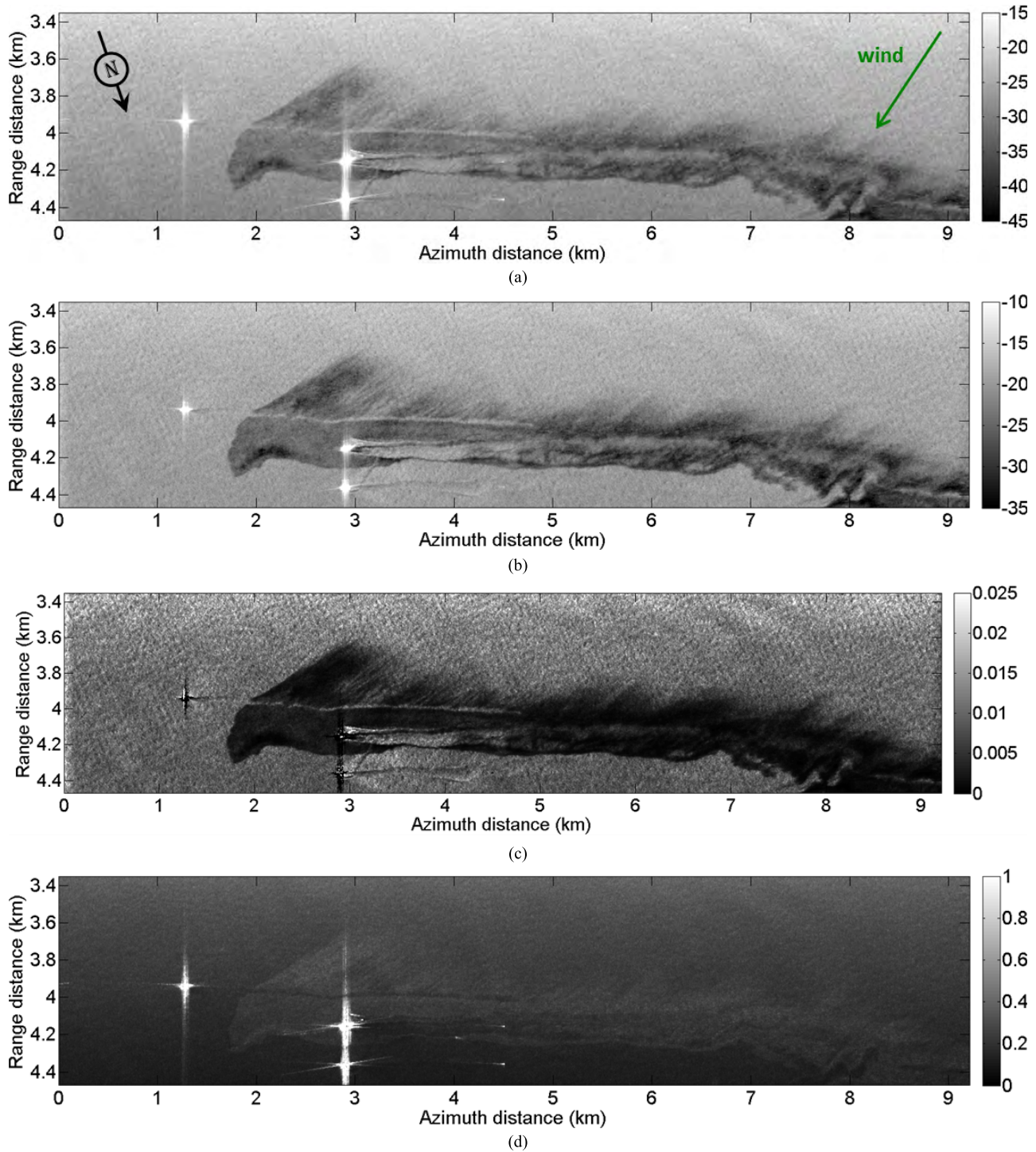


Fig. 7. SETHI NOFO'2015—L-band SAR data acquired over mineral oil released at sea—June 09, 2015, 10:01 UTC. (a) HH, (b) VV, (c) PD, and (d) PR quantities. Multilook $7 \text{ m} \times 7 \text{ m}$.

noise floor has been estimated using the same methodology as that used for the SETHI one [71], and it is shown in Fig. 5. The NESZ is very low, ranging from around -35 to $-51 \text{ dBm}^2/\text{m}^2$, allowing a sufficient SNR over sea surface covered by slicks for valid analysis of surface properties.

V. METHODOLOGY AND PERFORMANCE ASSESSMENT

We use receiver operating characteristic (ROC) [72] curves to characterize the detection capabilities of the

parameters discussed in Section III. This is an extension of the methodology published in [26] using a much larger data set and a more comprehensive set of parameters. ROC curves are obtained by plotting the probability of detection (Pd) against the probability of false alarm (Pfa), which quantifies the performance of a detector as its discrimination threshold is varied. In other words, ROC graphs depict the tradeoff between hit rates and false alarm rates of detectors [72]. The procedure, shown in Fig. 6, is as follows: we manually select areas of

clean sea surface (i.e., the background) and slick (i.e., the area of interest) and compute for each investigated parameter the histograms of values within the two regions. Then, for all possible values of the detection threshold, we calculate Pd as the fraction of samples within the area of interest that are below the threshold and Pfa as the fraction of samples in the background that are below the threshold. We will use these results to develop an instrument-independent ranking of the detection capabilities of each investigated parameter.

A. Sea Surface Slick Observation

We begin by evaluating the quad-pol SAR data acquired by SETHI (Fig. 7) over a controlled release of mineral oil (NOFO'2015 experiment). In Fig. 7, images of HH and VV channels are given as well as the PD and the PR maps. Visually, there is no significant difference between the cross-polarized and the co-polarized images, so the HV channel is not shown here. For these images, the wind direction is from the top right (see green arrow in Fig. 7(a); black arrow indicates the north direction). Wind information was obtained from the Norwegian Meteorological Institute and is given in Table II. The oil slick is observable as a dark area, with a ship's wake running through the slick. Within the lower part of the slick, the passage of a mechanical recovery boom (MOS sweeper [73]) appears to have left a relatively clean sea surface. Images show a feathered structure along the top of the slick (upwind) and a smooth edge on the downwind side of the slick, the expected appearance of the slick based on the wind direction.

Interestingly, while the upper limit of the slick thickness (greater than $1 \mu\text{m}$) has been estimated to be at least one-hundredth of the penetration depth at L-band (typically of the order of millimeters for water content greater than 50%—see Fig. 1), the mineral oil slick is observable in the PR images [Fig. 7(d)]. An explanation could be that there is a dielectric change due to the presence of oil in the water column that will impact the Polarization Ratio.

Low backscattering values from slick-covered areas can lead to low SNR values. Therefore, it is critical that we ensure sufficiently high SNR values before undertaking any analysis. SNR values along a transect through data obtained by SETHI during the NOFO'2015 experiment are shown in Fig. 8. The curves have been computed across a range transect at azimuth 2.1 km. The slick is between 3.85 km (incidence angle 44.2°) and 4.2 km (incidence angle 49.4°). The SNR values are high (even in cross-polarization), which enables polarimetric analysis of the surface properties.

B. Evaluation of Polarimetric Parameters for Slick Detection: Mineral Oil

We first focus on SAR data collected by SETHI over mineral oil spill (NOFO'2015 experiments). Fig. 9 shows areas selected for ROC curves computation where the uncontaminated sea surface (background) is outlined by the blue box and the contaminated area of interest is outlined by the red box. Note that the average SNR computed over the two regions (Table IV) is greater than 10 dB.

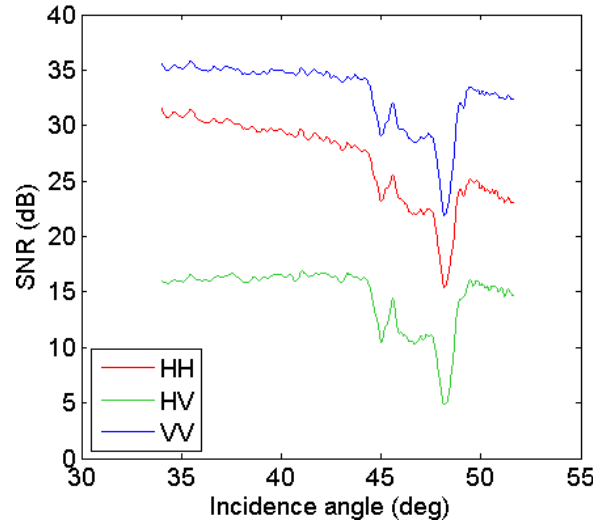


Fig. 8. SETHI signal-to-noise ratio (SNR) in polarization HH (red), HV (green), VV (blue)—range transect for azimuth 2.1 km (see Fig. 7)—June 09, 2015, 10:01 UTC.

ROC curves (Fig. 10) show that the Polarization Difference and VV are the most efficient parameters for mineral oil slick detection (i.e., for a given value of Pfa, they exhibit the greater value of Pd). The first eigenvalue (λ_1) is also very efficient for detecting slick-covered area, as it gives a performance of detection similar (slightly lower for low values of Pfa) to that obtained with VV and PD. They are then followed by the Hermitian Product between HH and VV (HP) and HH and HV. HV has good performance of detection and is even better than that of HH for low values of Pfa. This result for HV, which is consistent with the results obtained with UAVSAR data in stronger wind conditions obtained one day later (June 10) [57], is possible because of high SNR over the entire image. Then, we found that the Polarization Ratio and the studied quad-polarimetric parameters have low Pd values for all Pfa values. So, the co-pol coherence, the Bragg Likelihood Ratio, the Degree of Polarization, the Entropy, and the Conformity Coefficient are the parameters that give the worst performances of detection. These results seem to indicate that the same main scattering mechanism occurs over both contaminated and uncontaminated sea surface, namely, surface reflection and Bragg scattering [41]. To confirm this, we note that the polarimetric entropy, computed with a high SNR even over the polluted area, is low over both the clean sea surface and the slick; the mean entropy values are, respectively, equal to 0.18 and 0.17. This indicates that only one dominant scattering mechanism occurs, which confirms previous observations [56], [57] for the NOFO'2015 exercise and the original observation based on UAVSAR L-band data acquired over the Deepwater Horizon oil spill accident [41].

We now investigate SAR data collected with UAVSAR during the same NOFO'2015 experiment (mineral oil). As for SETHI, the UAVSAR instrument is characterized by a very low noise floor, which suggests a good complementarity of the results obtained with the two airborne sensors. The imaged ocean surface is the same as for the previous SETHI analysis (Fig. 9), and the time lag between the two

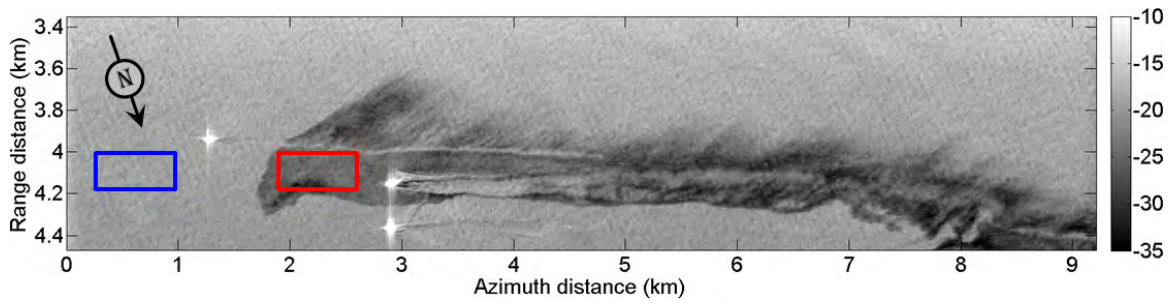


Fig. 9. Areas selected for ROC curve computation—blue box: clean sea surface and red box: slick area. SETHI, NOFO’2015 experiment, June 09, 2015, 10:01 UTC; VV channel; multilook 7 m × 7 m.

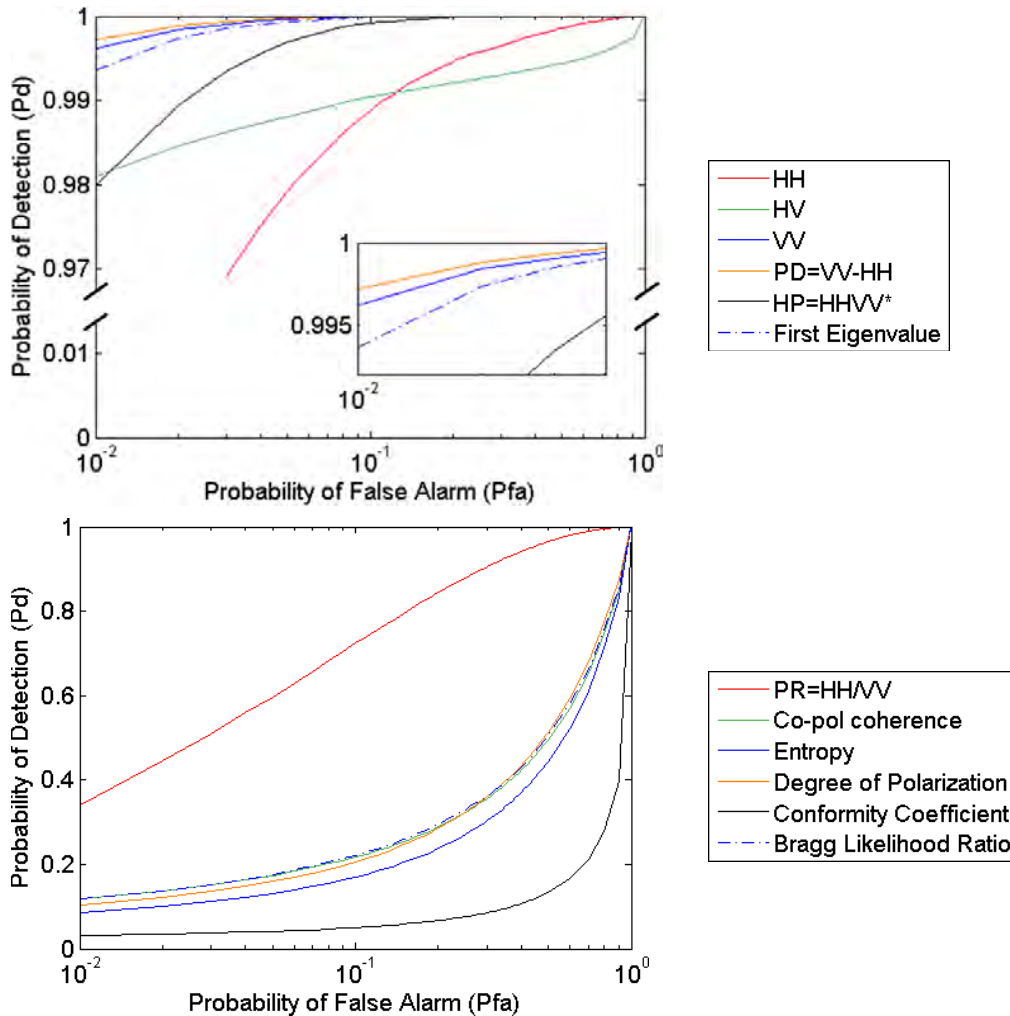


Fig. 10. SETHI, NOFO’2015 experiment, June 09, 2015, 10:01 UTC—Pd versus Pfa computed for all investigated parameters. Note the cut of the vertical axis on the top figure.

TABLE V
SIGNAL-TO-NOISE RATIO—UAVSAR, NOFO’2015 EXPERIMENT, JUNE 09, 2015, 09:56 UTC

Region	Incidence angle (deg)	HH	HV	VV
		MEAN [MIN MAX] dB	MEAN [MIN MAX] dB	MEAN [MIN MAX] dB
Clean sea	56.8°	14.8 [14.4 15.1] dB	9.4 [9.1 9.6] dB	23.7 [23.3 24.0] dB
Oil slick	56.8°	10.2 [10.0 10.4] dB	4.8 [4.5 5.0] dB	17.0 [16.7 17.4] dB

acquisitions is 5 min. For UAVSAR ROC graph analysis, the contaminated sea surface is close to that selected for SETHI (Figs. 9 and 11). Clean sea regions are selected to be at

the same range as the selected oil-covered areas, but they are in different places for SETHI and UAVSAR due to different flight directions. For the chosen regions of interest, the NESZ is

TABLE VI
SIGNAL-TO-NOISE RATIO—SETHI, POLLUPROOF'2015 EXPERIMENT, MAY 22, 2015, 16:07 UTC

Region	Incidence angle (deg)	HH	HV	VV
		MEAN [MIN MAX] dB	MEAN [MIN MAX] dB	MEAN [MIN MAX] dB
Clean sea	42.5°	30.7 [29.6 31.7] dB	18.7 [17.5 19.7] dB	36.6 [35.6 37.5] dB
Oil slick	42.5°	26.7 [25.9 27.5] dB	14.6 [13.5 15.8] dB	33.1 [32.2 33.8] dB

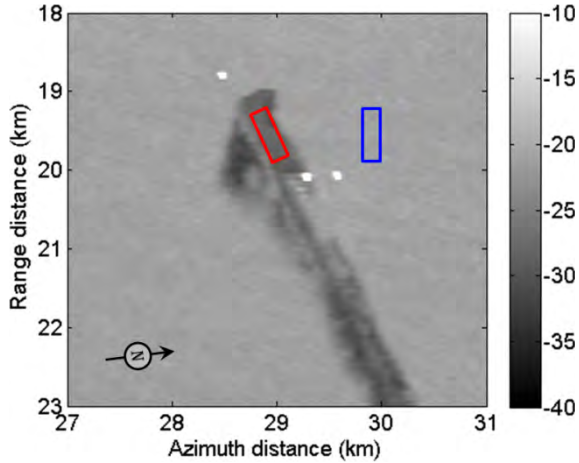


Fig. 11. Areas selected for ROC curve computation. Blue box: clean sea surface and red box: slick area. UAVSAR, NOFO'2015 experiment, June 09, 2015, 09:56 UTC—VV channel.

around $-45 \text{ dBm}^2/\text{m}^2$ (incidence angle around 57°). The SNR in the selected regions are given in Table V. As for SETHI, the levels are high ($>5 \text{ dB}$), which ensures a reliable analysis of surface backscatter over both slick-free and oil-covered sea surfaces. ROC graphs shown in Fig. 12 demonstrate that the best performance of detection is given by the cross-polarized channel (HV), followed by VV, the Polarization Difference, and the first eigenvalue (λ_1), then HH and the Hermitian Product between HH and VV (HP), and finally the conventional quad-polarimetric parameters of Entropy, Polarization Ratio, Degree of Polarization, dual-pol coherence, Bragg Likelihood Ratio and Conformity Coefficient. These results are very close to those obtained by SETHI.

C. Evaluation of Polarimetric Parameters for Slick Detection: Vegetable Oil

We now investigate Fatty Acid Methyl Esters (FAME) and rapeseed oil releases imaged by SETHI during the POLLUPROOF'2015 experiment (Fig. 13). Because of their physicochemical properties, these two substances have different behaviors once released into the ocean. FAME forms a cloud in the water column composed of microdroplets, and rapeseed oil forms a film on the surface [43]. These two behaviors have been highlighted in [43], using the oil–water mixing index introduced in [42].

The slick contains both substances. FAME appears on the left part of the spill and covers a surface of 0.29 km^2 [see red box in Fig. 13(a)]. Rapeseed oil corresponds to the right part of the spill [green box in Fig. 13(a)] and covers a surface of 1.26 km^2 . In between, there is a mixture of the two products [blue box in Fig. 13(a)]. From the amount

released product (1 m^3) and the area covered by the spill, the average thickness of the rapeseed oil spill is estimated to be equal to $0.8 \mu\text{m}$. This is approximately three orders of magnitude thinner than the penetration depth at L-band. Thus, the relative dielectric constant measured by the radar should be unaffected by the oil slick, and no signature of the rapeseed oil is observed in the Polarization Ratio image [Fig. 13(d)]. FAME, which mixes in the seawater column [43], slightly appears on the Polarization Ratio image, probably due to a decrease of the effective dielectric constant of this mixture compared to that of the surrounding clean sea area.

Clean sea surface and surface covered by rapeseed oil have been chosen and ROC curves computed for the selected areas. As for mineral oil analysis, the SNR is high (see Table VI), at least 14 dB , over both covered and free sea surfaces.

Similar to the results from mineral oil slicks, we observe (see Fig. 14) that for the rapeseed oil release, most of quad-polarimetric parameters (BLR, Entropy, and co-polarized coherence) give very poor performance of detection while amplitude channels are very powerful: HV gives the best performance of detection, followed closely by VV, the first eigenvalue (λ_1), HH, the Hermitian Product between HH and VV (HP), and the Polarization Difference (PD). As obtained above for mineral oil, we find here again that the Polarization Ratio (PR) and the conventional quad-polarimetric parameters (co-pol coherence, Bragg Likelihood Ratio, Degree of Polarization, Entropy and Conformity Coefficient) give the worst detection performance. We note finally that an identical ordering of the investigated parameters is obtained when selected sea surface contaminated by FAME instead of rapeseed oil (ROC curves not shown here).

This analysis, based on ROC graphs obtained with SAR data acquired by two airborne remote sensing sensors, both characterized by a very low instrument noise floor, demonstrate that, in the three cases shown, the VV and HV amplitude channels provide the best overall performance of detection. Sometimes, a slight improvement could be obtained with polarization-dependent parameters like the Polarization Difference.

Speckle affects the performances of detection, and multi-look is the most common method to reduce its effect. In this paper, we study the performances of detection offered by several polarization-dependent parameters, all calculated with the same window size, namely, multilooking by 7×7 in range and azimuth directions. The size of the window influences the detection performance of each of the parameters, but since the same window size is always used, the result obtained herein can be generalized to other window sizes.

When SAR data are collected with a very low NESZ, the backscattered signal is not corrupted by noise, the EM wave is well polarized, and only one scattering mechanism

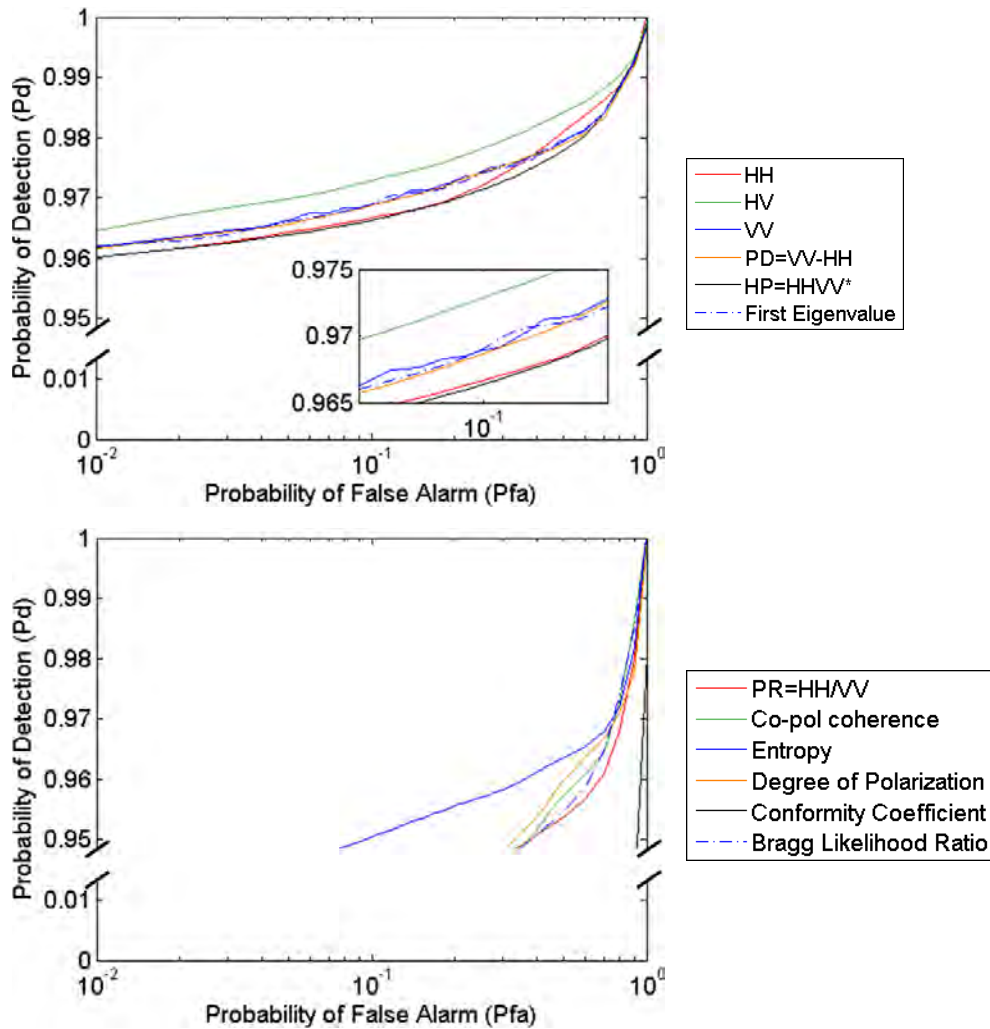


Fig. 12. UAVSAR, NOFO'2015 experiment, June 09, 2015, 09:56 UTC—Pd versus Pfa computed for all investigated parameters. Note the cut of the vertical axis on both figures.

occurs over both clean and contaminated sea surface (low entropy values over both surfaces). When the SNR over slick-covered area is not as high as with the airborne acquisitions analyzed here, as for the spaceborne SARs available today, the instrument noise must be considered when evaluating the performance of detection of polarimetric parameters. Section V-D focuses on the influence of instrument noise.

D. Instrument Noise Effect

To study how the NESZ impacts the ROC curves obtained for the investigated features, we added increasing levels of Gaussian white noise, from 5 to 30 dB, to the raw SAR data collected by SETHI during the NOFO'2015 experiment. We then processed the noisier data using the standard processing software (Fig. 15). We note that when the noise is increased by 15 dB [Fig. 15(d)], its detrimental effect in the VV image is apparent. When 30 dB of noise is added, the slick is no longer observable in the VV image [Fig. 15(f)].

We now assess the detection performance for all simulated instrument noise levels. ROC curves are computed over the areas shown in Fig. 9. The results for some selected

radar quantities are given in Fig. 16, and conclusions are as follows.

- 1) For a given Pfa, Pd for HH, VV, and HV decreases as SNR decreases. When the additive noise is less than or equal to 10 dB, the ROC curves are largely unchanged.
- 2) For a given Pfa, Pd increases for the polarimetric parameters for additive noise values less than 20 dB. Then, performance of detection decreases with greater levels of additive noise.

Thus, in contrast to the amplitude values, the Pd for the polarimetric parameters increases with the instrument noise so long as the SNR is sufficiently high over clean sea surface (~ 15 dB added noise) and then decreases for decreasing SNR. As the SNR decreases, the received signal is increasingly corrupted by noise and the combined noise plus scattered EM signal becomes randomly polarized (DoP goes to 0 and Entropy goes to 1 as the total signal approaches noise only). With sufficiently high noise levels, both contaminated and uncontaminated sea surfaces will appear randomly polarized and no further separation between the two regions is possible. SNR values as well as mean values of DoP and Entropy over

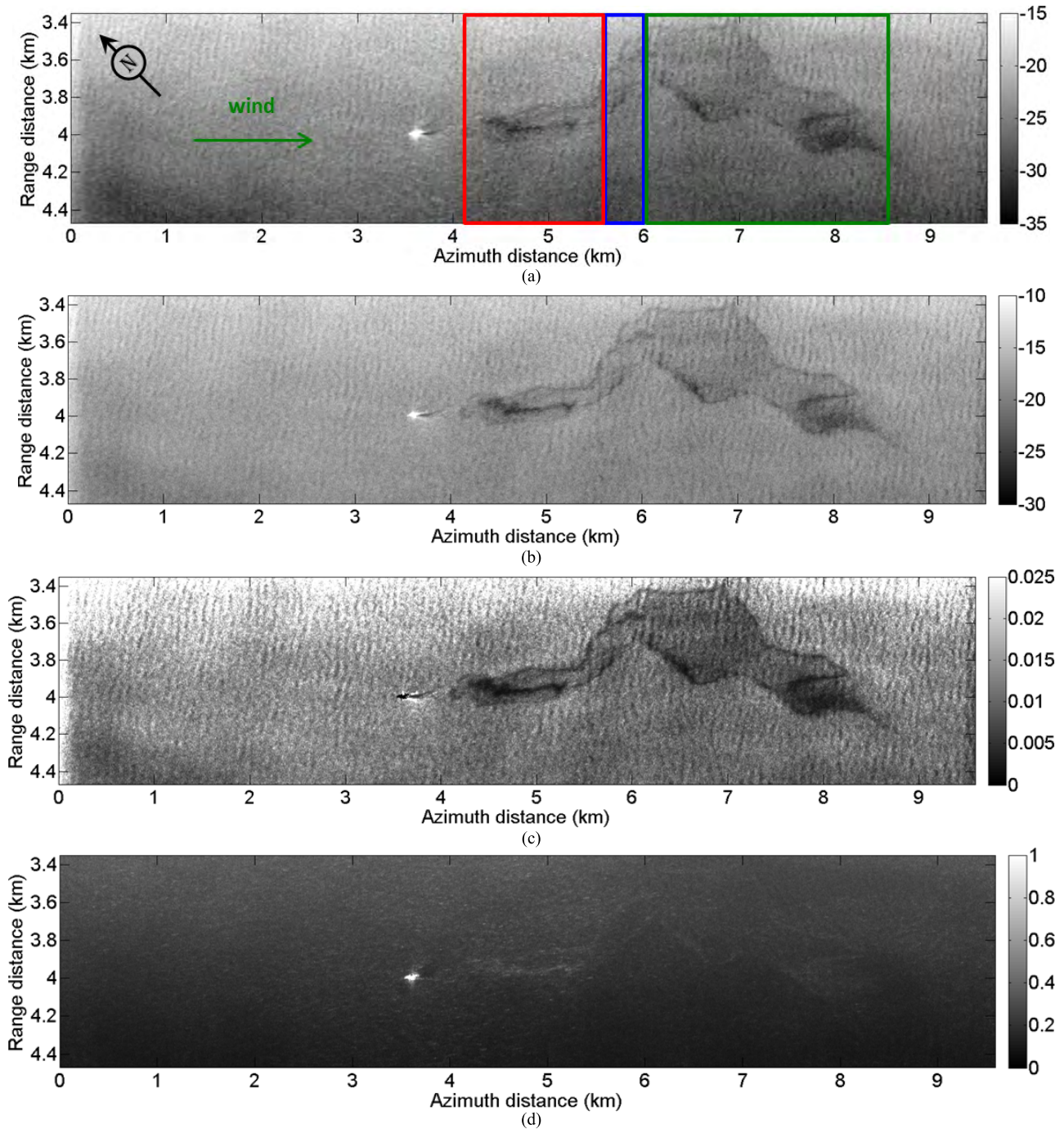


Fig. 13. SETHI POLLUPROOF*2015—L-band SAR data—May 22, 2015, 16:07 UTC. (a) HH, (b) VV, (c) PD, and (d) PR quantities—multilook $7 \text{ m} \times 7 \text{ m}$. FAME is indicated by the red box and rapeseed oil by the green box, and the blue box corresponds to a mixture between the two products.

clean sea and the oil slick are given in Tables VII and VIII. Despite the increase in Pd with increasing noise component for the polarimetric parameters, the Pd remains highest for the single-polarization HH and VV parameters at any given level of added noise. For a noise level increased by less than 20 dB, HV has higher Pd than all polarimetric parameters.

VI. DISCUSSION

Our analysis of L-band SAR data collected by SETHI and UAVSAR, two airborne sensors that have low instrument noise floor, allows us to formulate the following ordering

of polarization-dependent parameters for region-based slick detection, whether vegetable films or mineral oil slicks.

- 1) *Group 1*: VV, HV, the Polarization Difference (PD), and the first eigenvalue (λ_1).
- 2) *Group 2*: HH and the Hermitian Product between HH and VV (HP).
- 3) *Group 3*: The Entropy (H), the Polarization Ratio (PR), the Degree of Polarization (DoP), the co-polarized coherence (ρ_{HHVV}), the Bragg Likelihood Ratio (BLR), and the Conformity Coefficient (μ).

The parameters in the first group all provide high performance of detection based on the ROC curve results. The presence

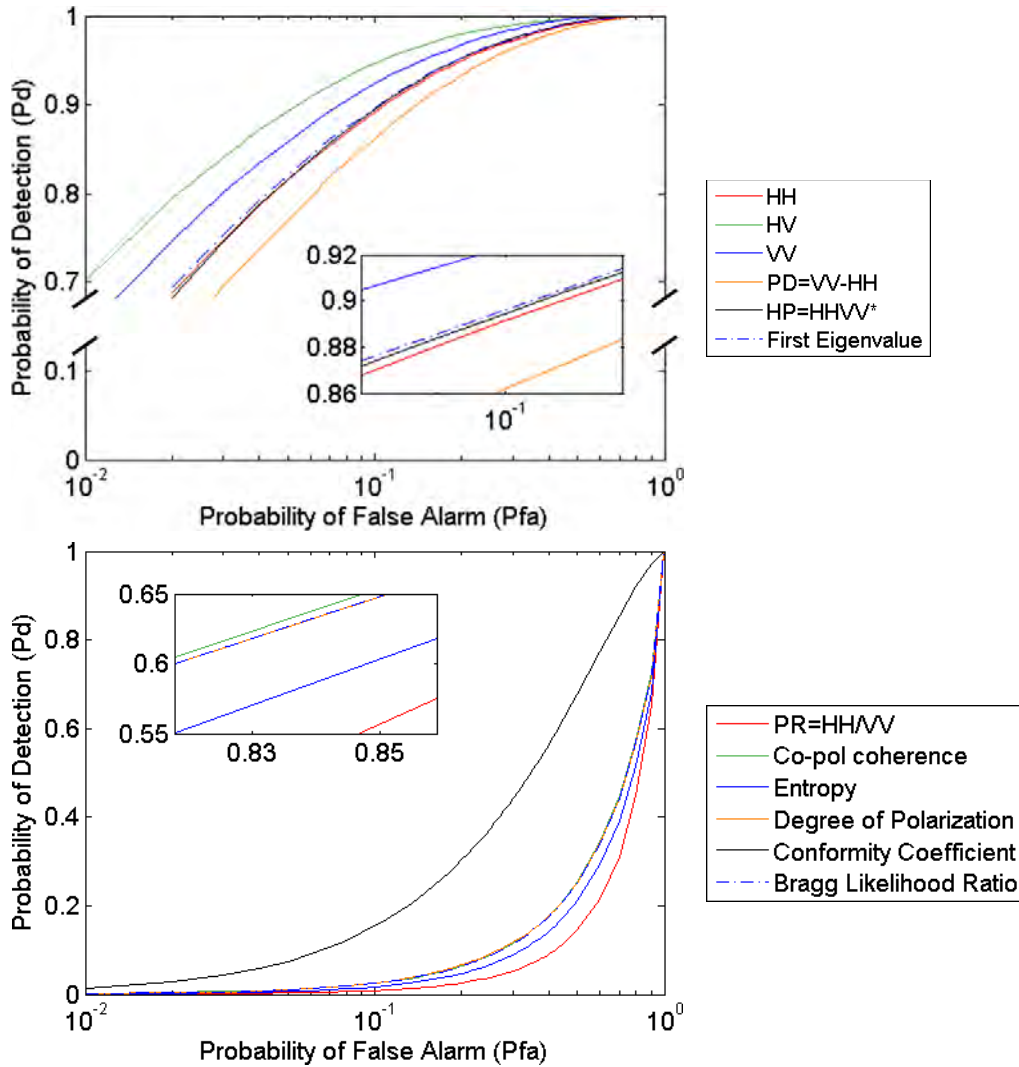


Fig. 14. SETHI, POLLUPROOF²2015 experiment, May 22, 2015, 16:07 UTC—Pd versus Pfa computed for all investigated parameters. Note the cut of the vertical axis on the top figure.

TABLE VII
SIGNAL-TO-NOISE RATIO—SETHI, NOFO²2015 EXPERIMENT, JUNE 09, 2015, 10:01 UTC

Region	Noise added	HH	HV	VV
Clean sea	Original data	26.5 dB	16.4 dB	34.1 dB
	5 dB	21.5 dB	11.4 dB	29.1 dB
	10 dB	16.5 dB	6.4dB	24.1 dB
	15 dB	11.5 dB	1.4 dB	19.1 dB
	20 dB	6.5 dB	-3.6 dB	14.1 dB
	30 dB	-3.5 dB	-13.6 dB	4.1 dB
Oil slick	Original data	21.5 dB	10.2 dB	28.0 dB
	5 dB	16.5 dB	5.2 dB	23.0 dB
	10 dB	11.5 dB	0.2 dB	18.0 dB
	15 dB	6.5 dB	-4.8 dB	13.0 dB
	20 dB	1.5 dB	-9.8 dB	8.0 dB
	30 dB	-8.5 dB	-19.8 dB	-2.0 dB

of each parameter in group 1 can be understood through the Bragg scattering model. In this framework, VV always has the highest amplitude and HH and VV have different reflectivities, ensuring that PD takes positive values. In the

tilted-Bragg-scattering model, HV can have a nonzero amplitude that is always less than both HH and VV. As a result, the first eigenvalue of the covariance matrix is dominated by VV and, to a lesser extent, HH. The control

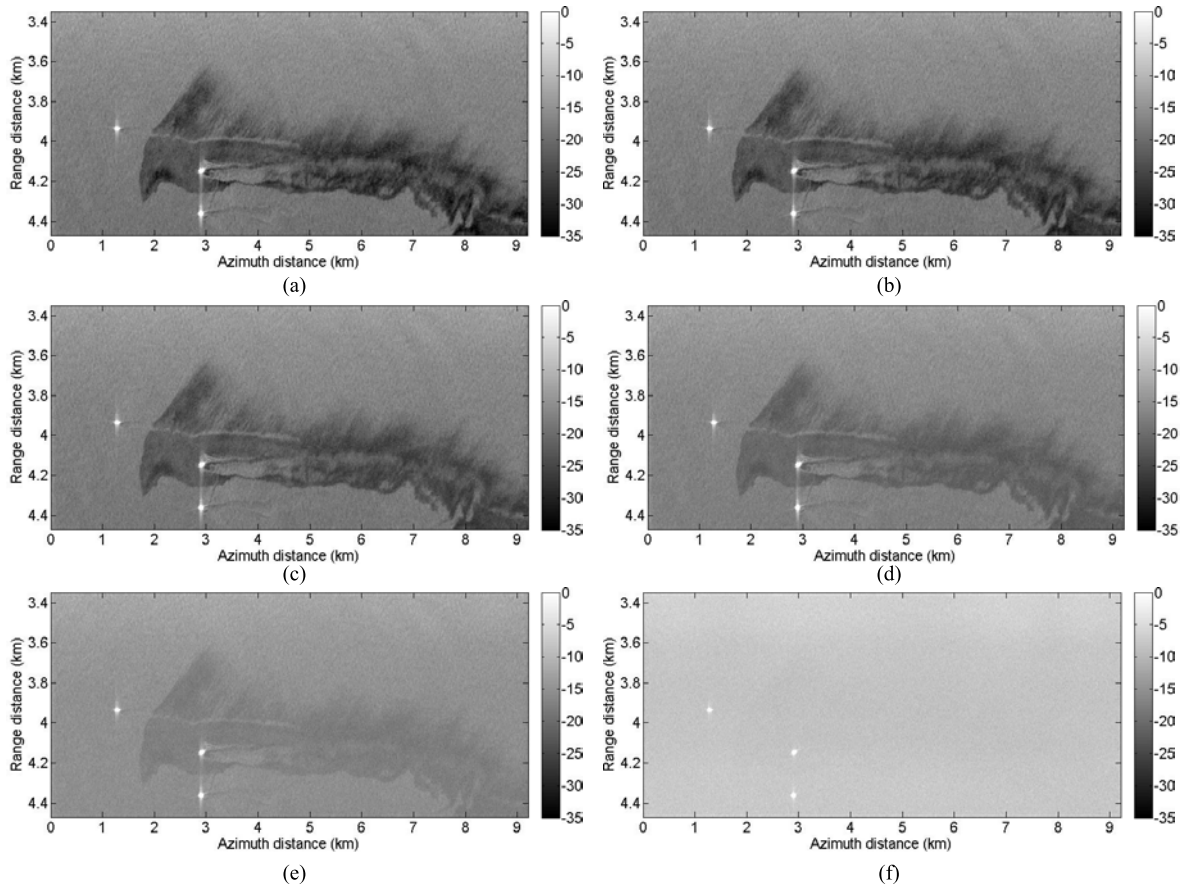


Fig. 15. Noise effect—SETHI polarization VV. (a) Original data and instrument noise increased by (b) 5 dB, (c) 10 dB, (d) 15 dB, (e) 20 dB, and (f) 30 dB—NOFO’2015 experiment, June 09, 2015, 10:01 UTC.

TABLE VIII
DoP AND ENTROPY—SETHI, NOFO’2015 EXPERIMENT,
JUNE 09, 2015, 10:01 UTC

Region	Noise added	DoP	Entropy
Clean sea	Original data	0.94	0.17
	5 dB	0.93	0.19
	10 dB	0.9	0.24
	15 dB	0.84	0.34
	20 dB	0.75	0.46
	30 dB	0.67	0.56
Oil slick	Original data	0.92	0.18
	5 dB	0.88	0.25
	10 dB	0.81	0.36
	15 dB	0.72	0.48
	20 dB	0.67	0.55
	30 dB	0.66	0.57

of VV on the value of the first eigenvalue explains why the first eigenvalue is a high-performing parameter. As previously reported in [57], HV performs well where the instrument noise floor is low because, to a good approximation in the tilted-Bragg model, the HV amplitude is proportional to PD.

The second group of parameters, composed of HH and the Hermitian Product between HH and VV channels, gives good performance of detection, although slightly lower than the performance of group 1. We show that HH channel is slightly less effective than VV for slick detection. However, we emphasize

that HH is effective for distinguishing slicks from relatively clean sea surfaces. HP suffers from the decrease in detection performance of HH compared to that of VV.

We place all remaining parameters in group 3, which has the worst capabilities of detection. The parameters in group 3 are the Polarization Ratio (PR), the co-polarized coherence (ρ_{HHVV}), the Bragg Likelihood Ratio (BLR), the Entropy (H), the Degree of Polarization (DoP) and the Conformity Coefficient (μ). For these parameters, detection performance seems to be very strongly correlated with the instrument noise and their applicability in a sea pollution detection scheme is instrument dependent. For a sufficiently high SNR, the EM wave backscattered by the slick-free sea surface remains well polarized (DoP close to 1 and Entropy close to 0). It becomes less polarized over the contaminated area (DoP decreases and Entropy increases) and the performances of detection increase. When the instrument noise becomes a significant fraction of the measured signal (low SNR), the apparent backscattered signal becomes randomly polarized for contaminated and uncontaminated sea surfaces, and no further separation between the two regions is possible. The instrument noise issue for oil spill detection using quad-polarimetric SAR data has been recently addressed in [15]. In this paper, the authors hypothesize that the often-stated claims that non-Bragg scattering occurs over slick-covered areas is due to a misinterpretation of SAR images collected with too low an SNR. Our study presented in this paper is in agreement with this hypothesis and goes even further since,

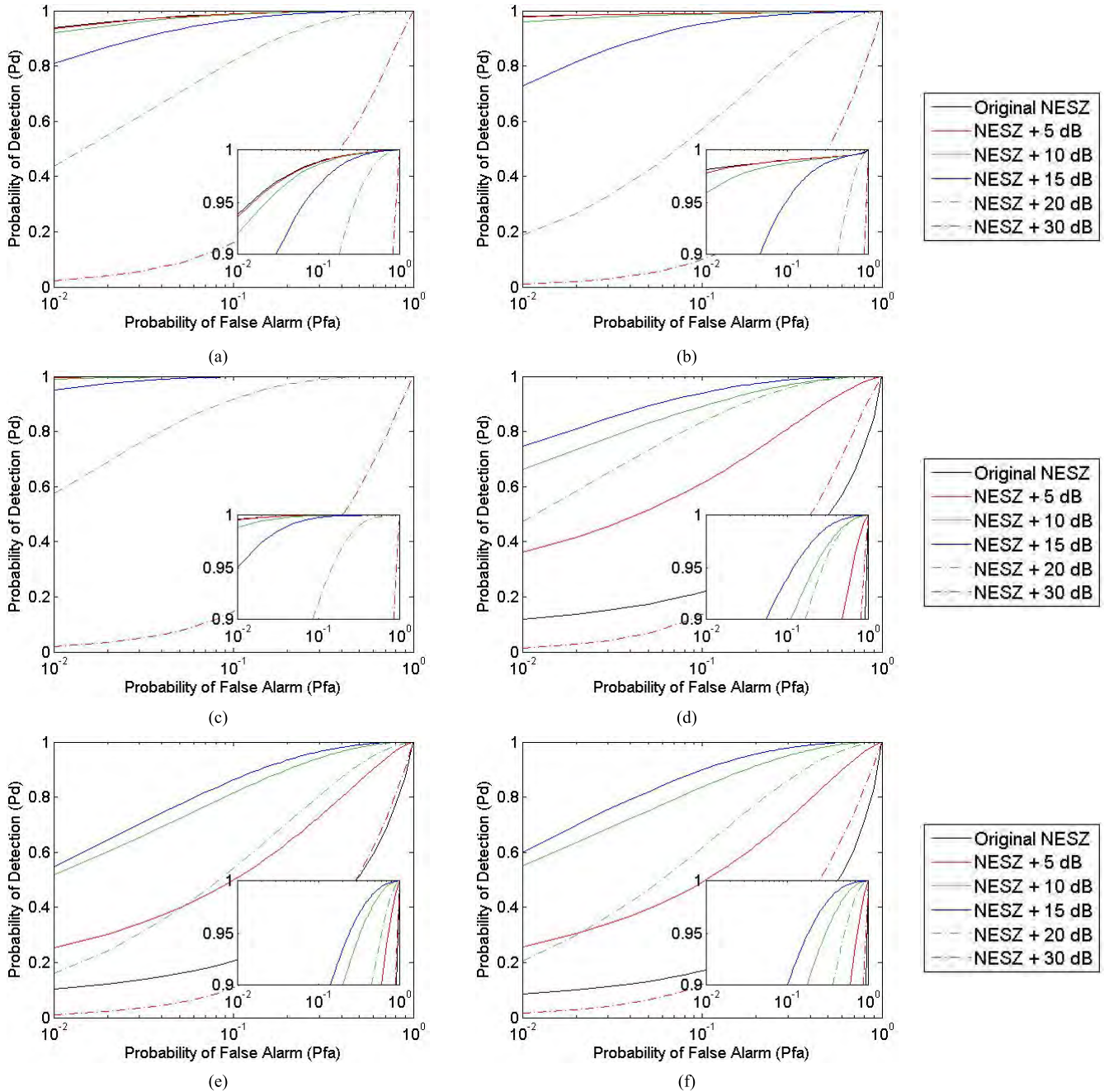


Fig. 16. Noise effect on ROC curves—SETHI (a) HH, (b) HV, (c) VV, (d) dual-pol coherence, (e) DoP, and (f) Entropy—NOFO’2015 experiment, June 09, 2015, 10:01 UTC.

for the first time, we quantify in a systematic way the effect of instrument noise on polarization-dependent SAR parameters when applied to oil spill detection. As previously reported in [15] and [41], we demonstrate that there is no deviation from Bragg scattering for radar scattering from ocean surface covered by mineral and vegetable oil.

The hierarchy that we propose here is obtained from L-band airborne SAR data collected over vegetable and mineral oil slick released during moderate wind conditions. A similar study is proposed in [56] and [57], with [57] evaluating the parameters during transport and evolution of mineral and plant slicks. The major differences between all these studies are the proposed method of measuring the capabilities of detection

of different quantities investigated and the fact that the slicks studied in [56] and [57] were thinner, formed from the release of 0.2–0.5 m³ of material rather than 45 m³ as the slick in our study. In [56], SAR data acquired by UAVSAR, TerraSAR-X, and RADARSAT-2 at nearly the same time over mineral oil spills under high-wind conditions are investigated using many of the same parameters as herein. They found likewise that VV intensity is the most efficient parameter for the detection of oil slick on sea surface. The HV channel was not investigated in [56] because of the low SNR of the satellite data. The UAVSAR image investigated in [56] is also studied in [57], combined with 17 other images covering the evolving slicks over an 8-h period. In the latter, the proposed methodology

to order the polarimetric parameters is slightly different than in [56], and the authors also found that VV intensity is very efficient for slick–sea discrimination. The HV channel was studied in [57] and, similar to our results, those authors found that the cross-polarized channel is attractive for slick detection over ocean surface when employed SAR data are acquired with a very low instrument noise floor. Comparing [56], [57], and the results that we report here, there is a clear consensus on the use of VV or HV channels for slick detection at sea. The main difference between results obtained in this paper and those reported in [56] and [57] concerns the performances of detection given by the Polarization Difference. Indeed, we found here, and as already reported in [17], [33], [43], and [54], that the Polarization Difference is one of the most efficient parameters for slick–sea discrimination. This difference could be due to different wind conditions, sea state, or slick thicknesses, and highlights the complexity of slick detection across a range of variables under which they can occur.

VII. CONCLUSION

To guide the selection of the most appropriate SAR imaging mode for marine pollution detection, a methodology based on the analysis of ROC curves has been reported in this paper. The ROC analysis accounts for the non-Gaussian tails of the probability distribution of parameter values, which are particularly important for the slick-covered areas. We compare the probabilities of detecting a slick with the probabilities of a false alarm for a range of detection thresholds to rank various polarization-dependent parameters in the order of slick-detection performance, from best to worst. A key aspect of the results reported in this paper lies in the analysis of the instrument noise effect on the performance of detection offered by the studied parameters. This is done by progressively adding Gaussian white noise directly to the raw SAR data and then processing the noisier data using the standard processing software. The other important aspects of this paper derive from three factors: the quantitative evaluation of a dozen common parameters used for detecting marine slicks; the uniqueness of the studied data set collected by two airborne sensors operating at L-band, both of which are characterized by an instrument noise floor that is much lower than the one that is currently available from spaceborne SARs; and the evaluation of detectability of both vegetable and mineral oil slicks with the same low-noise instrument. Low noise makes the parameters more sensitive to the surface properties and less influenced by the sensor.

We find that HV amplitude can outperform all other investigated amplitudes and polarimetric settings whenever the instrument noise is sufficiently low (at least 5 dB in this paper). However, as instrument noise increases, HV amplitude and all polarimetric parameters that rely on HV become corrupted by the noise and their slick-detection performance diminishes. HV is closely followed by the investigated co-polarized settings (ordered as follows: VV, the Polarization Difference, HH, and the Hermitian Product between HH and VV), while being more robust to a lower SNR than the cross-polarized channel.

We note that this relative ordering is determined from a single combined set of sea state, meteorological conditions, and slick properties, and further work is needed to expand to other conditions, in particular lower wind speeds and different slick thicknesses.

For detecting slicks on the sea surface, we propose that VV parameter offers the best tradeoff between the benefit of detection performance and the instrument and data requirements.

We find that the co-pol amplitudes (HH and VV) and two polarimetric parameters, the Polarization Difference and the first eigenvalue of the quad-pol covariance matrix, are more robust in the presence of instrument noise than the cross-pol (HV) amplitude and quad-polarimetric parameters. This disparity in robustness is due to higher co-pol amplitudes relative to the cross-pol amplitude and the strong impact of instrument noise on POLSAR parameters. This implies that polarimetric quantities which combine the four polarimetric channels have performances of detection mainly driven by the instrument noise level (NESZ).

ACKNOWLEDGMENT

The authors would like to thank the Norwegian Clean Seas Association for Operating Companies (NOFO), Norway, for allowing them to participate in the oil-on-water exercise, which was carried out during June 8, 2015–June 14, 2015. They would like to thank everyone involved in the experiment at sea and those who participated in SAR data processing. They would also like to thank H. Oriot from ONERA, Palaiseau, France, for his thoughtful discussions about receiver operating characteristic curve computation. This research was carried out in part at the Jet Propulsion Laboratory, California Institute of Technology, Pasadena, CA, USA, under contract with the U.S. National Aeronautics and Space Administration (NASA). The UAVSAR data are courtesy of the NASA/Jet Propulsion Laboratory and are openly available through the Alaska Satellite Facility (<http://asf.alaska.edu>).

REFERENCES

- [1] M. Fingas and C. Brown, “Review of oil spill remote sensing,” *Marine Pollution Bull.*, vol. 83, no. 1, pp. 9–23, 2014.
- [2] C. Brekke and A. H. S. Solberg, “Oil spill detection by satellite remote sensing,” *Remote Sens. Environ.*, vol. 95, no. 1, pp. 1–13, 2005.
- [3] O. Garcia-Pineda *et al.*, “Detection of floating oil anomalies from the Deepwater Horizon oil spill with synthetic aperture radar,” *Oceanography*, vol. 26, no. 2, pp. 124–137, 2013.
- [4] H. A. Espedal, “Satellite SAR oil spill detection using wind history information,” *Int. J. Remote Sens.*, vol. 20, no. 1, pp. 49–65, Jan. 1999.
- [5] H. A. Espedal, O. M. Johannessen, J. A. Johannessen, E. Dano, D. R. Lyzenga, and J. C. Knulst, “COASTWATCH’95: ERS 1/2 SAR detection of natural film on the ocean surface,” *J. Geophys. Res.*, vol. 103, no. C11, pp. 24969–24982, 1998.
- [6] M. Gade and W. Alpers, “Using ERS-2 SAR images for routine observation of marine pollution in European coastal waters,” *Sci. Total Environ.*, vols. 237–238, pp. 441–448, Sep. 1999.
- [7] O. Garcia-Pineda, B. Zimmer, M. Howard, W. Pichel, X. Li, and I. R. MacDonald, “Using SAR images to delineate ocean oil slicks with a texture-classifying neural network algorithm (TCNNA),” *Can. J. Remote Sens.*, vol. 35, no. 5, pp. 411–421, Oct. 2009.
- [8] F. Girard-Ardhuin, G. Mercier, F. Collard, and R. Garello, “Operational oil-slick characterization by SAR imagery and synergistic data,” *IEEE J. Ocean. Eng.*, vol. 30, no. 3, pp. 487–495, Jul. 2005.

- [9] A. D. Jenkins and K. B. Dysthe, "The effective film viscosity coefficients of a thin floating fluid layer," *J. Fluid Mech.*, vol. 344, pp. 335–337, Aug. 1997.
- [10] A. D. Jenkins and A. S. Jacobs, "Wave damping by a thin layer of viscous fluid," *Phys. Fluids*, vol. 9, no. 5, pp. 1256–1264, 1997.
- [11] K. P. Singh, A. L. Gray, R. K. Hawkins, and R. A. O'Neil, "The influence of surface oil on c-and ku-band ocean backscatter," *IEEE Trans. Geosci. Remote Sens.*, vol. GE-24, no. 5, pp. 738–744, Sep. 1986.
- [12] G. R. Valenzuela, "Theories for the interaction of electromagnetic and oceanic waves—A review," *Boundary-Layer Meteorol.*, vol. 13, nos. 1–4, pp. 61–85, Jan. 1978.
- [13] M. Migliaccio, F. Nunziata, and A. Buono, "SAR polarimetry for sea oil slick observation," *Int. J. Remote Sens.*, vol. 36, no. 12, pp. 3243–3273, 2015.
- [14] A. H. S. Solberg, "Remote sensing of ocean oil-spill pollution," *Proc. IEEE*, vol. 100, no. 10, pp. 2931–2945, Oct. 2012.
- [15] W. Alpers, B. Holt, and K. Zeng, "Oil spill detection by imaging radars: Challenges and pitfalls," *Remote Sens. Environ.*, vol. 201, pp. 133–147, Nov. 2017.
- [16] M. Migliaccio, F. Nunziata, and A. Gambardella, "On the co-polarized phase difference for oil spill observation," *Int. J. Remote Sens.*, vol. 30, no. 6, pp. 1587–1602, 2009.
- [17] M. W. Hansen, V. Kudryavtsev, B. Chapron, C. Brekke, and J. A. Johannessen, "Wave breaking in slicks: Impacts on C-band quad-polarized SAR measurements," *IEEE J. Sel. Topics Appl. Earth Observ. Remote Sens.*, vol. 9, no. 11, pp. 4929–4940, Nov. 2016.
- [18] M. Gade, W. Alpers, H. Hühnerfuss, H. Masuko, and T. Kobayashi, "Imaging of biogenic and anthropogenic ocean surface films by the multifrequency/multipolarization SIR-C/X-SAR," *J. Geophys. Res.*, vol. 103, no. C9, pp. 18851–18866, 1998.
- [19] R. Touzi, F. J. Charbonneau, R. K. Hawkins, and P. W. Vachon, "Ship detection and characterization using polarimetric SAR," *Can. J. Remote Sens.*, vol. 30, no. 3, pp. 552–559, 2004.
- [20] F. Nunziata, A. Gambardella, and M. Migliaccio, "On the Mueller scattering matrix for SAR sea oil slick observation," *IEEE Geosci. Remote Sens. Lett.*, vol. 5, no. 4, pp. 691–695, Oct. 2008.
- [21] M. Migliaccio, A. Gambardella, F. Nunziata, M. Shimada, and O. Isoguchi, "The PALSAR polarimetric mode for sea oil slick observation," *IEEE Trans. Geosci. Remote Sens.*, vol. 47, no. 12, pp. 4032–4041, Dec. 2009.
- [22] D. Velotto, M. Migliaccio, F. Nunziata, and S. Lehner, "Dual-polarized TerraSAR-X data for oil-spill observation," *IEEE Trans. Geosci. Remote Sens.*, vol. 49, no. 12, pp. 4751–4762, Dec. 2011.
- [23] R. Shirvany, M. Chabert, and J. Y. Tourneret, "Ship and oil-spill detection using the degree of polarization in linear and hybrid/compact dual-pol SAR," *IEEE J. Sel. Topics Appl. Earth Observ. Remote Sens.*, vol. 5, no. 3, pp. 885–892, Jun. 2012.
- [24] F. Nunziata, A. Gambardella, and M. Migliaccio, "On the degree of polarization for SAR sea oil slick observation," *ISPRS J. Photogramm. Remote Sens.*, vol. 78, pp. 41–49, Apr. 2013.
- [25] S. Skrunes, C. Brekke, and T. Eltoft, "Characterization of marine surface slicks by radarsat-2 multipolarization features," *IEEE Trans. Geosci. Remote Sens.*, vol. 52, no. 9, pp. 5302–5319, Sep. 2014.
- [26] A.-B. Salberg, O. Rudjord, and A. H. S. Solberg, "Oil spill detection in hybrid-polarimetric SAR images," *IEEE Trans. Geosci. Remote Sens.*, vol. 52, no. 10, pp. 6521–6533, Oct. 2014.
- [27] S. Angelliaume, X. Ceamanos, F. Viallefont-Robinet, R. Baqué, P. Déliot, and V. Miegbielle, "Hyperspectral and radar airborne imagery over controlled release of oil at sea," *Sensors*, vol. 17, no. 8, p. 1772, 2017.
- [28] S. Hensley *et al.*, "The UAVSAR instrument: Description and first results," in *Proc. IEEE Radar Conf.*, Rome, Italy, May 2008, pp. 1–6.
- [29] K. D. Ward, R. J. A. Tough, and S. Watts, *Sea Clutter: Scattering, the K Distribution and Radar Performance*, 2nd ed. Herts, U.K.: IET, 2013.
- [30] F. T. Ulaby, R. K. Moore, and A. K. Fung, *Microwave Remote Sensing: Active and Passive: Radar Remote Sensing and Surface Scattering and Emission Theory*, vol. 2. Dedham, MA, USA: Artech House, 1986.
- [31] Y. Quilfen, B. Chapron, A. Bentamy, J. Gourrion, T. El Fouhailly, and D. Vandemark, "Global ERS 1 and 2 and NSCAT observations: Upwind/crosswind and upwind/downwind measurements," *J. Geophys. Res. Oceans*, vol. 104, no. C5, pp. 11459–11469, May 1999.
- [32] J. Horstmann, W. Koch, S. Lehner, and R. Tonboe, "Wind retrieval over the ocean using synthetic aperture radar with C-band HH polarization," *IEEE Trans. Geosci. Remote Sens.*, vol. 38, no. 5, pp. 2122–2131, Sep. 2000.
- [33] V. N. Kudryavtsev, B. Chapron, A. G. Myasoedov, F. Collard, and J. A. Johannessen, "On dual co-polarized SAR measurements of the ocean surface," *IEEE Geosci. Remote Sens. Lett.*, vol. 10, no. 4, pp. 761–765, Jul. 2013.
- [34] V. Kudryavtsev, D. Hauser, G. Caudal, and B. Chapron, "A semiempirical model of the normalized radar cross section of the sea surface, 2. Radar modulation transfer function," *J. Geophys. Res.*, vol. 108, no. C3, pp. 2156–2202, 2003.
- [35] B. Holt, "SAR imaging of the ocean surface," in *Synthetic Aperture Radar (SAR) Marine User's Manual*, C. R. Jackson and J. R. Apel, Eds. Silver Spring, MD, USA: NOAA, 2004, pp. 263–275.
- [36] K. Hasselmann *et al.*, "Theory of synthetic aperture radar ocean imaging: A MARSEN view," *J. Geophys. Res.*, vol. 90, no. C3, pp. 4659–4686, 1985.
- [37] G. R. Valenzuela, "Scattering of electromagnetic waves from a tilted slightly rough surface," *Radio Sci.*, vol. 3, no. 11, pp. 1057–1066, Nov. 1968.
- [38] T. Meissner and F. J. Wentz, "The complex dielectric constant of pure and sea water from microwave satellite observations," *IEEE Trans. Geosci. Remote Sens.*, vol. 42, no. 9, pp. 1836–1849, Sep. 2004.
- [39] K. Folgerø, "Bilinear calibration of coaxial transmission/reflection cells for permittivity measurement of low-loss liquids," *Meas. Sci. Technol.*, vol. 7, no. 9, pp. 1260–1269, 1996.
- [40] T. Friisø, Y. Schildberg, O. Rambeau, T. Tjomsland, H. J. Førdedal, and J. Sjøblom, "Complex permittivity of crude oils and solutions of heavy crude oil fractions," *J. Dispersion Sci. Technol.*, vol. 19, no. 1, pp. 93–126, 1998.
- [41] B. Minchew, C. E. Jones, and B. Holt, "Polarimetric analysis of backscatter from the Deepwater Horizon oil spill using L-band synthetic aperture radar," *IEEE Trans. Geosci. Remote Sens.*, vol. 50, no. 10, pp. 3812–3830, Oct. 2012.
- [42] B. Minchew, "Determining the mixing of oil and sea water using polarimetric synthetic aperture radar," *Geophys. Res. Lett.*, vol. 39, no. 16, p. L16607, 2012.
- [43] S. Angelliaume, B. Minchew, S. Chataing, P. Martineau, and V. Miegbielle, "Multifrequency radar imagery and characterization of hazardous and noxious substances at sea," *IEEE Trans. Geosci. Remote Sens.*, vol. 55, no. 5, pp. 3051–3066, May 2017.
- [44] *Bonn Agreement Aerial Surveillance Handbook*, Bonn Agreement, London, U.K., 2004, p. 96.
- [45] *Bonn Agreement Aerial Surveillance Handbook*, Bonn Agreement, London, U.K., 2009, p. 106.
- [46] I. Leifer *et al.*, "State of the art satellite and airborne marine oil spill remote sensing: Application to the BP Deepwater Horizon oil spill," *Remote Sens. Environ.*, vol. 124, pp. 185–209, Sep. 2012.
- [47] M. Fingas and B. Fieldhouse, "Studies on water-in-oil products from crude oils and petroleum products," *Marine Pollution Bull.*, vol. 64, no. 2, pp. 272–283, 2012.
- [48] Z. H. Shah and Q. A. Tahir, "Dielectric properties of vegetable oils," *J. Sci. Res.*, vol. 3, no. 3, pp. 481–492, Aug. 2011.
- [49] U. Erle, M. Regier, C. Persch, and H. Schubert, "Dielectric properties of emulsions and suspensions: Mixture equations and measurement comparisons," *J. Microw. Power Electromagn. Energy*, vol. 35, no. 3, pp. 185–190, 2000.
- [50] W. Alpers and H. A. Espedal, "Oils and surfactants," in *Synthetic Aperture Radar Marine User's Manual*, C. R. Jackson and J. R. Apel, Eds. Washington, DC, USA: U.S. Department of Commerce, National Oceanic and Atmospheric Administration, 2004, ch. 11, pp. 263–275.
- [51] V. Wismann, M. Gade, W. Alpers, and H. Hühnerfuss, "Radar signatures of marine mineral oil spills measured by an airborne multifrequency radar," *Int. J. Remote Sens.*, vol. 19, no. 18, pp. 3607–3623, 1998.
- [52] M. Gade, W. Alpers, H. Hühnerfuss, V. Wismann, and P. Lange, "On the reduction of the radar backscatter by oceanic surface films: Scatterometer measurements and their theoretical interpretation," *Remote Sens. Environ.*, vol. 66, no. 1, pp. 52–70, Oct. 1998.
- [53] D. Latini, F. Del Frate, and C. E. Jones, "Multi-frequency and polarimetric quantitative analysis of the Gulf of Mexico oil spill event comparing different SAR systems," *Remote Sens. Environ.*, vol. 183, pp. 26–42, Sep. 2016.
- [54] D. V. Ivonin, S. Skrunes, C. Brekke, and A. Y. Ivanov, "Interpreting sea surface slicks on the basis of the normalized radar cross-section model using RADARSAT-2 copolarization dual-channel SAR images," *Geophys. Res. Lett.*, vol. 43, no. 6, pp. 2748–2757, 2016.

- [55] S. Skrunes, C. Brekke, T. Eltoft, and V. Kudryavtsev, "Comparing near-coincident C- and X-band SAR acquisitions of marine oil spills," *IEEE Trans. Geosci. Remote Sens.*, vol. 53, no. 4, pp. 1958–1975, Apr. 2015.
- [56] S. Skrunes, C. Brekke, C. E. Jones, and B. Holt, "A multisensor comparison of experimental oil spills in polarimetric SAR for high wind conditions," *IEEE J. Sel. Topics Appl. Earth Observ. Remote Sens.*, vol. 9, no. 11, pp. 4948–4961, Nov. 2016.
- [57] M. M. Espeseth, S. Skrunes, C. E. Jones, C. Brekke, B. Holt, and A. P. Doulgeris, "Analysis of evolving oil spills in full-polarimetric and hybrid-polarity SAR," *IEEE Trans. Geosci. Remote Sens.*, vol. 59, no. 7, pp. 4190–4210, Jul. 2017.
- [58] M. Gade, W. Alpers, H. Hühnerfuss, and P. A. Lange, "Wind wave tank measurements of wave damping and radar cross sections in the presence of monomolecular surface films," *J. Geophys. Res.*, vol. 103, no. C2, pp. 3167–3178, 1998.
- [59] C.-A. Guérin, G. Soriano, and B. Chapron, "The weighted curvature approximation in scattering from sea surfaces," *Waves Random Complex Media*, vol. 20, no. 3, pp. 364–384, 2010.
- [60] H. A. Zebker, J. J. van Zyl, and D. N. Held, "Imaging radar polarimetry from wave synthesis," *J. Geophys. Res.*, vol. 92, no. B1, pp. 683–701, Jan. 1987.
- [61] W. J. Plant, E. A. Terray, R. A. Petitt, Jr., and W. C. Keller, "The dependence of microwave backscatter from the sea on illuminated area: Correlation times and lengths," *J. Geophys. Res.*, vol. 99, no. C5, pp. 9705–9723, May 1994.
- [62] A. S. Milman, A. O. Scheffler, and J. R. Bennett, "A theory of the synthetic aperture radar images of time-dependent scenes," *J. Geophys. Res.*, vol. 98, no. C1, pp. 911–925, Jan. 1993.
- [63] W. Born and E. Wolf, *Principles of Optics*. New York, NY, USA: Pergamon, 1959.
- [64] W.-M. Boerner *et al.*, "Polarimetric in radar remote sensing: Basic and applied concepts," in *Principles and Applications of IMAGING RADAR*, vol. 2. Hoboken, NJ, USA: Wiley, 1998.
- [65] R. Touzi, W.-M. Boerner, J.-S. Lee, and E. Lueneburg, "A review of polarimetry in the context of synthetic aperture radar: Concepts and information extraction," *Can. J. Remote Sens.*, vol. 30, no. 3, pp. 380–407, 2004.
- [66] B. Zhang, W. Perrie, X. Li, and W. B. Pichel, "Mapping sea surface oil slicks using RADARSAT-2 quad-polarization SAR image," *Geophys. Res. Lett.*, vol. 38, no. 10, p. L10602, 2011.
- [67] M.-L. Truong-Loi, P. Dubois-Fernandez, A. Freeman, and E. Pottier, "The conformity coefficient or how to explore the scattering behaviour from compact polarimetry mode," in *Proc. IEEE Radar Conf.*, Pasadena, CA, USA, May 2009, pp. 1–6.
- [68] S. R. Cloude and E. Pottier, "A review of target decomposition theorems in radar polarimetry," *IEEE Trans. Geosci. Remote Sens.*, vol. 34, no. 2, pp. 498–518, Mar. 1996.
- [69] S. R. Cloude and E. Pottier, "An entropy based classification scheme for land applications of polarimetric SAR," *IEEE Trans. Geosci. Remote Sens.*, vol. 35, no. 1, pp. 68–78, Jan. 1997.
- [70] C. E. Jones *et al.*, "Measurement and modeling of oil slick transport," *J. Geophys. Res. Oceans*, vol. 121, no. 10, pp. 7759–7775, 2016.
- [71] I. Hajnsek, E. Pottier, and S. R. Cloude, "Inversion of surface parameters from polarimetric SAR," *IEEE Trans. Geosci. Remote Sens.*, vol. 41, no. 4, pp. 727–744, Apr. 2003.
- [72] J. P. Egan, *Signal Detection Theory and ROC Analysis* (Cognition and Perception). New York, NY, USA: Academic, 1975.
- [73] *MOS Sweeper—Egersund Group*. Accessed: Jan. 23, 2018. [Online]. Available: <http://www.egersundgroup.no/oilspill/mos-sweeper>



Sébastien Angelliaume received the Engineering degree from the Ecole Nationale Supérieure d'Ingénieur de Constructions Aéronautiques, Toulouse, France, and the M.S. degree from the Ecole Nationale Supérieure d'Electrotechnique, d'Electronique, d'Informatique, d'Hydraulique et des Télécommunications, Toulouse, both in 2003.

Since 2006, he has been with the Electromagnetism and Radar Department, Office National d'Etudes et de Recherches Aérospatiales (ONERA—the French Aerospace Lab), Salon de Provence, France, where he has been involved in the ONERA synthetic aperture radar airborne platforms RAMSES and SETHI, developing science applications. Since 2010, his research at ONERA has focused mainly on remote sensing over the ocean surface.



Pascale C. Dubois-Fernandez (A'04–M'04–SM'04) received the Diplôme d'Ingenieur degree from the Ecole Nationale Supérieure d'Ingénieur de Constructions Aéronautiques, Toulouse, France, in 1983, and the M.S. and Eng. degrees from the California Institute of Technology, Pasadena, CA, USA, in 1984 and 1986, respectively.

She was with the Radar Science and Technology Group, Jet Propulsion Laboratory, Pasadena, CA, USA, where she stayed for ten years, participating in numerous programs such as Magellan, AIRSAR, and SIR-C. She then moved back to France, where she focused on cartographic applications of satellite data. In 2000, she joined the Electromagnetism and Radar Department, Office National d'Etudes et de Recherches Aérospatiales (ONERA—the French Aerospace Lab), Salon de Provence, France, where she has been involved in the ONERA synthetic aperture radar (SAR) airborne platform, RAMSES, developing science applications as the SAR civilian remote sensing expert.



Cathleen E. Jones received the B.S. degree in physics from Texas A&M University, College Station, TX, USA, and the Ph.D. degree in physics from the California Institute of Technology, Pasadena, CA, USA.

She is currently a Radar Scientist with NASA's Jet Propulsion Laboratory, California Institute of Technology, Pasadena, CA, USA, where her main research is focused on using radar remote sensing for studying natural disasters and monitoring critical infrastructure, primarily using high-resolution L-band PolSAR and InSAR based on UAVSAR data. Her research interests include development of methods for determining oil slick characteristics and identifying levee deformation, seepage, and general subsidence rates using synthetic aperture radar (SAR), and detection of sinkhole precursors in InSAR-challenged areas.



Benjamin Holt received the B.S. degree from Stanford University, Stanford, CA, USA, in 1972, and the M.S. degree in physical oceanography from the University of Southern California, Los Angeles, CA, USA, in 1988.

In 1978, he joined the Ocean Circulation Group, Earth Science Section, Jet Propulsion Laboratory, California Institute of Technology, Pasadena, CA, USA, where he is currently a Research Scientist. His research interests include using multisensor remote sensing data to examine the geophysical state of polar sea ice and snow, coastal oceanography and circulation, the detection of marine pollutants, new instrument development, and techniques for microwave measurement of sea ice thickness.



Brent Minchew received the B.Sc. and M.Sc. degrees in aerospace engineering from the University of Texas at Austin, Austin, TX, USA, in 2008 and 2010, respectively, and the Ph.D. degree in geophysics from the California Institute of Technology, Pasadena, CA, USA.

From 2016 to 2018, he was an NSF Postdoctoral Fellow at the British Antarctic Survey, Cambridge, U.K. He is currently an Assistant Professor with the Department of Earth, Atmospheric and Planetary Sciences, Massachusetts Institute of Technology, Cambridge, MA, USA. His research interests include remote sensing applications and environmental fluid dynamics, with an emphasis on glacier mechanics.



Emna Amri was born in Tunis, Tunisia, in 1990. She received the Engineering degree in computer science and the master's degree in intelligent systems in imaging and artificial vision from the University of Tunis El Manar, Tunis, in 2015 and 2017, respectively.

Her research interests include computer vision, machine learning, and remote sensing.



Véronique Miegebielle received the Geology Doctorate degree with a specialization in remote sensing from Pau and Pays de l'Adour University, Pau, France, in 1993.

She spent the first 15 years of her career, dealing with geology and environmental subjects. In 2009, she moved on to take care of Remote Sensing Service at Total, Pau. Since 2011, she has been in charge of remote sensing offshore research project.

SAR Imagery for Detecting Sea Surface Slicks: Performance Assessment of Polarization-Dependent Parameters

Sébastien Angelliaume[✉], Pascale C. Dubois-Fernandez, *Senior Member, IEEE*, Cathleen E. Jones, Benjamin Holt, Brent Minchew, Emna Amri, and Véronique Miegebielle

Abstract—Remote sensing technology is an essential link in the global monitoring of the ocean surface, and radars are efficient sensors for detecting marine pollution. When used operationally by authorities, a tradeoff must usually be made between the covered area and the quantity of information collected by the radar. To identify the most appropriate imaging mode, a methodology based on receiver operating characteristic curve analysis has been applied to an original data set collected by two airborne systems operating at L-band, both characterized by a very low instrument noise floor. The data set was acquired during controlled releases of mineral and vegetable oil at sea. Various polarization-dependent quantities are investigated, and their ability to detect slick-covered areas is assessed. A relative ordering of the main polarimetric parameters is reported in this paper. When the sensor has a sufficiently low noise floor, HV is recommended because it provides the strongest slick-sea contrast. Otherwise, VV is found to be the most relevant parameter for detecting slicks on the ocean surface. Among all the investigated quad-polarimetric settings, no significant added value compared to single-polarized data was found. More specifically, it is demonstrated, by increasing the instrument noise level, that the studied polarimetric quantities which combine the four polarimetric channels have performances of detection mainly driven by the instrument noise floor, namely, the noise equivalent sigma zero. This result, obtained by progressively adding noise to the raw synthetic aperture radar (SAR) data, indicates that the polarimetric discrimination between clean sea and polluted area results mainly from the differentiated behavior between single-bounce scattering and noise. It is thus demonstrated, using SAR data collected with a low instrument noise floor, that there is no deviation from Bragg scattering for radar scattering from ocean surface covered by mineral and vegetable oil.

Index Terms—Bragg, detection, instrument noise, marine pollution, noise, noise equivalent sigma zero (NESZ), noise floor, ocean, oil, polarimetric discrimination, polarization, probability of detection (Pd), probability of false alarm (Pfa), radar, ranking,

Manuscript received October 11, 2017; revised December 20, 2017 and January 26, 2018; accepted January 28, 2018. This work was supported in part by the French National Research Agency (ANR) through the POLLUPROOF Research Program under Grant ANR-13-ECOT-007 and in part by the New Advanced Observation Method Integration Project, a common research program between Total (the French Petroleum Company) and ONERA (the French Aerospace Lab). (*Corresponding author: Sébastien Angelliaume.*)

S. Angelliaume, P. C. Dubois-Fernandez, and E. Amri are with ONERA, DEMR, 13661 Salon de Provence, France (e-mail: sebastien.angelliaume@onera.fr).

C. E. Jones and B. Holt are with the Jet Propulsion Laboratory, California Institute of Technology, Pasadena, CA 91109 USA.

B. Minchew is with British Antarctic Survey, Cambridge CB3 0ET, U.K.

V. Miegebielle is with the Remote Sensing Department, Total, 64018 Pau, France.

Color versions of one or more of the figures in this paper are available online at <http://ieeexplore.ieee.org>.

Digital Object Identifier 10.1109/TGRS.2018.2803216

receiver operating characteristic (ROC) curves, synthetic aperture radar (SAR), sea, slick, spill.

I. INTRODUCTION

SPACEBORNE and airborne remote sensing sensors are commonly used in the offshore domain for monitoring natural and anthropogenic oil slicks [1]–[3]. These sensors allow the authorities and the petroleum companies to monitor sea shipping lanes to identify possible fuel releases, respond to incidents occurring at surface or subsurface oil and gas facilities, and identify the occurrence of natural hydrocarbons (seeps) on the sea surface [4]–[6], testifying to the presence of mature source rock on the ocean bottom.

Because of the constraints linked mainly to weather conditions and the risk of significant cloud cover, the use and programming of synthetic aperture radar (SAR) data is usually favored over optical imagery for oil slick detection over the ocean surface [6]–[8]. SAR is a powerful tool for detecting hydrocarbons or chemicals on the sea surface because of the sensitivity of the electromagnetic (EM) scattering to surface roughness. In calm seas, most of the transmitted energy is reflected away from the radar and the backscattered signal toward the instrument is very low. Wind-driven roughness increases the total backscattered energy from the surface. Oil films on the sea surface damp the capillary and short gravity waves [9], [10], which are the main source of sea surface roughness. As a consequence, slicks appear as dark areas in the SAR image (low backscattered signal), which makes the presence of an oil slick on the sea surface detectable in radar imagery.

Several major issues are identified in the success of hydrocarbon detection in the offshore domain, the first of which remains today, namely, the revisit time. Indeed, in an emergency situation, obtaining quick information from spaceborne sensors is decisive. The latency is constrained by the repeat orbit interval of SAR satellite systems, the trajectory of the orbits, the location of the area of interest (e.g., there are more possibilities of acquisition daily at high latitudes than that toward the equator), the data recording and downlink system, and the SAR viewing geometry agility [11]. Thus, very large swath modes are often selected by maritime surveillance services to the detriment of the spatial resolution or to the amount of information potentially collected over the area of interest, for example, with polarimetric modes. Monitoring

services exploit mainly radar remote sensing data acquired in a single-polarization mode, maximizing the covered surface of the ocean. Due to a higher backscattered signal level from the sea surface for vertically (V) polarized waves than that for horizontal (H) polarization [12], the VV channel is often preferred to HH for ocean studies. Because most of the spaceborne SAR systems available today have a moderate noise floor (between -20 and -35 dBm²/m² [13]), the cross-polarization (HV or VH) channels have not been used for operational ocean slick detection.

The second major issue affecting the success of offshore hydrocarbon detection concerns the speed of data analysis coupled with the reliability of hydrocarbon detection. Operationally, the analysis of SAR images is mostly based on the visual identification of dark areas corresponding to oil slicks [14]. Many oceanic and atmospheric phenomena can occur over the sea surface and manifest themselves on radar images in the same way as areas covered by hydrocarbons. These are called look-alikes, and they can originate from several sources [15]: 1) natural biogenic surface films produced by fish or plankton; 2) young and thin sea ice; 3) low-wind areas; and 4) upwelling of cold water. For decades, Alpers *et al.* [15], Migliaccio *et al.* [16], and Hansen *et al.* [17] have attempted to develop methodologies to differentiate ocean areas covered by hydrocarbon from look-alikes. Today, the discrimination between biogenic films and mineral oil slicks remains an active area of research [15]. The method of conventional operational SAR analysis is mainly based on the experience and expertise of the image interpreter. In order to facilitate visual inspection, there have been many studies of the SAR signature of hydrocarbons observed in different acquisition configurations in order to identify the optimal detection method. Regarding the choice of sensor, the reliability of detection depends mainly on the frequency band and the sensor noise floor. For example, it has been demonstrated in [18] that SAR images acquired at high frequency (e.g., X- or C-band) are preferable to those acquired at lower frequency (e.g., L-band) for mineral oil slick detection. In parallel with system considerations, it is essential to know what information is most relevant for detection, especially information that can be obtained from the polarization of the EM waves. Because many studies published in the literature have suggested that multipolarization (dual-polarization or quad-polarization) or polarimetric (POLoSAR, i.e., using both amplitude and phase information) parameters improve the detection capability of slicks compared to single-polarization data [19]–[26], exploring various polarization-dependent SAR parameters accessible in the range of possible SAR acquisition configurations is a valuable aid to operational teams in ranking the acquisition modes that can be used.

The aim of this paper is to present a prioritization of SAR parameters to enhance and facilitate slick detection in the offshore domain. The originality of the proposed method lies in the definition and quantitative evaluation of parameters calculated using data obtained in quad-polarimetric mode by two airborne SARs operating at L-band (1.275 and 1.325 GHz) with very high signal-to-noise ratio (SNR) over controlled releases of mineral and vegetable oil at sea. These two sensors are Système Expérimental de Télédétection Hyperfréquence

Imageur (SETHI) operated by ONERA [27], the French Aerospace Lab, and Uninhabited Aerial Vehicle Synthetic Aperture Radar (UAVSAR) operated by National Aeronautics and Space Administration (NASA)/Jet Propulsion Laboratory (JPL) [28].

This paper is organized as follows. Section II presents the basis of the radar scattering from the ocean surface. Section III summarizes the state-of-the-art POLoSAR parameters proposed in the literature for slick detection. Section IV describes the airborne SAR data used in this paper. Section V presents the methodology used to evaluate the studied parameters and gives the results, and main discussions are presented in Section VI.

II. RADAR SCATTERING FROM THE OCEAN SURFACE

Over a rough sea surface where Bragg scattering is dominant (incidence angles in the so-called “plateau region” [29], ranging from around 30° to 60°), the co-polarized channels (HH and VV) have higher backscattered power than that of the cross-polarized (HV and VH) channels. Higher backscattered power means higher SNR, which makes these channels more attractive for slick detection on the sea surface where typical backscattered power can be low [17]. The co-polarized radar backscattered power is proportional to the normalized radar cross section (NRCS), which is defined in the Bragg scattering theory [12] as

$$\sigma_{pp}^0 = 4\pi k_{EM}^4 \cos^4 \theta_i \Gamma_{pp} W(k_B) \quad (1)$$

$$k_B = 2k_{EM} \sin \theta_i \quad (2)$$

where subscript p denotes either H (horizontal) or V (vertical) polarization; $k_{EM} = 2\pi/\lambda_{EM}$ is the EM wavenumber corresponding to the radar wavelength λ_{EM} ; Γ_{pp} is the reflectivity; $W(k_B)$ is the spectral density of ocean surface roughness evaluated at the Bragg wavenumber k_B ; and θ_i is the radar local incidence angle. The spectral density of the sea surface describes the components of the ocean wave spectrum that contribute to the scattering of the radar pulses [30], while the reflectivity describes the total power scattered from the surface.

This formulation of the NRCS (1) does not fully explain the EM signal backscattered by a rough sea surface because it takes into account only the polarized components of the backscattering from the ocean surface. Deviations between model estimation (Bragg theory) and real observation [31], [32] are often explained through nonresonant mechanisms, called non-Bragg or nonpolarized effects [33]. Those mechanisms are generally associated with breaking waves or whitecaps, and they contribute to the total backscattered energy from the sea surface. However, the contribution of non-Bragg scattering to the total NRCS is frequency dependent, and it has been reported in [34] that at low EM frequency (e.g., L-band), the relative contribution of this non-polarized component with respect to the total power scattered from the ocean surface is negligible. For this reason, we do not consider nonpolarized effects in the rest of this paper.

The local incidence angle of the EM wave θ_i is defined [12] as

$$\theta_i = \cos^{-1}[\cos(\theta + \psi) \cos \xi] \quad (3)$$

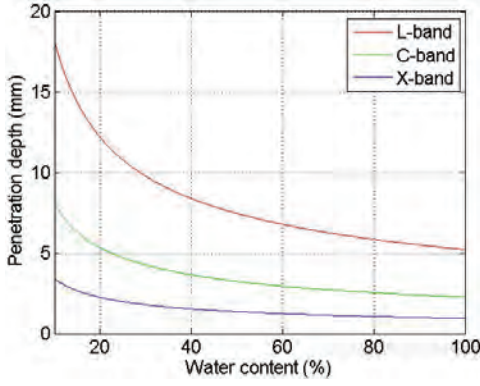


Fig. 1. Penetration depth as a function of water content (volumetric percentage) based on a linear mixing model for the dielectric constant at L-band (red), C-band (green), and X-band (blue); dielectric constants are specified in Table I.

where θ is the EM angle of incidence relative to the local, untilted surface vertical direction and ψ and ζ are defined in the following paragraph.

The sea surface is modeled as a set of slightly rough tilted facets that contributes to the backscattering of the incident radiation. Each facet has superimposed small-scale surface roughness that creates a Bragg scatterer when the roughness scale is commensurate with the radar wavelength. Small-scale roughness is randomly distributed on the scattering surface and responds to the strength of local wind, which generates capillary and short gravity waves whose wavelengths are of the order centimeters to decimeters with periods less than 1 s [35]. The tilt of the facet is caused by larger scale gravity waves on the ocean surface that change the local orientation, or tilt, of the short waves [36]. The orientation of the facet of the sea surface is defined by two angles: ψ , which is the angle between local up and the projection of the facet normal onto the radar scattering plane (in-plane tilt), and ζ , which is the angle between local up and the projection of the facet normal onto the vertically oriented plane perpendicular to the scattering plane (out-of-plane tilt) (see [37, Fig. 1]).

The co-polarized reflectivity Γ_{pp} is a function of the local geometry and the electrical properties of the scattering surface (e.g., seawater and films) such that

$$\Gamma_{pp} = \left| \left(\frac{\sin(\theta + \psi) \cos \zeta}{\sin \theta_i} \right)^2 \alpha_{pp} + \left(\frac{\sin \zeta}{\sin \theta_i} \right)^2 \alpha_{qq} \right|^2 \quad (4)$$

where subscript $q (p \neq q)$ denotes either H or V polarization. The co-polarized Bragg scattering coefficients, introduced in (4), are defined [12] as

$$\alpha_{HH} = \frac{\cos \theta_i - \sqrt{\varepsilon_r - \sin^2 \theta_i}}{\cos \theta_i + \sqrt{\varepsilon_r - \sin^2 \theta_i}} \quad (5)$$

$$\alpha_{VV} = \frac{(\varepsilon_r - 1)(\sin^2 \theta_i - \varepsilon_r(1 + \sin^2 \theta_i))}{(\varepsilon_r \cos \theta_i + \sqrt{\varepsilon_r - \sin^2 \theta_i})^2} \quad (6)$$

They depend only on the local incidence angle of the EM wave θ_i and the complex-valued relative dielectric constant of the imaged surface ε_r .

TABLE I
DIELECTRIC CONSTANT OF SEAWATER FROM [38] AND
MINERAL OIL FROM [39] AND [40]

Material	L-BAND [1.3 GHz]	C-BAND [5.0 GHz]	X-BAND [10 GHz]
Seawater (15°C 35 PSU)	73.0+65.1i	66.8+35.7i	52.9+39.0i
Mineral oil	2.3+0.01i	2.3+0.01i	2.3+0.01i

The relative dielectric constant ε_r defined as the ratio between the material dielectric constant and the electric constant in a vacuum is a complex number. Its value is material dependent and varies with the radar frequency. The imaginary part characterizes how far an EM wave can penetrate into a conducting medium. The penetration depth δ_p is defined as the depth where the power of the propagating EM wave is attenuated by a factor of $1/e$ such that

$$\delta_p = \frac{1}{2k_{EM} \text{Im}(\sqrt{\varepsilon_r})} \quad (7)$$

where $\text{Im}(\cdot)$ selects the imaginary part of a complex number. Typical values of dielectric constant of seawater [38] and mineral oil [39], [40] are given in Table I. Note that the value of the dielectric constant for mineral oil is nearly constant in the range 1–10 GHz, with a loss factor (imaginary component) close to 0, suggesting a nonnegligible penetration of the EM wave through this medium.

Assuming a linear mixing model, the effective dielectric constant of a water-in-oil emulsion (ε_{em}) is given by

$$\varepsilon_{em} = v\varepsilon_w + (1 - v)\varepsilon_{oil} \quad (8)$$

where v , ranging from 0 to 1, is the water content by volume of the oil–water mixture, and ε_w and ε_{oil} are the relative dielectric constants of seawater and oil, respectively. It follows from (8) that the effective dielectric constant of a mixture of oil and seawater is lower than that of seawater alone [41]. From values given in Table I and from (7) and (8), it is seen that the penetration depth decreases with increasing frequency and water content, with typical penetration depth of the order of millimeters for water content greater than 50% (Fig. 1).

When hydrocarbons are spilled into a marine environment, the oil can be mixed with seawater within the upper few centimeters of the water column or can behave like a viscoelastic film floating on the surface. In the first case, mixing of oil with seawater will lead to a reduction of the relative dielectric constant of the contaminated sea surface compared to the surrounding slick-free area. This will contribute to a decrease in the total radar backscattered power, along with suppression of the Bragg-wavelength gravity–capillary waves that are present due to the difference in surface tension and density. In the second case (thin film), radar-backscattered power is mainly diminished through mechanical damping of Bragg-wavelength gravity–capillary waves. The capability of radar imagery to distinguish between varying substances that manifest as a thin film on the sea surface or that mix with seawater near the surface has already been demonstrated in the case of

mineral oil [42] and chemicals [43]. If the thickness of the film on the top of the sea surface is thin compared to the penetration depth δ_p , the EM wave is not altered and will penetrate the film to scatter from the seawater below the film, so the effective dielectric constant will remain that of seawater, and not be changed by different, generally lower, dielectric constants of that product which forms the film. When the film becomes thicker (relative to the penetration depth), the dielectric properties of the film/seawater mixture will be reduced compared to seawater itself, with the mixture acting as a separate layer on the ocean surface with intermediate dielectric values that will also impact the power of the backscattered signal.

Mineral oil films can form multilayers, whose thickness can vary considerably within oil patches, from less than 1 μm to more than 1 mm [44]–[46]. When released at sea, mineral oil mixes quickly with seawater under the action of wind and waves and will result in water-in-oil mixture (emulsion) with water content generally between 50% and 75% [47].

Results shown in Fig. 1 suggest that the backscattered signal from ocean surface covered by a mineral oil film will only be impacted by the dielectric properties of the medium in the case of very thick slick, with greater effect on high-frequency imaging radar. Otherwise, damping of the sea surface roughness will be the primary mechanisms for decreasing radar-backscattered power. Because the dielectric constants of biogenic films and mineral oil are similar [48], [49] and because biogenic films can be observed on the ocean surface only in the form of monolayers [15], [18], i.e., they are only one molecular layer thick (typical thickness of 2.4–2.7 nm), the same phenomena will be observed as in the case of mineral oil film, namely, reduced backscattered power caused by mechanical damping of the Bragg-wavelength surface waves with little dependence on the effective dielectric constant.

III. STATE-OF-THE-ART POLSAR PARAMETERS

Radar remote sensing techniques are of great interest for monitoring slick-covered ocean surface for two primary reasons. First, EM waves are sensitive to the modification of the sea surface induced by oil. Second, SAR sensors can be used any time of day or year and in almost any weather conditions [50]. The physical interaction between an EM wave and a slick-covered area has been established by analyzing airborne and spaceborne data acquired over ocean surfaces covered by mineral oil and biogenic film [18], [51], [52]. Many studies [19]–[26] have analyzed the added value of polarimetric SAR data for slick monitoring. A review of SAR parameters used for this purpose is given in [14], where most of the methods published in the literature for oil slick detection are presented. Since this publication in 2012, many researchers have attempted to assess the utility of POLSAR parameters for slick detection. These works exploit either accidental events [53] or controlled releases of pollutant at sea, the latter of which includes experiments managed by the Norwegian Clean Seas Association for Operating Companies (NOFO) in the North Sea [17], [25], [26], [54]–[57] or the POLLUPROOF experiment whose objective is to establish a procedure for collecting evidence of

illegal maritime pollution by chemicals using remote sensing sensors [43]. In the following, we focus on polarization-dependent parameters that have been found to be efficient for slick detection in the offshore domain [13], [14] and we organize them by input data type. These are separated into categories that use backscattered amplitudes only (incoherent systems) and those that use both amplitude and phase of the backscattered signals (coherent systems, i.e., POLSAR modes of operation), and into systems that acquire dual-polarization data (HH/HV, VV/VH, or HH/VV acquisitions) and those that acquire quad-polarization data (HH/VV/HV/VH). Here we consider only linearly polarized systems, which are currently the most common in remote sensing.

A. Dual-Polarized Synthetic Aperture Radar

1) *Incoherent Dual-Co-Polarized Radar Imaging System:* For slick-detection methods using a dual-co-polarized (HH and VV) radar remote sensing system, the two relevant parameters that use amplitude data only [33] are the Polarization Ratio (PR) and the Polarization Difference (PD), respectively, defined within the Bragg model (in linear units) as

$$\text{PR} = \frac{\sigma_{\text{HH}}^0}{\sigma_{\text{VV}}^0} \approx \frac{\alpha_{\text{HH}}}{\alpha_{\text{VV}}} \quad 0 \leq \text{PR} \leq 1 \quad (9)$$

$$\text{PD} = \sigma_{\text{VV}}^0 - \sigma_{\text{HH}}^0 \quad \text{PD} \geq 0. \quad (10)$$

As backscattered power over the sea surface in the Bragg regime is stronger in VV polarization than that in HH [12], it follows that PR varies between 0 and 1 and PD takes positive values. As reflectivities at VV and HH are always different when the SNR is greater than 0 dB, there is no realistic scenario in which backscattered power is nonzero and PD is equal to 0. It follows from (9) that PR, commonly referred to as the Bragg ratio when written in this simplified form, is independent of sea surface roughness (W) and depends only on the local incidence angle and the relative dielectric constant [41], [42]. Because the relative dielectric constant is lower for slick-covered areas than for uncontaminated seawater [41], the Polarization Ratio (PR) can detect sea surface slicks through the decrease in the relative dielectric constant. It is also considered an effective parameter to distinguish between slick-covered sea surface and oceanographic phenomena [17].

When the ocean surface is covered by a thin film (like biogenic or thin mineral oil film), the surface layer is transparent to the EM waves, and thus the radar will sense the dielectric constant of the seawater under the film, which will have no effect on the Polarization Ratio [58]. However, for thick oil film (relative to the radar wavelength) or emulsions, the dielectric constant of the imaged product will affect the radar backscattering and its effect will manifest itself on the Polarization Ratio. Thus, Polarization Ratio could be used to discriminate between thin film and emulsion/thick film. However, at least one major issue occurs when using the Polarization Ratio for slick characterization at sea. The contrast, which is defined as the ratio of the values obtained over contaminated and uncontaminated areas, is low. This limitation is evident in Fig. 2 where, for example, there is little difference

in PR between pure seawater (line labeled 100%) and a 50–50 or a 25–75 mixture of seawater and oil.

The PD parameter is of interest for slick detection at sea [17], [33], [43] because it is proportional to the spectral density of the ocean surface roughness [59], which is altered even by thin films [9], [10]. As discussed in [33], the non-polarized part of the backscattered signal (see Section II) is removed using PD. Therefore, the Polarization Difference mostly contains contributions due to the presence of short wind-driven waves around the Bragg wavenumber (2), making PD an attractive parameter for slick detection at sea [33], [43].

2) Coherent Dual-Co-Polarized Radar Imaging System:

The Polarization Difference (PD) and the Polarization Ratio (PR), introduced above, use only the backscattered power of the complex dual-polarized signals. With a remote sensing system collecting coherent acquisitions, the phase between the two co-polarized channels is measured. In this case, the following parameters are generally recommended in the literature for slick detection over the ocean surface: the modulus of the co-polarized complex coherence (ρ_{HHVV}) [22], [25] and the Bragg likelihood ratio (BLR) [25], [26]

$$\rho = \frac{\langle S_{HH} S_{VV}^* \rangle}{\sqrt{\langle |S_{HH}|^2 \rangle \cdot \langle |S_{VV}|^2 \rangle}} = \rho_{HHVV} e^{j\Delta\phi} \quad 0 \leq \rho_{HHVV} \leq 1 \quad (11)$$

$$\text{BLR} = \max\{0, \text{Re}(\rho)\} \quad 0 \leq \text{BLR} \leq 1. \quad (12)$$

In (11) and (12), superscript * denotes the complex conjugate, $\langle \cdot \rangle$ denotes spatial averaging, $\text{Re}(\cdot)$ denotes the real part of a complex number, and S_{pp} represents the complex scattering coefficient. In the case of an EM signal backscattered by rough surface, the co-polarized channels (HH and VV) are correlated and in phase [12], [60]. It follows that the complex correlation of the co-polarized channels is a real number (imaginary part close to 0) and the modulus (ρ_{HHVV}) takes values close to 1. Thus, these two parameters have the same behavior, namely, the value is high (close to 1) when the Bragg scattering mechanism is dominant and the value is low (close to 0) otherwise. However, when the backscattered signal is corrupted by noise, the phase between the co-polar channels becomes uniformly distributed between 0 and π and the modulus of the co-polarized coherence reaches 0. The polarimetric coherence between the co-polarized channels can be written as the product of three terms

$$\rho_{HHVV} = \rho_{\text{Scattering}} \rho_{\text{Temp}} \rho_{\text{SNR}} \quad (13)$$

where $\rho_{\text{Scattering}}$ denotes the correlation between HH and VV due to scattering mechanism (close to 1 over ocean surface) and ρ_{Temp} and ρ_{SNR} denote temporal decorrelation and decorrelation due to noise, respectively. The decorrelation time of a moving sea surface is of the order of 1×10^{-2} s at X-band [61] and 1×10^{-1} s at L-band [62]. For sensors operating at low pulse repetition interval (PRI), the decorrelation due to time lag between transmitted pulses (alternatively polarized H and V) can be neglected. For the two sensors investigated in Sections IV-A and IV-B, the PRIs are equal to 1×10^{-7} s for SETHI and 2.3×10^{-6} s for UAVSAR, which

are both orders of magnitude smaller than the surface decorrelation time and assure no temporal decorrelation between HH and VV (ρ_{Temp} close to 1). Thus, the only remaining decorrelation term is that induced by the noise defined as

$$\rho_{\text{SNR}} = \frac{1}{1 + \text{SNR}^{-1}}. \quad (14)$$

Equation (14) exhibits the strong dependence of the modulus of the co-polarized complex coherence (ρ_{HHVV}), as well as the BLR, on the SNR. Following (14), an SNR equal to 10 or 5 dB induces a decorrelation between the two co-polarized channels of 10% and 25%, respectively.

In addition to their strong dependence on the SNR, being normalized by the amplitude of the co-polarized backscattering coefficient, both ρ_{HHVV} and BLR are more strongly affected by the noise (low SNR) than the intensities alone. To overcome this limitation while exploiting the potential of these parameters, we propose in this paper to use the Hermitian product (HP) between the two co-polarized channels, defined as

$$\text{HP} = \langle S_{HH} S_{VV}^* \rangle. \quad (15)$$

3) Coherent Dual-Polarized Radar Imaging System: A way to represent polarimetric information collected by a coherent dual-polarized (HH and HV or VV and VH) remote sensing system is the Stokes formalism [63]–[65]. The Stokes parameters are a set of four values (S_0 , S_1 , S_2 , and S_3) describing the polarization state of an EM wave

$$S_0 = \langle |E_H|^2 + |E_V|^2 \rangle \quad (16)$$

$$S_1 = \langle |E_H|^2 - |E_V|^2 \rangle \quad (17)$$

$$S_2 = 2\text{Re}(\langle E_H E_V^* \rangle) \quad (18)$$

$$S_3 = 2\text{Im}(\langle E_H E_V^* \rangle) \quad (19)$$

where $\text{Re}(\cdot)$ and $\text{Im}(\cdot)$ select the real and the imaginary values, respectively, of a complex number. E is the measured complex scattering coefficient in the subscripted polarization and is independent of the polarization state of the transmitted wave. Using this formalism, Touzi *et al.* [19], Shirvany *et al.* [23], and Nunziata *et al.* [24] have proposed to use the degree of polarization (DoP) for ship or marine pollution detection

$$\text{DoP} = \frac{\sqrt{S_1^2 + S_2^2 + S_3^2}}{S_0} \quad 0 \leq \text{DoP} \leq 1. \quad (20)$$

Over ocean surface, the EM wave is well polarized [60] and the DoP is close to 1 [23]. When the received signal is dominated by the noise, as in the case for slicked surfaces imaged by most of spaceborne SARs available today, the measured signals appear depolarized and the DoP reaches values close to 0.

These last four parameters (ρ_{HHVV} , BLR, HP, and DoP), derived from co-polarized coherent acquisitions, are recommended in the literature for oil slick detection and the proposed justification comes from their ability to distinguish Bragg scattering (over clean sea surface) to another scattering mechanism that may occur over slick-covered area [19], [22]–[25]. However, the impact of the noise on these parameters is often omitted even though, as we have just seen, it can have a predominant effect. An analysis of the impact of the noise is presented in Section V-D.

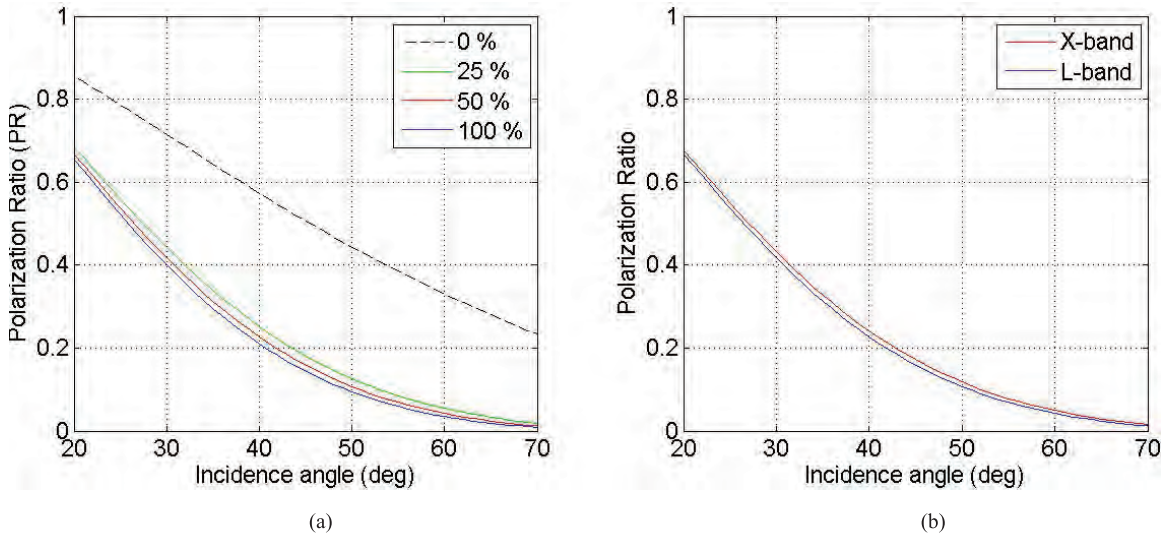


Fig. 2. PR (Bragg theory) as a function of incidence angle (a) at L-band for a water content of 0% (black dashed line), 25% (green line), 50% (red line), and 100% (blue line) and (b) at X-band (red line) and L-band (blue line) for a water content of 50%. A linear mixing is assumed between mineral oil and seawater. Values of dielectric constants are from Table I.

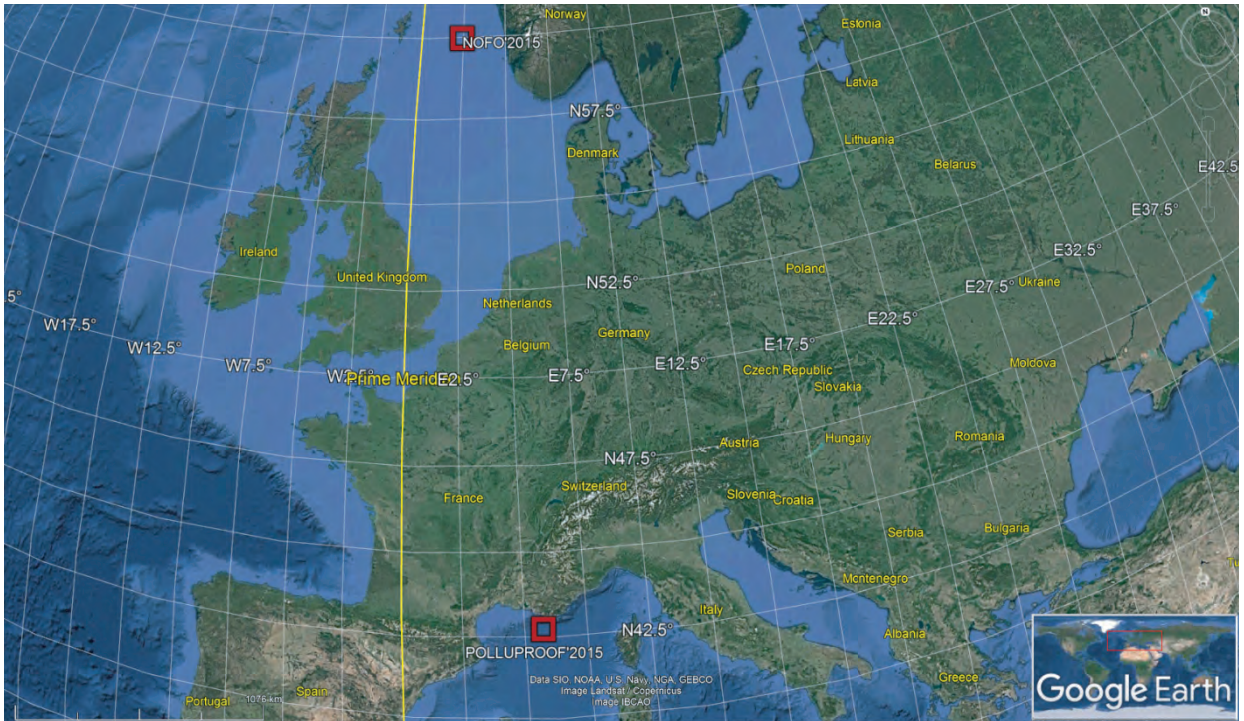


Fig. 3. Map of the POLLUPROOF*2015 and NOFO*2015 experimental sites.

B. Coherent Quad-Polarized Synthetic Aperture Radar

Many methods using quad-polarized remote sensing data are proposed in the literature to detect ocean surface covered by a slick. For a review, the reader is referred to [13] and [14]. Here we consider a few parameters dependent on all polarizations, namely, the Conformity Coefficient (μ) [66], originally proposed in [67] for remote sensing application over land surfaces, the first eigenvalue (λ_1) [41], and the Entropy (H) [25], [66] based on the eigenvalue decomposition of the covariance matrix C [68], [69]

$$\mu \approx \frac{2(\text{Re}(S_{HH}S_{VV}^*) - |S_{HV}|^2)}{|S_{HH}|^2 + 2|S_{HV}|^2 + |S_{VV}|^2} \quad -1 \leq \mu \leq 1 \quad (21)$$

$$C = \begin{bmatrix} \langle |S_{HH}|^2 \rangle & \sqrt{2} \langle S_{HH}S_{HV}^* \rangle & \langle S_{HH}S_{VV}^* \rangle \\ \sqrt{2} \langle S_{HV}S_{HH}^* \rangle & 2 \langle |S_{HV}|^2 \rangle & \sqrt{2} \langle S_{HV}S_{VV}^* \rangle \\ \langle S_{VV}S_{HH}^* \rangle & \sqrt{2} \langle S_{VV}S_{HV}^* \rangle & \langle |S_{VV}|^2 \rangle \end{bmatrix}. \quad (22)$$

Over the ocean, because the cross-polarized signal is very low, the Conformity Coefficient can be interpreted in the same way as the co-polarized coherence (11) or the BLR (12). A simple algorithm with a threshold equal to 0 is proposed in [66] for oil slick detection. The Entropy has similar interpretation to that of the Degree of Polarization (DoP), but with values near 0 corresponding to one dominant scattering mechanism and values close to 1 when multiscattering occurs or when the signal is corrupted by noise [68], [69].

TABLE II
ENVIRONMENTAL CONDITIONS AND PROPERTIES OF RELEASED SUBSTANCES

Date of release	Time of release (UTC)	Amount of release	Released substance	Time of imaging (UTC)	Wind speed (m/s)	Wind direction (from-deg)	Wave height (m) at time of imaging
22 May, 2015	15:00-15:30	1 m ³	Rapeseed oil	16:07	7	315	2
22 May, 2015	15:25-15:40	1 m ³	FAME	16:07	7	315	2
09 June, 2015	06:30-08:00	45 m ³	Mineral oil	09:56 10:01	5	255	1

TABLE III
PROPERTIES OF SAR SCENES INVESTIGATED IN THIS PAPER. INCIDENCE ANGLE AND NESZ VALUES ARE THE MINIMUM AND MAXIMUM ACROSS THE IMAGING SWATH

Sensor	Frequency band	Polarization mode	Experiment	Date	Time (UTC)	Incidence angle (deg)	NESZ (dBm ² /m ²)
SETHI	L	Quad-Pol	POLLUPROOF	22 May, 2015	16:07	34 / 52	-51 / -53
SETHI	L	Quad-Pol	NOFO	09 June, 2015	10:01	34 / 52	-51 / -53
UAVSAR	L	Quad-Pol	NOFO	09 June, 2015	09:56	19 / 68	-35 / -51

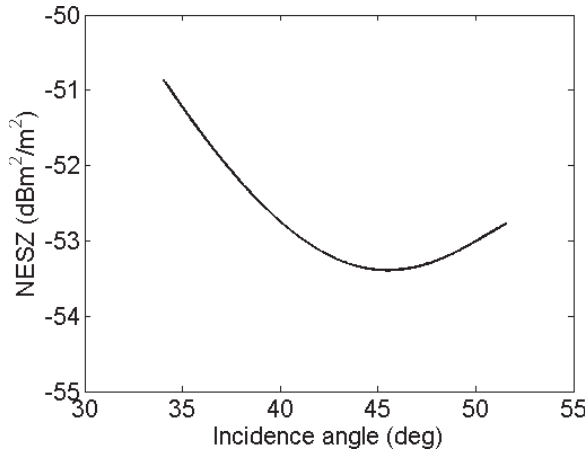


Fig. 4. SETHI—POLLUPROOF’2015 and NOFO’2015 experiments—instrument noise floor (NESZ) plotted by increasing incidence angle.

The main issue when working with quad-polarized SAR data is the low power of the backscattered signal in the cross-polarization channels (HV and VH). For most of spaceborne SAR sensors available today, the backscattered signal measured in cross-polarization over slick-covered area is close to or below the instrument noise floor [17]. This low SNR values strongly impact the values of the polarimetric parameters measured over oil slicks.

IV. EXPERIMENTAL DATA

Two experimental campaigns of measurements are used in this paper: NOFO’2015 and POLLUPROOF’2015 (see Fig. 3). POLLUPROOF’2015 was conducted in May 2015 over the

Mediterranean Sea (off the French coast, near 42°45’ N, 5°45’ E) and focused on the release and subsequent observation of several hazardous and noxious substances (HNS) that are meant to represent the majority of chemicals commonly transported by sea. The primary goal of this experiment is to establish a procedure for collecting evidence of illegal marine pollution by HNS using airborne sensors [43]. SAR images of controlled releases of fatty acid methyl esters (FAME) and rapeseed oil, conducted during the POLLUPROOF’2015 experiment, are investigated in this paper (Table II). Vegetable oils (like plant oil or rapeseed oil) have already been imaged by SAR sensors as they are often used to simulate a natural monomolecular biogenic slick [15], [18], [25]. NOFO’2015 was conducted from June 8, 2015 to June 14, 2015, during NOFO’s oil-on-water exercise. This experiment aims at testing recovering systems of pollution at sea by hydrocarbons. During the exercise, airborne and spaceborne acquisitions were collected over the offshore spill areas (North Sea, near 59°59’ N, 2°27’ E—see Fig. 3 and [56, Fig. 2]). In the following, we use SAR images collected by the French and American airborne sensors on June 9, 2015. For the investigated experiment, the released product is an emulsion of mineral oil in water, with a water content of 60% (Table II). It consists of a mixture of seawater, Oseberg crude oil, and a small addition of intermediate fuel oil (IFO) 380 (IFO or marine diesel oil, with a viscosity of 380 mm²·s⁻¹). For the trial, 45 m³ of mineral oil emulsion was discharged at sea. Large swath remote sensing data collected by UAVSAR (see Section IV-B) imaged the full extent of the hydrocarbon-covered area, namely, 5.4 km². Assuming all the 45 m³ of mineral oil emulsion released at sea was on

TABLE IV
SIGNAL-TO-NOISE RATIO—SETHI, NOFO'2015 EXPERIMENT, JUNE 09, 2015, 10:01 UTC

Region	Incidence angle (deg)	HH	HV	VV
		MEAN [MIN MAX] dB	MEAN [MIN MAX] dB	MEAN [MIN MAX] dB
Clean sea	44.5°	26.5 [25.8 27.4] dB	16.4 [15.6 17.2] dB	34.1 [33.3 34.9] dB
Oil slick	44.5°	21.5 [19.7 23.0] dB	10.2 [8.6 12.3] dB	28.0 [26.3 29.3] dB

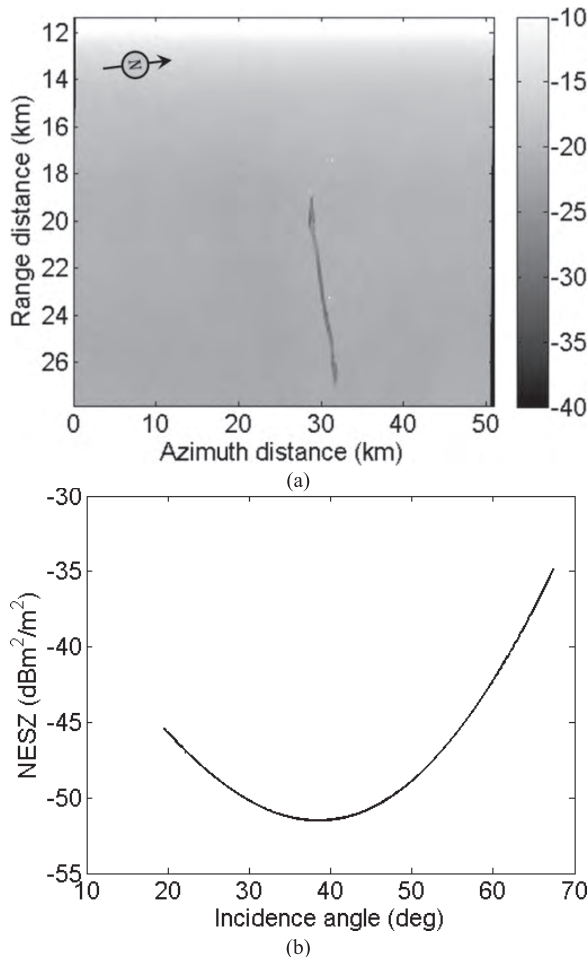


Fig. 5. UAVSAR—NOFO'2015 experiment, June 09, 2015, 09:56 UTC. (a) VV image and (b) instrument noise floor (NESZ) plotted by increasing incidence angle for the corresponding acquisition. The oil slick is located across the range of incidence angles from $\sim 56^\circ$ to 67° in the image.

the surface, the upper limit of the average slick thickness is greater than $1 \mu\text{m}$. The actual thickness is likely to be lower, shown through modeling of slicks released in the same area on June 10 during another spill experiment and under higher wind conditions that indicate only $\sim 50\%$ of the released oil was on the surface a few hours after the release [70].

Wind and waves information was obtained from Météo-France, the French national meteorological service (POLLUPROOF'2015 campaign), and from the Norwegian Meteorological Institute (NOFO'2015 campaign) and is given in Table II.

The methodologies and the results presented in the following are based on SAR data collected by SETHI [27], the remote sensing imaging system developed by ONERA,

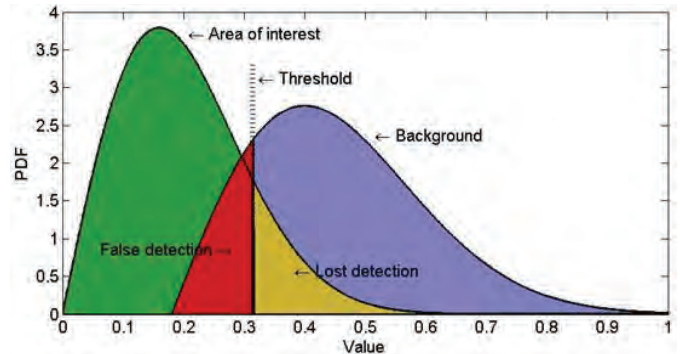


Fig. 6. Overview of histogram thresholding for ROC curve computation based upon separation of two classes.

as well as experimental data acquired by UAVSAR [28], the airborne sensor of JPL/NASA. Sections IV-A and IV-B briefly present the two SAR systems used here. Table III summarizes all SAR scenes investigated in this paper.

A. SETHI: Airborne Quad-Polarized SAR Sensor

SETHI is the ONERA airborne remote sensing laboratory designed to explore the science applications of remote sensing [27]. It is a pod-based system operating onboard a Falcon 20 Dassault aircraft flying at an altitude of 9000 ft. For both POLLUPROOF'2015 and NOFO'2015 campaigns, POLSAR data were acquired by SETHI at L-band, with a range resolution of 1 m (bandwidth from 1.25 to 1.4 GHz). Images are processed with an azimuth (along track) resolution equal to the range resolution. Imaged area is 9.5 km in azimuth and 1.5 km in range, with incidence angles from 34° to 52° . The instrument noise floor has been estimated using the method proposed in [71], and the results are shown in Fig. 4. The estimated noise equivalent sigma zero (NESZ) is very low, ranging from around -51 to $-53 \text{ dBm}^2/\text{m}^2$, allowing a sufficiently high SNR over slick-covered areas for valid analysis of surface characteristics. Examples of high-resolution polarization-dependent images acquired by SETHI at L-band are shown in Section V.

B. UAVSAR: Airborne Quad-Polarized SAR Sensor

During the NOFO'2015 experiment, UAVSAR (developed by NASA [28]) acquired POLSAR data at L-band over controlled releases of mineral oil at sea, flying at an altitude of 35100 ft. The data used in this analysis were acquired on June 9, 2015, within 5 min of SETHI and over the same area. They are processed with a resolution of 5 m in range and 7.2 m in azimuth (multilook format). The incidence angle ranges from 19.5° to 67.5° across the swath. The instrument

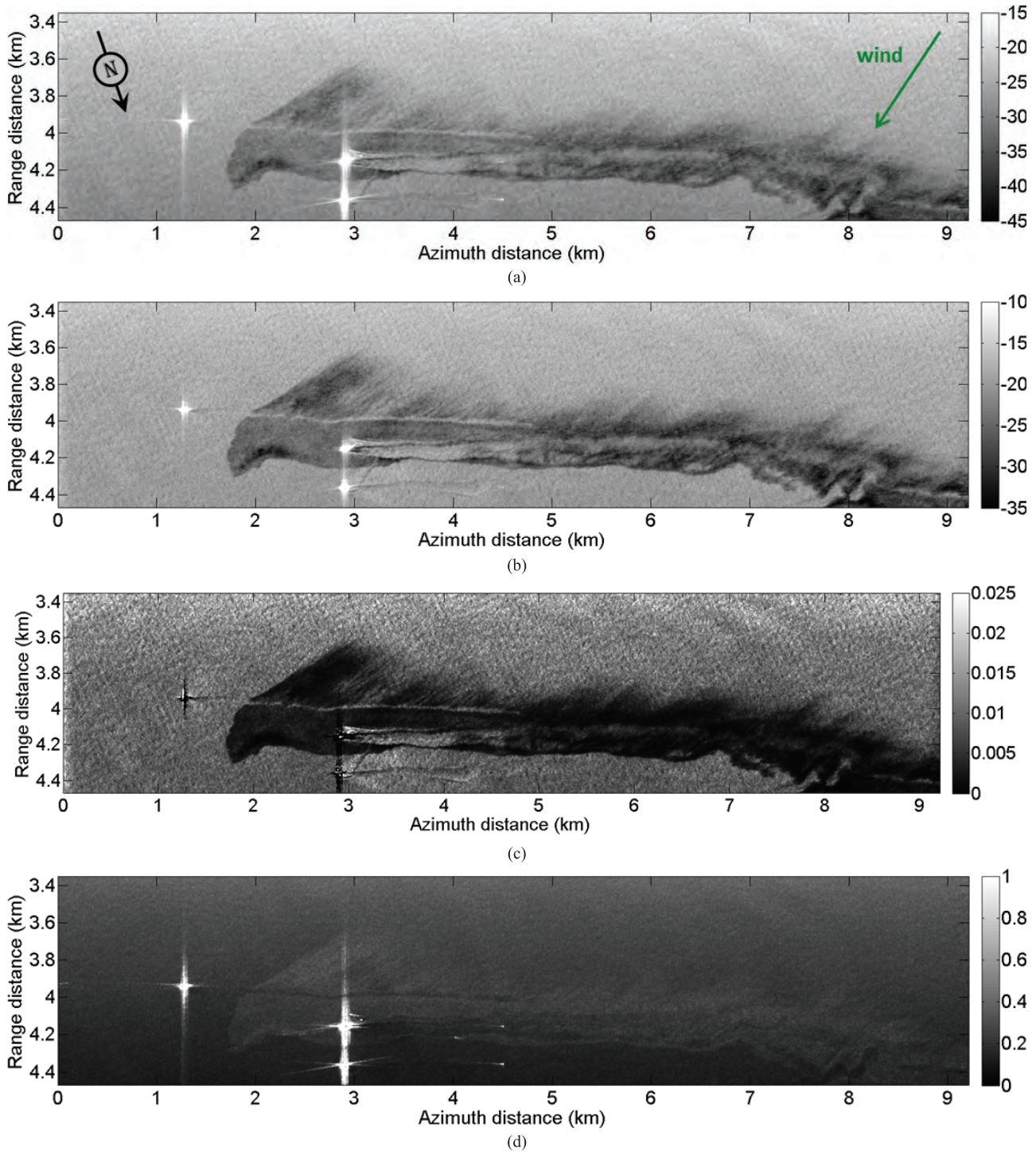


Fig. 7. SETHI NOFO'2015—L-band SAR data acquired over mineral oil released at sea—June 09, 2015, 10:01 UTC. (a) HH, (b) VV, (c) PD, and (d) PR quantities. Multilook $7 \text{ m} \times 7 \text{ m}$.

noise floor has been estimated using the same methodology as that used for the SETHI one [71], and it is shown in Fig. 5. The NESZ is very low, ranging from around -35 to $-51 \text{ dBm}^2/\text{m}^2$, allowing a sufficient SNR over sea surface covered by slicks for valid analysis of surface properties.

V. METHODOLOGY AND PERFORMANCE ASSESSMENT

We use receiver operating characteristic (ROC) [72] curves to characterize the detection capabilities of the

parameters discussed in Section III. This is an extension of the methodology published in [26] using a much larger data set and a more comprehensive set of parameters. ROC curves are obtained by plotting the probability of detection (Pd) against the probability of false alarm (Pfa), which quantifies the performance of a detector as its discrimination threshold is varied. In other words, ROC graphs depict the tradeoff between hit rates and false alarm rates of detectors [72]. The procedure, shown in Fig. 6, is as follows: we manually select areas of

clean sea surface (i.e., the background) and slick (i.e., the area of interest) and compute for each investigated parameter the histograms of values within the two regions. Then, for all possible values of the detection threshold, we calculate Pd as the fraction of samples within the area of interest that are below the threshold and Pfa as the fraction of samples in the background that are below the threshold. We will use these results to develop an instrument-independent ranking of the detection capabilities of each investigated parameter.

A. Sea Surface Slick Observation

We begin by evaluating the quad-pol SAR data acquired by SETHI (Fig. 7) over a controlled release of mineral oil (NOFO'2015 experiment). In Fig. 7, images of HH and VV channels are given as well as the PD and the PR maps. Visually, there is no significant difference between the cross-polarized and the co-polarized images, so the HV channel is not shown here. For these images, the wind direction is from the top right (see green arrow in Fig. 7(a); black arrow indicates the north direction). Wind information was obtained from the Norwegian Meteorological Institute and is given in Table II. The oil slick is observable as a dark area, with a ship's wake running through the slick. Within the lower part of the slick, the passage of a mechanical recovery boom (MOS sweeper [73]) appears to have left a relatively clean sea surface. Images show a feathered structure along the top of the slick (upwind) and a smooth edge on the downwind side of the slick, the expected appearance of the slick based on the wind direction.

Interestingly, while the upper limit of the slick thickness (greater than $1 \mu\text{m}$) has been estimated to be at least one-hundredth of the penetration depth at L-band (typically of the order of millimeters for water content greater than 50%—see Fig. 1), the mineral oil slick is observable in the PR images [Fig. 7(d)]. An explanation could be that there is a dielectric change due to the presence of oil in the water column that will impact the Polarization Ratio.

Low backscattering values from slick-covered areas can lead to low SNR values. Therefore, it is critical that we ensure sufficiently high SNR values before undertaking any analysis. SNR values along a transect through data obtained by SETHI during the NOFO'2015 experiment are shown in Fig. 8. The curves have been computed across a range transect at azimuth 2.1 km. The slick is between 3.85 km (incidence angle 44.2°) and 4.2 km (incidence angle 49.4°). The SNR values are high (even in cross-polarization), which enables polarimetric analysis of the surface properties.

B. Evaluation of Polarimetric Parameters for Slick Detection: Mineral Oil

We first focus on SAR data collected by SETHI over mineral oil spill (NOFO'2015 experiments). Fig. 9 shows areas selected for ROC curves computation where the uncontaminated sea surface (background) is outlined by the blue box and the contaminated area of interest is outlined by the red box. Note that the average SNR computed over the two regions (Table IV) is greater than 10 dB.

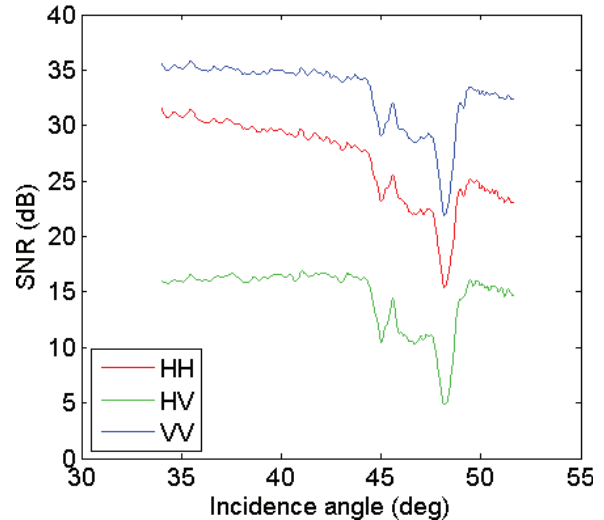


Fig. 8. SETHI signal-to-noise ratio (SNR) in polarization HH (red), HV (green), VV (blue)—range transect for azimuth 2.1 km (see Fig. 7)—June 09, 2015, 10:01 UTC.

ROC curves (Fig. 10) show that the Polarization Difference and VV are the most efficient parameters for mineral oil slick detection (i.e., for a given value of Pfa, they exhibit the greater value of Pd). The first eigenvalue (λ_1) is also very efficient for detecting slick-covered area, as it gives a performance of detection similar (slightly lower for low values of Pfa) to that obtained with VV and PD. They are then followed by the Hermitian Product between HH and VV (HP) and HH and HV. HV has good performance of detection and is even better than that of HH for low values of Pfa. This result for HV, which is consistent with the results obtained with UAVSAR data in stronger wind conditions obtained one day later (June 10) [57], is possible because of high SNR over the entire image. Then, we found that the Polarization Ratio and the studied quad-polarimetric parameters have low Pd values for all Pfa values. So, the co-pol coherence, the Bragg Likelihood Ratio, the Degree of Polarization, the Entropy, and the Conformity Coefficient are the parameters that give the worst performances of detection. These results seem to indicate that the same main scattering mechanism occurs over both contaminated and uncontaminated sea surface, namely, surface reflection and Bragg scattering [41]. To confirm this, we note that the polarimetric entropy, computed with a high SNR even over the polluted area, is low over both the clean sea surface and the slick; the mean entropy values are, respectively, equal to 0.18 and 0.17. This indicates that only one dominant scattering mechanism occurs, which confirms previous observations [56], [57] for the NOFO'2015 exercise and the original observation based on UAVSAR L-band data acquired over the Deepwater Horizon oil spill accident [41].

We now investigate SAR data collected with UAVSAR during the same NOFO'2015 experiment (mineral oil). As for SETHI, the UAVSAR instrument is characterized by a very low noise floor, which suggests a good complementarity of the results obtained with the two airborne sensors. The imaged ocean surface is the same as for the previous SETHI analysis (Fig. 9), and the time lag between the two

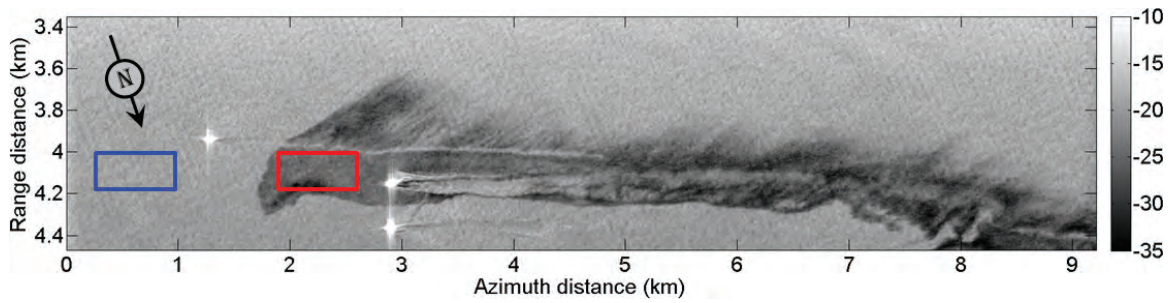


Fig. 9. Areas selected for ROC curve computation—blue box: clean sea surface and red box: slick area. SETHI, NOFO’2015 experiment, June 09, 2015, 10:01 UTC; VV channel; multilook 7 m × 7 m.

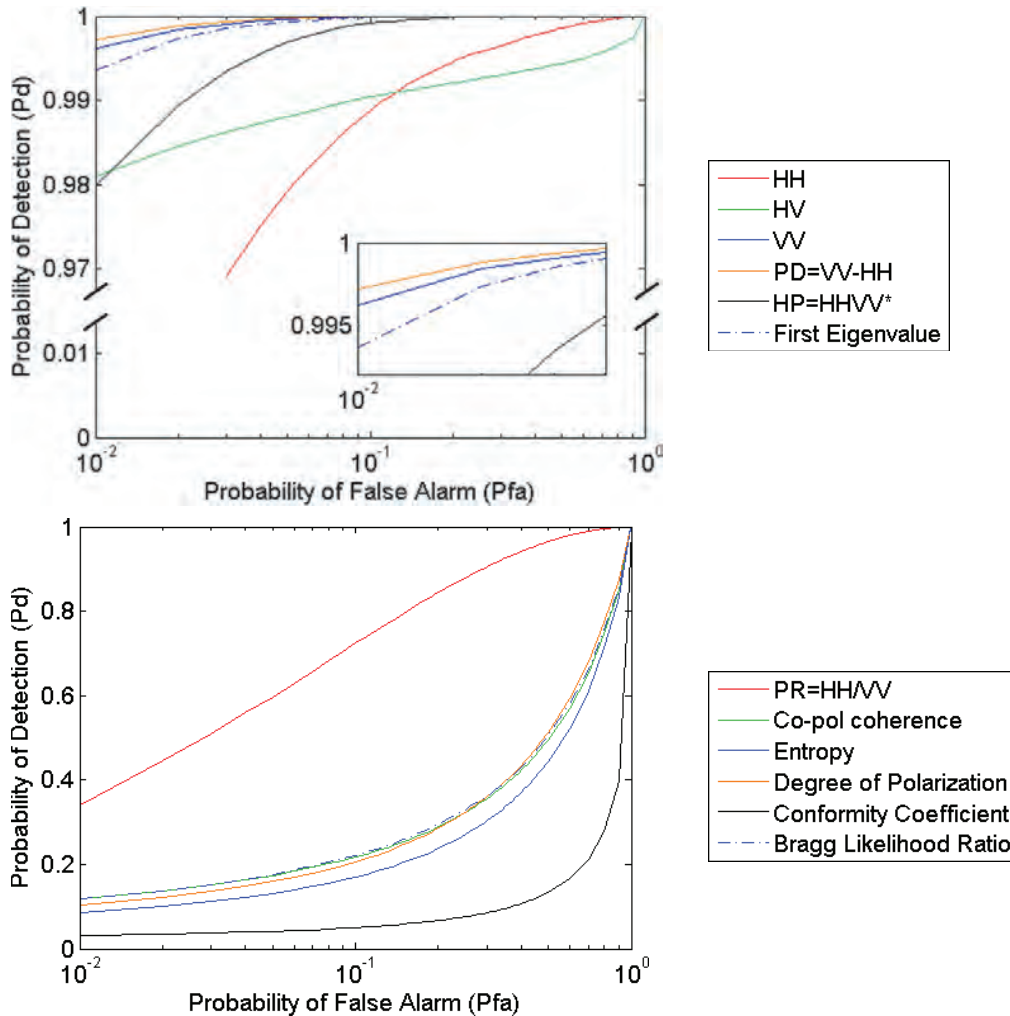


Fig. 10. SETHI, NOFO’2015 experiment, June 09, 2015, 10:01 UTC—Pd versus Pfa computed for all investigated parameters. Note the cut of the vertical axis on the top figure.

TABLE V
SIGNAL-TO-NOISE RATIO—UAVSAR, NOFO’2015 EXPERIMENT, JUNE 09, 2015, 09:56 UTC

Region	Incidence angle (deg)	HH	HV	VV
		MEAN [MIN MAX] dB	MEAN [MIN MAX] dB	MEAN [MIN MAX] dB
Clean sea	56.8°	14.8 [14.4 15.1] dB	9.4 [9.1 9.6] dB	23.7 [23.3 24.0] dB
Oil slick	56.8°	10.2 [10.0 10.4] dB	4.8 [4.5 5.0] dB	17.0 [16.7 17.4] dB

acquisitions is 5 min. For UAVSAR ROC graph analysis, the contaminated sea surface is close to that selected for SETHI (Figs. 9 and 11). Clean sea regions are selected to be at

the same range as the selected oil-covered areas, but they are in different places for SETHI and UAVSAR due to different flight directions. For the chosen regions of interest, the NESZ is

TABLE VI
SIGNAL-TO-NOISE RATIO—SETHI, POLLUPROOF'2015 EXPERIMENT, MAY 22, 2015, 16:07 UTC

Region	Incidence angle (deg)	HH	HV	VV
		MEAN [MIN MAX] dB	MEAN [MIN MAX] dB	MEAN [MIN MAX] dB
Clean sea	42.5°	30.7 [29.6 31.7] dB	18.7 [17.5 19.7] dB	36.6 [35.6 37.5] dB
Oil slick	42.5°	26.7 [25.9 27.5] dB	14.6 [13.5 15.8] dB	33.1 [32.2 33.8] dB

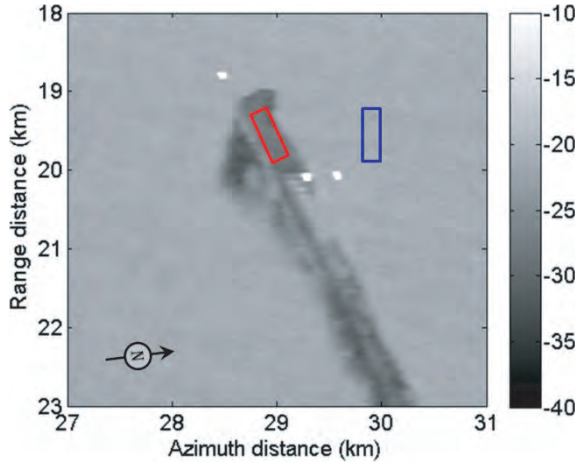


Fig. 11. Areas selected for ROC curve computation. Blue box: clean sea surface and red box: slick area. UAVSAR, NOFO'2015 experiment, June 09, 2015, 09:56 UTC—VV channel.

around $-45 \text{ dBm}^2/\text{m}^2$ (incidence angle around 57°). The SNR in the selected regions are given in Table V. As for SETHI, the levels are high ($>5 \text{ dB}$), which ensures a reliable analysis of surface backscatter over both slick-free and oil-covered sea surfaces. ROC graphs shown in Fig. 12 demonstrate that the best performance of detection is given by the cross-polarized channel (HV), followed by VV, the Polarization Difference, and the first eigenvalue (λ_1), then HH and the Hermitian Product between HH and VV (HP), and finally the conventional quad-polarimetric parameters of Entropy, Polarization Ratio, Degree of Polarization, dual-pol coherence, Bragg Likelihood Ratio and Conformity Coefficient. These results are very close to those obtained by SETHI.

C. Evaluation of Polarimetric Parameters for Slick Detection: Vegetable Oil

We now investigate Fatty Acid Methyl Esters (FAME) and rapeseed oil releases imaged by SETHI during the POLLUPROOF'2015 experiment (Fig. 13). Because of their physicochemical properties, these two substances have different behaviors once released into the ocean. FAME forms a cloud in the water column composed of microdroplets, and rapeseed oil forms a film on the surface [43]. These two behaviors have been highlighted in [43], using the oil–water mixing index introduced in [42].

The slick contains both substances. FAME appears on the left part of the spill and covers a surface of 0.29 km^2 [see red box in Fig. 13(a)]. Rapeseed oil corresponds to the right part of the spill [green box in Fig. 13(a)] and covers a surface of 1.26 km^2 . In between, there is a mixture of the two products [blue box in Fig. 13(a)]. From the amount

released product (1 m^3) and the area covered by the spill, the average thickness of the rapeseed oil spill is estimated to be equal to $0.8 \mu\text{m}$. This is approximately three orders of magnitude thinner than the penetration depth at L-band. Thus, the relative dielectric constant measured by the radar should be unaffected by the oil slick, and no signature of the rapeseed oil is observed in the Polarization Ratio image [Fig. 13(d)]. FAME, which mixes in the seawater column [43], slightly appears on the Polarization Ratio image, probably due to a decrease of the effective dielectric constant of this mixture compared to that of the surrounding clean sea area.

Clean sea surface and surface covered by rapeseed oil have been chosen and ROC curves computed for the selected areas. As for mineral oil analysis, the SNR is high (see Table VI), at least 14 dB , over both covered and free sea surfaces.

Similar to the results from mineral oil slicks, we observe (see Fig. 14) that for the rapeseed oil release, most of quad-polarimetric parameters (BLR, Entropy, and co-polarized coherence) give very poor performance of detection while amplitude channels are very powerful: HV gives the best performance of detection, followed closely by VV, the first eigenvalue (λ_1), HH, the Hermitian Product between HH and VV (HP), and the Polarization Difference (PD). As obtained above for mineral oil, we find here again that the Polarization Ratio (PR) and the conventional quad-polarimetric parameters (co-pol coherence, Bragg Likelihood Ratio, Degree of Polarization, Entropy and Conformity Coefficient) give the worst detection performance. We note finally that an identical ordering of the investigated parameters is obtained when selected sea surface contaminated by FAME instead of rapeseed oil (ROC curves not shown here).

This analysis, based on ROC graphs obtained with SAR data acquired by two airborne remote sensing sensors, both characterized by a very low instrument noise floor, demonstrate that, in the three cases shown, the VV and HV amplitude channels provide the best overall performance of detection. Sometimes, a slight improvement could be obtained with polarization-dependent parameters like the Polarization Difference.

Speckle affects the performances of detection, and multi-looking is the most common method to reduce its effect. In this paper, we study the performances of detection offered by several polarization-dependent parameters, all calculated with the same window size, namely, multilooking by 7×7 in range and azimuth directions. The size of the window influences the detection performance of each of the parameters, but since the same window size is always used, the result obtained herein can be generalized to other window sizes.

When SAR data are collected with a very low NESZ, the backscattered signal is not corrupted by noise, the EM wave is well polarized, and only one scattering mechanism

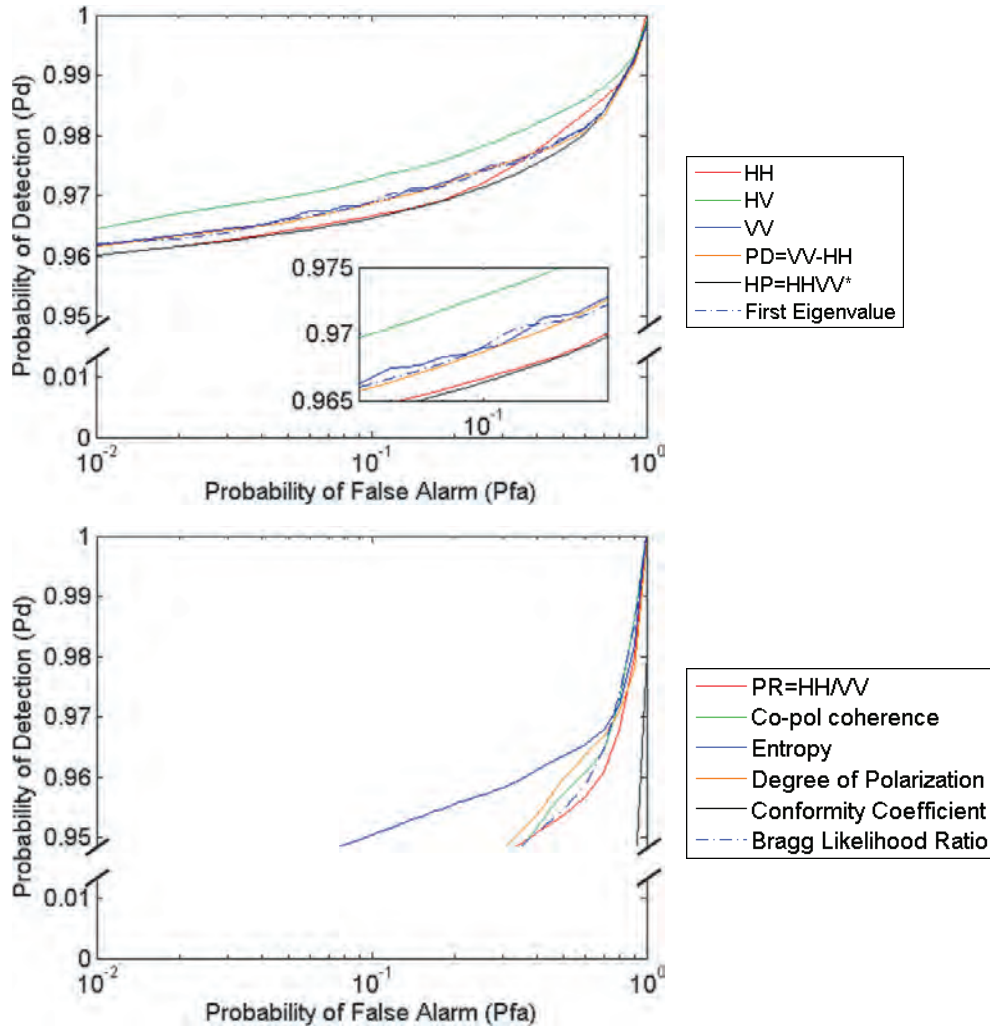


Fig. 12. UAVSAR, NOFO'2015 experiment, June 09, 2015, 09:56 UTC—Pd versus Pfa computed for all investigated parameters. Note the cut of the vertical axis on both figures.

occurs over both clean and contaminated sea surface (low entropy values over both surfaces). When the SNR over slick-covered area is not as high as with the airborne acquisitions analyzed here, as for the spaceborne SARs available today, the instrument noise must be considered when evaluating the performance of detection of polarimetric parameters. Section V-D focuses on the influence of instrument noise.

D. Instrument Noise Effect

To study how the NESZ impacts the ROC curves obtained for the investigated features, we added increasing levels of Gaussian white noise, from 5 to 30 dB, to the raw SAR data collected by SETHI during the NOFO'2015 experiment. We then processed the noisier data using the standard processing software (Fig. 15). We note that when the noise is increased by 15 dB [Fig. 15(d)], its detrimental effect in the VV image is apparent. When 30 dB of noise is added, the slick is no longer observable in the VV image [Fig. 15(f)].

We now assess the detection performance for all simulated instrument noise levels. ROC curves are computed over the areas shown in Fig. 9. The results for some selected

radar quantities are given in Fig. 16, and conclusions are as follows.

- 1) For a given Pfa, Pd for HH, VV, and HV decreases as SNR decreases. When the additive noise is less than or equal to 10 dB, the ROC curves are largely unchanged.
- 2) For a given Pfa, Pd increases for the polarimetric parameters for additive noise values less than 20 dB. Then, performance of detection decreases with greater levels of additive noise.

Thus, in contrast to the amplitude values, the Pd for the polarimetric parameters increases with the instrument noise so long as the SNR is sufficiently high over clean sea surface (~ 15 dB added noise) and then decreases for decreasing SNR. As the SNR decreases, the received signal is increasingly corrupted by noise and the combined noise plus scattered EM signal becomes randomly polarized (DoP goes to 0 and Entropy goes to 1 as the total signal approaches noise only). With sufficiently high noise levels, both contaminated and uncontaminated sea surfaces will appear randomly polarized and no further separation between the two regions is possible. SNR values as well as mean values of DoP and Entropy over

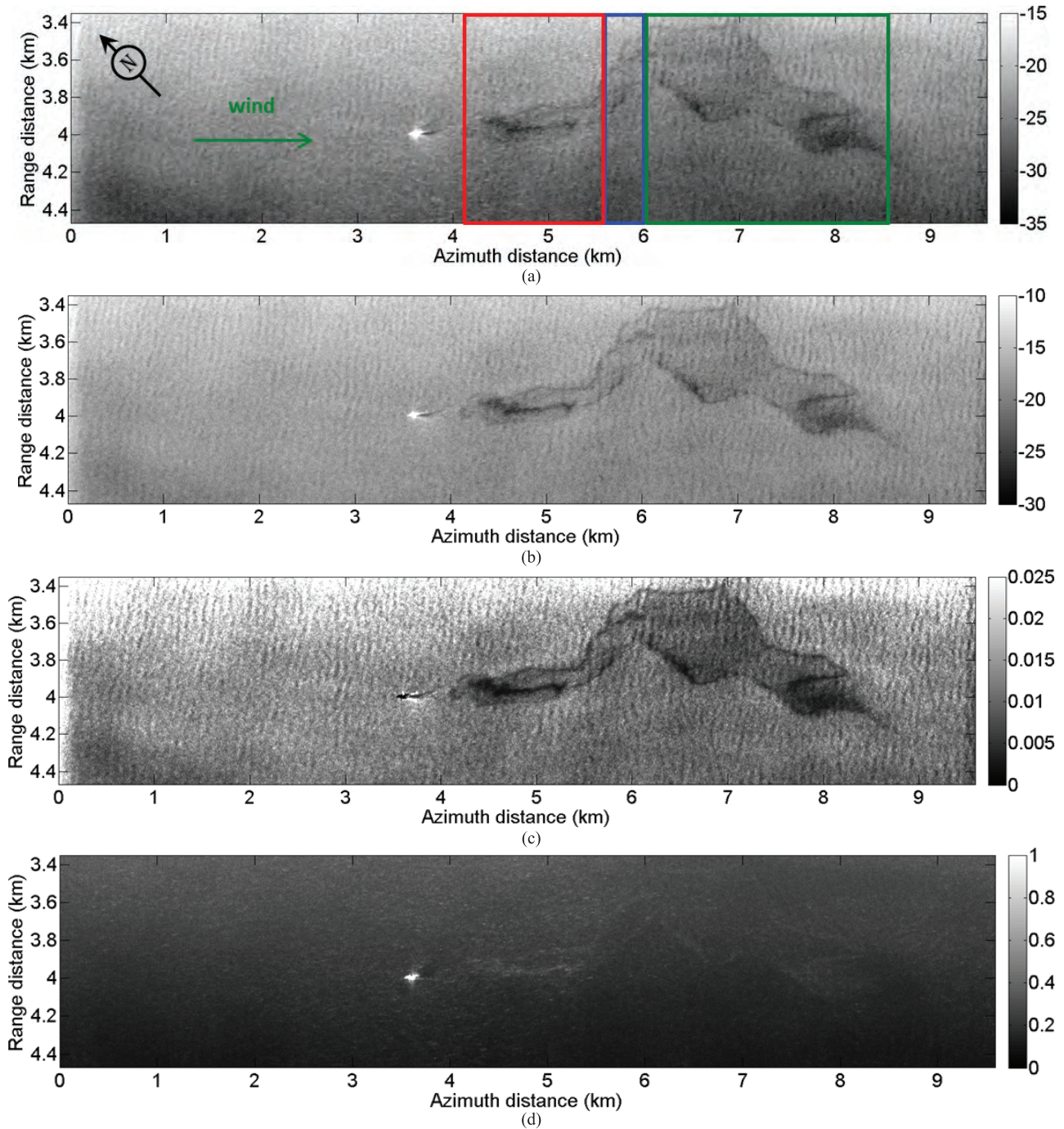


Fig. 13. SETHI POLLUPROOF*2015—L-band SAR data—May 22, 2015, 16:07 UTC. (a) HH, (b) VV, (c) PD, and (d) PR quantities—multilook $7 \text{ m} \times 7 \text{ m}$. FAME is indicated by the red box and rapeseed oil by the green box, and the blue box corresponds to a mixture between the two products.

clean sea and the oil slick are given in Tables VII and VIII. Despite the increase in Pd with increasing noise component for the polarimetric parameters, the Pd remains highest for the single-polarization HH and VV parameters at any given level of added noise. For a noise level increased by less than 20 dB, HV has higher Pd than all polarimetric parameters.

VI. DISCUSSION

Our analysis of L-band SAR data collected by SETHI and UAVSAR, two airborne sensors that have low instrument noise floor, allows us to formulate the following ordering

of polarization-dependent parameters for region-based slick detection, whether vegetable films or mineral oil slicks.

- 1) *Group 1*: VV, HV, the Polarization Difference (PD), and the first eigenvalue (λ_1).
- 2) *Group 2*: HH and the Hermitian Product between HH and VV (HP).
- 3) *Group 3*: The Entropy (H), the Polarization Ratio (PR), the Degree of Polarization (DoP), the co-polarized coherence (ρ_{HHVV}), the Bragg Likelihood Ratio (BLR), and the Conformity Coefficient (μ).

The parameters in the first group all provide high performance of detection based on the ROC curve results. The presence

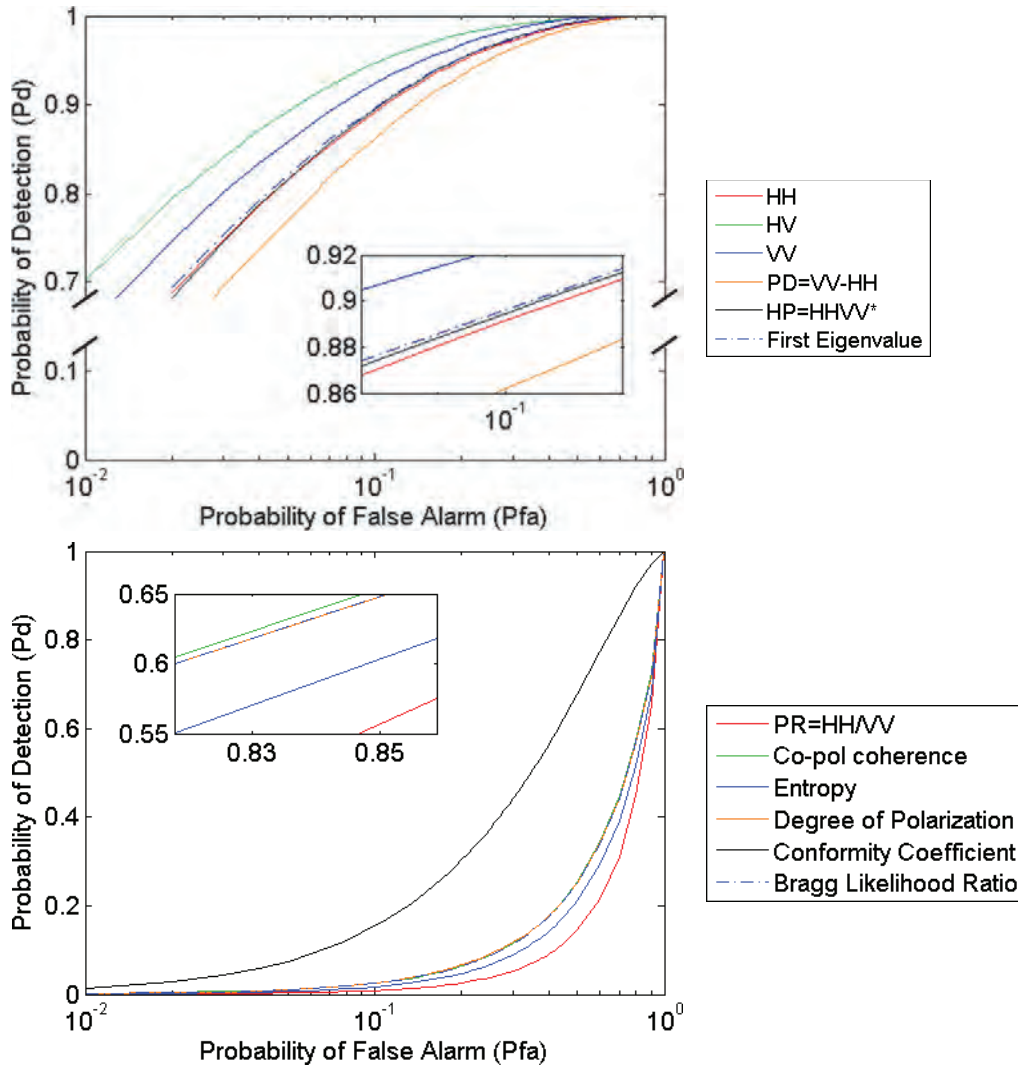


Fig. 14. SETHI, POLLUPROOF²2015 experiment, May 22, 2015, 16:07 UTC—Pd versus Pfa computed for all investigated parameters. Note the cut of the vertical axis on the top figure.

TABLE VII
SIGNAL-TO-NOISE RATIO—SETHI, NOFO²2015 EXPERIMENT, JUNE 09, 2015, 10:01 UTC

Region	Noise added	HH	HV	VV
Clean sea	Original data	26.5 dB	16.4 dB	34.1 dB
	5 dB	21.5 dB	11.4 dB	29.1 dB
	10 dB	16.5 dB	6.4dB	24.1 dB
	15 dB	11.5 dB	1.4 dB	19.1 dB
	20 dB	6.5 dB	-3.6 dB	14.1 dB
	30 dB	-3.5 dB	-13.6 dB	4.1 dB
Oil slick	Original data	21.5 dB	10.2 dB	28.0 dB
	5 dB	16.5 dB	5.2 dB	23.0 dB
	10 dB	11.5 dB	0.2 dB	18.0 dB
	15 dB	6.5 dB	-4.8 dB	13.0 dB
	20 dB	1.5 dB	-9.8 dB	8.0 dB
	30 dB	-8.5 dB	-19.8 dB	-2.0 dB

of each parameter in group 1 can be understood through the Bragg scattering model. In this framework, VV always has the highest amplitude and HH and VV have different reflectivities, ensuring that PD takes positive values. In the

tilted-Bragg-scattering model, HV can have a nonzero amplitude that is always less than both HH and VV. As a result, the first eigenvalue of the covariance matrix is dominated by VV and, to a lesser extent, HH. The control

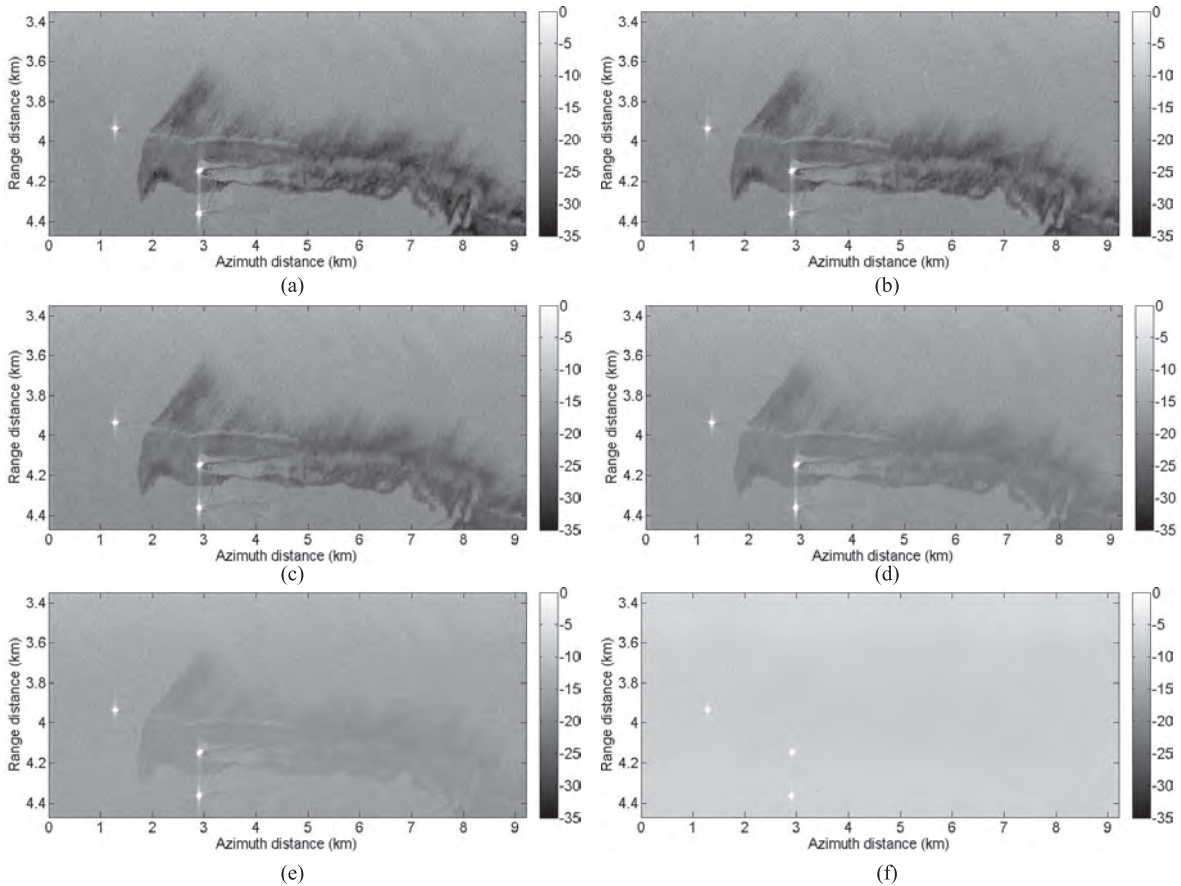


Fig. 15. Noise effect—SETHI polarization VV. (a) Original data and instrument noise increased by (b) 5 dB, (c) 10 dB, (d) 15 dB, (e) 20 dB, and (f) 30 dB—NOFO’2015 experiment, June 09, 2015, 10:01 UTC.

TABLE VIII
DoP AND ENTROPY—SETHI, NOFO’2015 EXPERIMENT,
JUNE 09, 2015, 10:01 UTC

Region	Noise added	DoP	Entropy
Clean sea	Original data	0.94	0.17
	5 dB	0.93	0.19
	10 dB	0.9	0.24
	15 dB	0.84	0.34
	20 dB	0.75	0.46
	30 dB	0.67	0.56
Oil slick	Original data	0.92	0.18
	5 dB	0.88	0.25
	10 dB	0.81	0.36
	15 dB	0.72	0.48
	20 dB	0.67	0.55
	30 dB	0.66	0.57

of VV on the value of the first eigenvalue explains why the first eigenvalue is a high-performing parameter. As previously reported in [57], HV performs well where the instrument noise floor is low because, to a good approximation in the tilted-Bragg model, the HV amplitude is proportional to PD.

The second group of parameters, composed of HH and the Hermitian Product between HH and VV channels, gives good performance of detection, although slightly lower than the performance of group 1. We show that HH channel is slightly less effective than VV for slick detection. However, we emphasize

that HH is effective for distinguishing slicks from relatively clean sea surfaces. HP suffers from the decrease in detection performance of HH compared to that of VV.

We place all remaining parameters in group 3, which has the worst capabilities of detection. The parameters in group 3 are the Polarization Ratio (PR), the co-polarized coherence (ρ_{HHVV}), the Bragg Likelihood Ratio (BLR), the Entropy (H), the Degree of Polarization (DoP) and the Conformity Coefficient (μ). For these parameters, detection performance seems to be very strongly correlated with the instrument noise and their applicability in a sea pollution detection scheme is instrument dependent. For a sufficiently high SNR, the EM wave backscattered by the slick-free sea surface remains well polarized (DoP close to 1 and Entropy close to 0). It becomes less polarized over the contaminated area (DoP decreases and Entropy increases) and the performances of detection increase. When the instrument noise becomes a significant fraction of the measured signal (low SNR), the apparent backscattered signal becomes randomly polarized for contaminated and uncontaminated sea surfaces, and no further separation between the two regions is possible. The instrument noise issue for oil spill detection using quad-polarimetric SAR data has been recently addressed in [15]. In this paper, the authors hypothesize that the often-stated claims that non-Bragg scattering occurs over slick-covered areas is due to a misinterpretation of SAR images collected with too low an SNR. Our study presented in this paper is in agreement with this hypothesis and goes even further since,

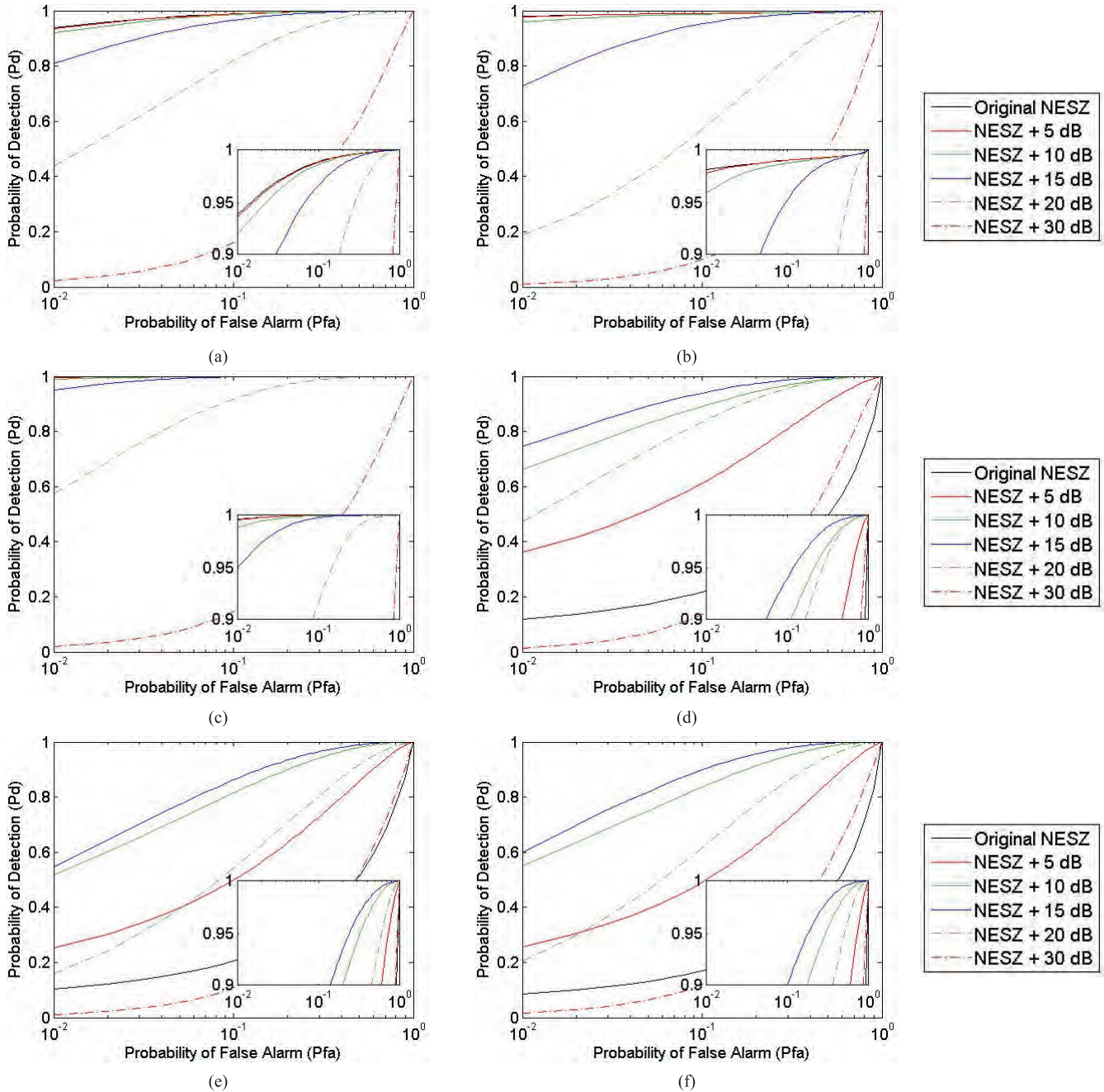


Fig. 16. Noise effect on ROC curves—SETHI (a) HH, (b) HV, (c) VV, (d) dual-pol coherence, (e) DoP, and (f) Entropy—NOFO’2015 experiment, June 09, 2015, 10:01 UTC.

for the first time, we quantify in a systematic way the effect of instrument noise on polarization-dependent SAR parameters when applied to oil spill detection. As previously reported in [15] and [41], we demonstrate that there is no deviation from Bragg scattering for radar scattering from ocean surface covered by mineral and vegetable oil.

The hierarchy that we propose here is obtained from L-band airborne SAR data collected over vegetable and mineral oil slick released during moderate wind conditions. A similar study is proposed in [56] and [57], with [57] evaluating the parameters during transport and evolution of mineral and plant slicks. The major differences between all these studies are the proposed method of measuring the capabilities of detection

of different quantities investigated and the fact that the slicks studied in [56] and [57] were thinner, formed from the release of 0.2–0.5 m³ of material rather than 45 m³ as the slick in our study. In [56], SAR data acquired by UAVSAR, TerraSAR-X, and RADARSAT-2 at nearly the same time over mineral oil spills under high-wind conditions are investigated using many of the same parameters as herein. They found likewise that VV intensity is the most efficient parameter for the detection of oil slick on sea surface. The HV channel was not investigated in [56] because of the low SNR of the satellite data. The UAVSAR image investigated in [56] is also studied in [57], combined with 17 other images covering the evolving slicks over an 8-h period. In the latter, the proposed methodology

to order the polarimetric parameters is slightly different than in [56], and the authors also found that VV intensity is very efficient for slick-sea discrimination. The HV channel was studied in [57] and, similar to our results, those authors found that the cross-polarized channel is attractive for slick detection over ocean surface when employed SAR data are acquired with a very low instrument noise floor. Comparing [56], [57], and the results that we report here, there is a clear consensus on the use of VV or HV channels for slick detection at sea. The main difference between results obtained in this paper and those reported in [56] and [57] concerns the performances of detection given by the Polarization Difference. Indeed, we found here, and as already reported in [17], [33], [43], and [54], that the Polarization Difference is one of the most efficient parameters for slick-sea discrimination. This difference could be due to different wind conditions, sea state, or slick thicknesses, and highlights the complexity of slick detection across a range of variables under which they can occur.

VII. CONCLUSION

To guide the selection of the most appropriate SAR imaging mode for marine pollution detection, a methodology based on the analysis of ROC curves has been reported in this paper. The ROC analysis accounts for the non-Gaussian tails of the probability distribution of parameter values, which are particularly important for the slick-covered areas. We compare the probabilities of detecting a slick with the probabilities of a false alarm for a range of detection thresholds to rank various polarization-dependent parameters in the order of slick-detection performance, from best to worst. A key aspect of the results reported in this paper lies in the analysis of the instrument noise effect on the performance of detection offered by the studied parameters. This is done by progressively adding Gaussian white noise directly to the raw SAR data and then processing the noisier data using the standard processing software. The other important aspects of this paper derive from three factors: the quantitative evaluation of a dozen common parameters used for detecting marine slicks; the uniqueness of the studied data set collected by two airborne sensors operating at L-band, both of which are characterized by an instrument noise floor that is much lower than the one that is currently available from spaceborne SARs; and the evaluation of detectability of both vegetable and mineral oil slicks with the same low-noise instrument. Low noise makes the parameters more sensitive to the surface properties and less influenced by the sensor.

We find that HV amplitude can outperform all other investigated amplitudes and polarimetric settings whenever the instrument noise is sufficiently low (at least 5 dB in this paper). However, as instrument noise increases, HV amplitude and all polarimetric parameters that rely on HV become corrupted by the noise and their slick-detection performance diminishes. HV is closely followed by the investigated co-polarized settings (ordered as follows: VV, the Polarization Difference, HH, and the Hermitian Product between HH and VV), while being more robust to a lower SNR than the cross-polarized channel.

We note that this relative ordering is determined from a single combined set of sea state, meteorological conditions, and slick properties, and further work is needed to expand to other conditions, in particular lower wind speeds and different slick thicknesses.

For detecting slicks on the sea surface, we propose that VV parameter offers the best tradeoff between the benefit of detection performance and the instrument and data requirements.

We find that the co-pol amplitudes (HH and VV) and two polarimetric parameters, the Polarization Difference and the first eigenvalue of the quad-pol covariance matrix, are more robust in the presence of instrument noise than the cross-pol (HV) amplitude and quad-polarimetric parameters. This disparity in robustness is due to higher co-pol amplitudes relative to the cross-pol amplitude and the strong impact of instrument noise on POLSAR parameters. This implies that polarimetric quantities which combine the four polarimetric channels have performances of detection mainly driven by the instrument noise level (NESZ).

ACKNOWLEDGMENT

The authors would like to thank the Norwegian Clean Seas Association for Operating Companies (NOFO), Norway, for allowing them to participate in the oil-on-water exercise, which was carried out during June 8, 2015–June 14, 2015. They would like to thank everyone involved in the experiment at sea and those who participated in SAR data processing. They would also like to thank H. Oriot from ONERA, Palaiseau, France, for his thoughtful discussions about receiver operating characteristic curve computation. This research was carried out in part at the Jet Propulsion Laboratory, California Institute of Technology, Pasadena, CA, USA, under contract with the U.S. National Aeronautics and Space Administration (NASA). The UAVSAR data are courtesy of the NASA/Jet Propulsion Laboratory and are openly available through the Alaska Satellite Facility (<http://asf.alaska.edu>).

REFERENCES

- [1] M. Fingas and C. Brown, "Review of oil spill remote sensing," *Marine Pollution Bull.*, vol. 83, no. 1, pp. 9–23, 2014.
- [2] C. Brekke and A. H. S. Solberg, "Oil spill detection by satellite remote sensing," *Remote Sens. Environ.*, vol. 95, no. 1, pp. 1–13, 2005.
- [3] O. Garcia-Pineda *et al.*, "Detection of floating oil anomalies from the Deepwater Horizon oil spill with synthetic aperture radar," *Oceanography*, vol. 26, no. 2, pp. 124–137, 2013.
- [4] H. A. Espedal, "Satellite SAR oil spill detection using wind history information," *Int. J. Remote Sens.*, vol. 20, no. 1, pp. 49–65, Jan. 1999.
- [5] H. A. Espedal, O. M. Johannessen, J. A. Johannessen, E. Dano, D. R. Lyzenga, and J. C. Knulst, "COASTWATCH'95: ERS 1/2 SAR detection of natural film on the ocean surface," *J. Geophys. Res.*, vol. 103, no. C11, pp. 24969–24982, 1998.
- [6] M. Gade and W. Alpers, "Using ERS-2 SAR images for routine observation of marine pollution in European coastal waters," *Sci. Total Environ.*, vols. 237–238, pp. 441–448, Sep. 1999.
- [7] O. Garcia-Pineda, B. Zimmer, M. Howard, W. Pichel, X. Li, and I. R. MacDonald, "Using SAR images to delineate ocean oil slicks with a texture-classifying neural network algorithm (TCNNA)," *Can. J. Remote Sens.*, vol. 35, no. 5, pp. 411–421, Oct. 2009.
- [8] F. Girard-Ardhuin, G. Mercier, F. Collard, and R. Garello, "Operational oil-slick characterization by SAR imagery and synergistic data," *IEEE J. Ocean. Eng.*, vol. 30, no. 3, pp. 487–495, Jul. 2005.

- [9] A. D. Jenkins and K. B. Dysthe, "The effective film viscosity coefficients of a thin floating fluid layer," *J. Fluid Mech.*, vol. 344, pp. 335–337, Aug. 1997.
- [10] A. D. Jenkins and A. S. Jacobs, "Wave damping by a thin layer of viscous fluid," *Phys. Fluids*, vol. 9, no. 5, pp. 1256–1264, 1997.
- [11] K. P. Singh, A. L. Gray, R. K. Hawkins, and R. A. O'Neil, "The influence of surface oil on c-and ku-band ocean backscatter," *IEEE Trans. Geosci. Remote Sens.*, vol. GE-24, no. 5, pp. 738–744, Sep. 1986.
- [12] G. R. Valenzuela, "Theories for the interaction of electromagnetic and oceanic waves—A review," *Boundary-Layer Meteorol.*, vol. 13, nos. 1–4, pp. 61–85, Jan. 1978.
- [13] M. Migliaccio, F. Nunziata, and A. Buono, "SAR polarimetry for sea oil slick observation," *Int. J. Remote Sens.*, vol. 36, no. 12, pp. 3243–3273, 2015.
- [14] A. H. S. Solberg, "Remote sensing of ocean oil-spill pollution," *Proc. IEEE*, vol. 100, no. 10, pp. 2931–2945, Oct. 2012.
- [15] W. Alpers, B. Holt, and K. Zeng, "Oil spill detection by imaging radars: Challenges and pitfalls," *Remote Sens. Environ.*, vol. 201, pp. 133–147, Nov. 2017.
- [16] M. Migliaccio, F. Nunziata, and A. Gambardella, "On the co-polarized phase difference for oil spill observation," *Int. J. Remote Sens.*, vol. 30, no. 6, pp. 1587–1602, 2009.
- [17] M. W. Hansen, V. Kudryavtsev, B. Chapron, C. Brekke, and J. A. Johannessen, "Wave breaking in slicks: Impacts on C-band quad-polarized SAR measurements," *IEEE J. Sel. Topics Appl. Earth Observ. Remote Sens.*, vol. 9, no. 11, pp. 4929–4940, Nov. 2016.
- [18] M. Gade, W. Alpers, H. Hühnerfuss, H. Masuko, and T. Kobayashi, "Imaging of biogenic and anthropogenic ocean surface films by the multifrequency/multipolarization SIR-C/X-SAR," *J. Geophys. Res.*, vol. 103, no. C9, pp. 18851–18866, 1998.
- [19] R. Touzi, F. J. Charbonneau, R. K. Hawkins, and P. W. Vachon, "Ship detection and characterization using polarimetric SAR," *Can. J. Remote Sens.*, vol. 30, no. 3, pp. 552–559, 2004.
- [20] F. Nunziata, A. Gambardella, and M. Migliaccio, "On the Mueller scattering matrix for SAR sea oil slick observation," *IEEE Geosci. Remote Sens. Lett.*, vol. 5, no. 4, pp. 691–695, Oct. 2008.
- [21] M. Migliaccio, A. Gambardella, F. Nunziata, M. Shimada, and O. Isoguchi, "The PALSAR polarimetric mode for sea oil slick observation," *IEEE Trans. Geosci. Remote Sens.*, vol. 47, no. 12, pp. 4032–4041, Dec. 2009.
- [22] D. Velotto, M. Migliaccio, F. Nunziata, and S. Lehner, "Dual-polarized TerraSAR-X data for oil-spill observation," *IEEE Trans. Geosci. Remote Sens.*, vol. 49, no. 12, pp. 4751–4762, Dec. 2011.
- [23] R. Shirvany, M. Chabert, and J. Y. Tourneret, "Ship and oil-spill detection using the degree of polarization in linear and hybrid/compact dual-pol SAR," *IEEE J. Sel. Topics Appl. Earth Observ. Remote Sens.*, vol. 5, no. 3, pp. 885–892, Jun. 2012.
- [24] F. Nunziata, A. Gambardella, and M. Migliaccio, "On the degree of polarization for SAR sea oil slick observation," *ISPRS J. Photogramm. Remote Sens.*, vol. 78, pp. 41–49, Apr. 2013.
- [25] S. Skrunes, C. Brekke, and T. Eltoft, "Characterization of marine surface slicks by radarsat-2 multipolarization features," *IEEE Trans. Geosci. Remote Sens.*, vol. 52, no. 9, pp. 5302–5319, Sep. 2014.
- [26] A.-B. Salberg, O. Rudjord, and A. H. S. Solberg, "Oil spill detection in hybrid-polarimetric SAR images," *IEEE Trans. Geosci. Remote Sens.*, vol. 52, no. 10, pp. 6521–6533, Oct. 2014.
- [27] S. Angelliaume, X. Ceamanos, F. Viallefont-Robinet, R. Baqué, P. Déliot, and V. Miegbielle, "Hyperspectral and radar airborne imagery over controlled release of oil at sea," *Sensors*, vol. 17, no. 8, p. 1772, 2017.
- [28] S. Hensley *et al.*, "The UAVSAR instrument: Description and first results," in *Proc. IEEE Radar Conf.*, Rome, Italy, May 2008, pp. 1–6.
- [29] K. D. Ward, R. J. A. Tough, and S. Watts, *Sea Clutter: Scattering, the K Distribution and Radar Performance*, 2nd ed. Herts, U.K.: IET, 2013.
- [30] F. T. Ulaby, R. K. Moore, and A. K. Fung, *Microwave Remote Sensing: Active and Passive: Radar Remote Sensing and Surface Scattering and Emission Theory*, vol. 2. Dedham, MA, USA: Artech House, 1986.
- [31] Y. Quilfen, B. Chapron, A. Bentamy, J. Gourrion, T. El Fouhailly, and D. Vandemark, "Global ERS 1 and 2 and NSCAT observations: Upwind/crosswind and upwind/downwind measurements," *J. Geophys. Res. Oceans*, vol. 104, no. C5, pp. 11459–11469, May 1999.
- [32] J. Horstmann, W. Koch, S. Lehner, and R. Tonboe, "Wind retrieval over the ocean using synthetic aperture radar with C-band HH polarization," *IEEE Trans. Geosci. Remote Sens.*, vol. 38, no. 5, pp. 2122–2131, Sep. 2000.
- [33] V. N. Kudryavtsev, B. Chapron, A. G. Myasoedov, F. Collard, and J. A. Johannessen, "On dual co-polarized SAR measurements of the ocean surface," *IEEE Geosci. Remote Sens. Lett.*, vol. 10, no. 4, pp. 761–765, Jul. 2013.
- [34] V. Kudryavtsev, D. Hauser, G. Caudal, and B. Chapron, "A semiempirical model of the normalized radar cross section of the sea surface, 2. Radar modulation transfer function," *J. Geophys. Res.*, vol. 108, no. C3, pp. 2156–2202, 2003.
- [35] B. Holt, "SAR imaging of the ocean surface," in *Synthetic Aperture Radar (SAR) Marine User's Manual*, C. R. Jackson and J. R. Apel, Eds. Silver Spring, MD, USA: NOAA, 2004, pp. 263–275.
- [36] K. Hasselmann *et al.*, "Theory of synthetic aperture radar ocean imaging: A MARSEN view," *J. Geophys. Res.*, vol. 90, no. C3, pp. 4659–4686, 1985.
- [37] G. R. Valenzuela, "Scattering of electromagnetic waves from a tilted slightly rough surface," *Radio Sci.*, vol. 3, no. 11, pp. 1057–1066, Nov. 1968.
- [38] T. Meissner and F. J. Wentz, "The complex dielectric constant of pure and sea water from microwave satellite observations," *IEEE Trans. Geosci. Remote Sens.*, vol. 42, no. 9, pp. 1836–1849, Sep. 2004.
- [39] K. Folgerø, "Bilinear calibration of coaxial transmission/reflection cells for permittivity measurement of low-loss liquids," *Meas. Sci. Technol.*, vol. 7, no. 9, pp. 1260–1269, 1996.
- [40] T. Friisø, Y. Schildberg, O. Rambeau, T. Tjomsland, H. J. Førdedal, and J. Sjøblom, "Complex permittivity of crude oils and solutions of heavy crude oil fractions," *J. Dispersion Sci. Technol.*, vol. 19, no. 1, pp. 93–126, 1998.
- [41] B. Minchew, C. E. Jones, and B. Holt, "Polarimetric analysis of backscatter from the Deepwater Horizon oil spill using L-band synthetic aperture radar," *IEEE Trans. Geosci. Remote Sens.*, vol. 50, no. 10, pp. 3812–3830, Oct. 2012.
- [42] B. Minchew, "Determining the mixing of oil and sea water using polarimetric synthetic aperture radar," *Geophys. Res. Lett.*, vol. 39, no. 16, p. L16607, 2012.
- [43] S. Angelliaume, B. Minchew, S. Chataing, P. Martineau, and V. Miegbielle, "Multifrequency radar imagery and characterization of hazardous and noxious substances at sea," *IEEE Trans. Geosci. Remote Sens.*, vol. 55, no. 5, pp. 3051–3066, May 2017.
- [44] *Bonn Agreement Aerial Surveillance Handbook*, Bonn Agreement, London, U.K., 2004, p. 96.
- [45] *Bonn Agreement Aerial Surveillance Handbook*, Bonn Agreement, London, U.K., 2009, p. 106.
- [46] I. Leifer *et al.*, "State of the art satellite and airborne marine oil spill remote sensing: Application to the BP Deepwater Horizon oil spill," *Remote Sens. Environ.*, vol. 124, pp. 185–209, Sep. 2012.
- [47] M. Fingas and B. Fieldhouse, "Studies on water-in-oil products from crude oils and petroleum products," *Marine Pollution Bull.*, vol. 64, no. 2, pp. 272–283, 2012.
- [48] Z. H. Shah and Q. A. Tahir, "Dielectric properties of vegetable oils," *J. Sci. Res.*, vol. 3, no. 3, pp. 481–492, Aug. 2011.
- [49] U. Erle, M. Regier, C. Persch, and H. Schubert, "Dielectric properties of emulsions and suspensions: Mixture equations and measurement comparisons," *J. Microw. Power Electromagn. Energy*, vol. 35, no. 3, pp. 185–190, 2000.
- [50] W. Alpers and H. A. Espedal, "Oils and surfactants," in *Synthetic Aperture Radar Marine User's Manual*, C. R. Jackson and J. R. Apel, Eds. Washington, DC, USA: U.S. Department of Commerce, National Oceanic and Atmospheric Administration, 2004, ch. 11, pp. 263–275.
- [51] V. Wismann, M. Gade, W. Alpers, and H. Hühnerfuss, "Radar signatures of marine mineral oil spills measured by an airborne multifrequency radar," *Int. J. Remote Sens.*, vol. 19, no. 18, pp. 3607–3623, 1998.
- [52] M. Gade, W. Alpers, H. Hühnerfuss, V. Wismann, and P. Lange, "On the reduction of the radar backscatter by oceanic surface films: Scatterometer measurements and their theoretical interpretation," *Remote Sens. Environ.*, vol. 66, no. 1, pp. 52–70, Oct. 1998.
- [53] D. Latini, F. Del Frate, and C. E. Jones, "Multi-frequency and polarimetric quantitative analysis of the Gulf of Mexico oil spill event comparing different SAR systems," *Remote Sens. Environ.*, vol. 183, pp. 26–42, Sep. 2016.
- [54] D. V. Ivonin, S. Skrunes, C. Brekke, and A. Y. Ivanov, "Interpreting sea surface slicks on the basis of the normalized radar cross-section model using RADARSAT-2 copolarization dual-channel SAR images," *Geophys. Res. Lett.*, vol. 43, no. 6, pp. 2748–2757, 2016.

- [55] S. Skrunes, C. Brekke, T. Eltoft, and V. Kudryavtsev, "Comparing near-coincident C- and X-band SAR acquisitions of marine oil spills," *IEEE Trans. Geosci. Remote Sens.*, vol. 53, no. 4, pp. 1958–1975, Apr. 2015.
- [56] S. Skrunes, C. Brekke, C. E. Jones, and B. Holt, "A multisensor comparison of experimental oil spills in polarimetric SAR for high wind conditions," *IEEE J. Sel. Topics Appl. Earth Observ. Remote Sens.*, vol. 9, no. 11, pp. 4948–4961, Nov. 2016.
- [57] M. M. Espeseth, S. Skrunes, C. E. Jones, C. Brekke, B. Holt, and A. P. Doulgeris, "Analysis of evolving oil spills in full-polarimetric and hybrid-polarity SAR," *IEEE Trans. Geosci. Remote Sens.*, vol. 59, no. 7, pp. 4190–4210, Jul. 2017.
- [58] M. Gade, W. Alpers, H. Hühnerfuss, and P. A. Lange, "Wind wave tank measurements of wave damping and radar cross sections in the presence of monomolecular surface films," *J. Geophys. Res.*, vol. 103, no. C2, pp. 3167–3178, 1998.
- [59] C.-A. Guérin, G. Soriano, and B. Chapron, "The weighted curvature approximation in scattering from sea surfaces," *Waves Random Complex Media*, vol. 20, no. 3, pp. 364–384, 2010.
- [60] H. A. Zebker, J. J. van Zyl, and D. N. Held, "Imaging radar polarimetry from wave synthesis," *J. Geophys. Res.*, vol. 92, no. B1, pp. 683–701, Jan. 1987.
- [61] W. J. Plant, E. A. Terray, R. A. Petitt, Jr., and W. C. Keller, "The dependence of microwave backscatter from the sea on illuminated area: Correlation times and lengths," *J. Geophys. Res.*, vol. 99, no. C5, pp. 9705–9723, May 1994.
- [62] A. S. Milman, A. O. Scheffler, and J. R. Bennett, "A theory of the synthetic aperture radar images of time-dependent scenes," *J. Geophys. Res.*, vol. 98, no. C1, pp. 911–925, Jan. 1993.
- [63] W. Born and E. Wolf, *Principles of Optics*. New York, NY, USA: Pergamon, 1959.
- [64] W.-M. Boerner *et al.*, "Polarimetric in radar remote sensing: Basic and applied concepts," in *Principles and Applications of IMAGING RADAR*, vol. 2. Hoboken, NJ, USA: Wiley, 1998.
- [65] R. Touzi, W.-M. Boerner, J.-S. Lee, and E. Lueneburg, "A review of polarimetry in the context of synthetic aperture radar: Concepts and information extraction," *Can. J. Remote Sens.*, vol. 30, no. 3, pp. 380–407, 2004.
- [66] B. Zhang, W. Perrie, X. Li, and W. B. Pichel, "Mapping sea surface oil slicks using RADARSAT-2 quad-polarization SAR image," *Geophys. Res. Lett.*, vol. 38, no. 10, p. L10602, 2011.
- [67] M.-L. Truong-Loi, P. Dubois-Fernandez, A. Freeman, and E. Pottier, "The conformity coefficient or how to explore the scattering behaviour from compact polarimetry mode," in *Proc. IEEE Radar Conf.*, Pasadena, CA, USA, May 2009, pp. 1–6.
- [68] S. R. Cloude and E. Pottier, "A review of target decomposition theorems in radar polarimetry," *IEEE Trans. Geosci. Remote Sens.*, vol. 34, no. 2, pp. 498–518, Mar. 1996.
- [69] S. R. Cloude and E. Pottier, "An entropy based classification scheme for land applications of polarimetric SAR," *IEEE Trans. Geosci. Remote Sens.*, vol. 35, no. 1, pp. 68–78, Jan. 1997.
- [70] C. E. Jones *et al.*, "Measurement and modeling of oil slick transport," *J. Geophys. Res. Oceans*, vol. 121, no. 10, pp. 7759–7775, 2016.
- [71] I. Hajnsek, E. Pottier, and S. R. Cloude, "Inversion of surface parameters from polarimetric SAR," *IEEE Trans. Geosci. Remote Sens.*, vol. 41, no. 4, pp. 727–744, Apr. 2003.
- [72] J. P. Egan, *Signal Detection Theory and ROC Analysis* (Cognition and Perception). New York, NY, USA: Academic, 1975.
- [73] *MOS Sweeper—Egersund Group*. Accessed: Jan. 23, 2018. [Online]. Available: <http://www.egersundgroup.no/oilspill/mos-sweeper>



Sébastien Angelliaume received the Engineering degree from the Ecole Nationale Supérieure d'Ingénieur de Constructions Aéronautiques, Toulouse, France, and the M.S. degree from the Ecole Nationale Supérieure d'Electrotechnique, d'Electronique, d'Informatique, d'Hydraulique et des Télécommunications, Toulouse, both in 2003.

Since 2006, he has been with the Electromagnetism and Radar Department, Office National d'Etudes et de Recherches Aérospatiales (ONERA—the French Aerospace Lab), Salon de

Provence, France, where he has been involved in the ONERA synthetic aperture radar airborne platforms RAMSES and SETHI, developing science applications. Since 2010, his research at ONERA has focused mainly on remote sensing over the ocean surface.



Pascale C. Dubois-Fernandez (A'04–M'04–SM'04) received the Diplôme d'Ingenieur degree from the Ecole Nationale Supérieure d'Ingénieur de Constructions Aéronautiques, Toulouse, France, in 1983, and the M.S. and Eng. degrees from the California Institute of Technology, Pasadena, CA, USA, in 1984 and 1986, respectively.

She was with the Radar Science and Technology Group, Jet Propulsion Laboratory, Pasadena, CA, USA, where she stayed for ten years, participating in numerous programs such as Magellan, AIRSAR, and SIR-C. She then moved back to France, where she focused on cartographic applications of satellite data. In 2000, she joined the Electromagnetism and Radar Department, Office National d'Etudes et de Recherches Aérospatiales (ONERA—the French Aerospace Lab), Salon de Provence, France, where she has been involved in the ONERA synthetic aperture radar (SAR) airborne platform, RAMSES, developing science applications as the SAR civilian remote sensing expert.



Cathleen E. Jones received the B.S. degree in physics from Texas A&M University, College Station, TX, USA, and the Ph.D. degree in physics from the California Institute of Technology, Pasadena, CA, USA.

She is currently a Radar Scientist with NASA's Jet Propulsion Laboratory, California Institute of Technology, Pasadena, CA, USA, where her main research is focused on using radar remote sensing for studying natural disasters and monitoring critical infrastructure, primarily using high-resolution L-band PolSAR and InSAR based on UAVSAR data. Her research interests include development of methods for determining oil slick characteristics and identifying levee deformation, seepage, and general subsidence rates using synthetic aperture radar (SAR), and detection of sinkhole precursors in InSAR-challenged areas.



Benjamin Holt received the B.S. degree from Stanford University, Stanford, CA, USA, in 1972, and the M.S. degree in physical oceanography from the University of Southern California, Los Angeles, CA, USA, in 1988.

In 1978, he joined the Ocean Circulation Group, Earth Science Section, Jet Propulsion Laboratory, California Institute of Technology, Pasadena, CA, USA, where he is currently a Research Scientist. His research interests include using multisensor remote sensing data to examine the geophysical state of polar sea ice and snow, coastal oceanography and circulation, the detection of marine pollutants, new instrument development, and techniques for microwave measurement of sea ice thickness.



Brent Minchew received the B.Sc. and M.Sc. degrees in aerospace engineering from the University of Texas at Austin, Austin, TX, USA, in 2008 and 2010, respectively, and the Ph.D. degree in geophysics from the California Institute of Technology, Pasadena, CA, USA.

From 2016 to 2018, he was an NSF Postdoctoral Fellow at the British Antarctic Survey, Cambridge, U.K. He is currently an Assistant Professor with the Department of Earth, Atmospheric and Planetary Sciences, Massachusetts Institute of Technology, Cambridge, MA, USA. His research interests include remote sensing applications and environmental fluid dynamics, with an emphasis on glacier mechanics.



Emna Amri was born in Tunis, Tunisia, in 1990. She received the Engineering degree in computer science and the master's degree in intelligent systems in imaging and artificial vision from the University of Tunis El Manar, Tunis, in 2015 and 2017, respectively.

Her research interests include computer vision, machine learning, and remote sensing.



Véronique Miegbielle received the Geology Doctorate degree with a specialization in remote sensing from Pau and Pays de l'Adour University, Pau, France, in 1993.

She spent the first 15 years of her career, dealing with geology and environmental subjects. In 2009, she moved on to take care of Remote Sensing Service at Total, Pau. Since 2011, she has been in charge of remote sensing offshore research project.